

# **Strategies to Mitigate the Challenges of Corrosive Electrolytes in Rechargeable Aluminum Batteries**

Zur Erlangung des akademischen Grades einer  
DOKTORIN DER NATURWISSENSCHAFTEN

(Dr. rer. nat.)

von der KIT-Fakultät für Chemie und Biowissenschaften  
des Karlsruher Instituts für Technologie (KIT)

genehmigte

DISSERTATION

von

M.Sc. Mahla Talari

1. Referent: Prof. Dr. rer. nat Helmut Ehrenberg

2. Referentin: Prof. Dr. Sonia Dsoke

Tag der mündlichen Prüfung: 24.10.2024



## **Selbständigkeitserklärung**

Hiermit versichere ich, dass ich die vorliegende Arbeit selbstständig verfasst habe, dass ich keine anderen als die angegebenen Quellen und Hilfsmittel benutzt habe, dass ich die wörtlich oder inhaltlich übernommenen Stellen als solche gekennzeichnet habe und, dass ich die Satzung des KIT zur Sicherung guter wissenschaftlicher Praxis in der jeweils gültigen Fassung beachtet habe.

Karlsruhe, den .....

Mahla Talari



## Acknowledgment

Thank you all for your contributions and support which helped me throughout my PhD journey.

First and foremost, I am indebted to my Professor, *Prof. Helmut Ehrenberg*, for providing me with this invaluable opportunity to pursue my PhD at the IAM-ESS. His support has been instrumental in my academic growth.

I would also like to sincerely thank my supervisor, *prof. Sonia Dsoke*, whose unwavering encouragement, patience, and expertise have been invaluable in shaping this research. Her mentorship and guidance have been pivotal in my success.

I am also grateful to *Dr. Fabian Jeschull*, whose insights and organizational skills have been essential in facilitating the progress of our research group.

I would like to acknowledge the invaluable support of *Prof. Julia Maibach*, who provided me with the opportunity to conduct research with her team at Chalmers University. Her expertise in XPS analysis and her willingness to patiently answer my questions, both simple and complex, have been invaluable. Special thanks go to the specific faculty and staff members, particularly *Vanessa Trouillet*, for their assistance and advice.

Thank you, my colleagues. Our companionship, discussions, and moral support have created a positive and supportive working environment. The coffee breaks have not only boosted my motivation but have also fostered a collaborative and enriching research atmosphere. “I choose not to name you all, but t you are always in my thoughts.”

*Elian Feuntez Mendoza* and *Noha Sabi*, I want you to know my gratitude. You became more than colleagues to me. Your support extended beyond professional boundaries. Your friendship and encouragement added a touch of sparkle, making the serious PhD journey more enjoyable and enriching.

Lastly, but most importantly, I would like to express my deepest gratitude to *Siavosh Mozafari Nezhad*, my husband. Your unfaltering love and encouragement have been my constant source of strength and motivation during the most challenging times during these years. When disappointments and failures arose, and the sun had already set, taking my motivation with it, you stood by me. You gave me the courage to step forward, to explore new paths. you took my fears and filled the voids with visions of success with your creative ideas. During the hardest nights of my PhD, which were also the loneliest times of my immigration journey, you cared for me as the best friend and family I could ever ask for. Your presence was my anchor, your love my guiding light, and for that, I am eternally grateful.

به لطف آنکه نگهدار من است، دل خوش دار

که در کنار تو هرگز دلش به هیچ آزرده مباد

سعدی

## Table of Content

Abbreviations.....	X
Symbol and constant.....	XIII
Figures .....	XIV
Tables .....	XVIII
Zusammenfassung .....	XIX
Abstract .....	XXII
1 Introduction and Motivation.....	1
2 Theoretical background .....	3
2.1 Key parameters of battery electrochemistry .....	3
2.2 Understanding of rechargeable aluminum batteries (RABs).....	5
2.2.1 Key points when discussing RABs.....	7
2.3 Electrolyte evolution in RABs: A journey from molten salts to chloride-free organics.....	9
2.3.1 High-temperature molten salts electrolytes.....	9
2.3.2 Room-temperature chloroaluminate ionic liquid electrolyte .....	10
2.3.3 Non-ionic liquid electrolytes with $\text{AlCl}_3$ .....	12
2.3.4 Al halides-based electrolytes.....	13
2.3.5 Chloride-free electrolytes .....	14
2.4 Mitigating corrosion using inhibitors.....	18
3 Experimental .....	20
3.1 Chemicals and Metal foils .....	20
3.2 Electrolytes preparation .....	21
3.2.1 Non-corrosive electrolyte based on $\text{Al}(\text{OTf})_3$ .....	21
3.2.2 Chloroaluminate ionic liquid electrolytes .....	21
3.3 Electrochemical analysis.....	22
3.3.1 Cells preparation .....	22

3.3.2	Electrochemical characterization .....	24
3.3.2.1	Cyclic voltammetry measurements (CV) .....	25
3.3.2.2	Chronoamperometry measurements (CA) .....	25
3.3.2.3	Potentiodynamic polarization measurements .....	26
3.4	Materials characterization techniques .....	27
3.4.1	Scanning electron microscopy and energy-dispersive X-ray spectroscopy (SEM/EDX) .....	28
3.4.2	Optical microscopy .....	28
3.4.3	X-ray photoelectron spectroscopy (XPS) .....	28
3.5	Analytical techniques .....	29
3.5.1	Electrochemical quartz crystal microbalance (EQCM) .....	30
3.5.2	Gas chromatography (GC) .....	31
3.5.3	Karl Fisher (KF) Titration .....	31
4	Assessing the feasibility of Al plating/stripping from a non-corrosive Al(OTf) <sub>3</sub> -based electrolyte .....	32
4.1	Investigation on Al plating/stripping from ANU-20000 Electrolyte .....	32
4.2	The Impact of urea on electrochemical reactions .....	39
4.3	Impact of water content on the electrochemical reactions .....	42
4.4	Key finding of this chapter .....	45
5	Mitigating corrosivity of AlCl <sub>3</sub> :EMImCl electrolyte using inhibitors .....	46
5.1	Impact of inhibitors on corrosion behavior of AISI 316L .....	48
5.1.1	Evaluation of corrosion current density <i>via</i> electrochemical assessments .....	48
5.1.2	Surface characterization of AISI 316L using XPS .....	52
5.1.2.1	XPS studies of immersed AISI 316L in the electrolyte containing inhibitors 53	
5.1.2.2	XPS results of polarized AISI 316 in the electrolyte-containing inhibitors 58	
5.2	Impact of inhibitors on Al negative electrode .....	65



5.2.1	Evaluation of inhibitors impact on Al plating and stripping <i>via</i> electrochemical analysis	65
5.2.2	Surface Characterization of Al Negative Electrode	67
5.2.2.1	Al foil immersed in the electrolytes-containing inhibitors: XPS study	68
5.2.2.2	Al foil cycled in the electrolytes-containing inhibitors: XPS study	72
	Key finding of this chapter	78
6	Technical challenges in evaluating RABs	80
6.1	Reference electrode challenges in RABs evaluation	80
6.2	Detrimental effects of water in RABs	81
6.3	Challenges of in-situ characterization in RABs research	83
7	Conclusion	84
8	Outlook	87
	A pinch of amusement	89
9	References	91
10	Contributions of Authorship	103
11	Scientific contributions	104
11.1	Publication	104
11.2	Conference contributions	104

## Abbreviations

A15E1	AlCl <sub>3</sub> :EMImCl (molar ratio 1.5:1)
A15E1BF <sub>4</sub>	A15E1+ 2 wt% EMImBF <sub>4</sub>
A15E1OTf <sub>2</sub>	A15E1+ 2 wt% EMImOTf
A15E1Py <sub>2</sub>	A15E1+ 2 wt% Py <sub>1.4</sub> Cl
ACN	Acetonitrile
Al	Aluminum
AlBr <sub>3</sub>	Aluminum tribromide
AlF <sub>3</sub>	Aluminum Fluoride
Al <sub>2</sub> O <sub>3</sub>	Aluminum Oxide
Al(OTf) <sub>3</sub>	Aluminum trifluoromethanesulfonate
Al(TFSI) <sub>3</sub>	Aluminum tris(trifluoromethanesulfonyl)imide
BMIM	1-butyl-3-methylimidazolium
BMImBF <sub>4</sub>	1-butyl-3-methylimidazolium tetrafluoroborate
Ca	Calcium
CaCl <sub>2</sub>	Calcium chloride
CE	Counter Electrode
Co	Cobalt
CV	Cyclic voltammetry
CuSO <sub>4</sub>	Copper (II) sulfate
DFT	Density functional theory
DMSO	Dimethyl sulfoxide
E <sub>corr</sub>	Corrosion potentials
EDX	Energy-dispersive X-ray spectroscopy
EQCM	Electrochemical Quartz Crystal Microbalance
Et <sub>2</sub> O	Diethyl ether
EMIM	1-ethyl-3-methylimidazolium
EMIM BF <sub>4</sub>	1-ethyl-3-methylimidazolium tetrafluoroborate

EMIM OTf	1-ethyl-3-methylimidazolium trifluoromethanesulfonate
EMIM TFSI	1-ethyl-3-methylimidazolium bis(trifluoromethylsulfonyl)amide
FeO	Iron(II) oxide
Fe <sub>2</sub> O <sub>3</sub>	Iron(III) oxide
FTIR	Fourier-transform infrared spectroscopy
GC	Glassy carbon
GC	Gas Chromatography
GBL	Gamma-butyrolactone
HER	Hydrogen evolution reaction
[HMIM][BF <sub>4</sub> ]	1-hexyl-3-methylimidazolium tetrafluoroborate
[HMIM][OTf]	1-hexyl-3-methylimidazolium trifluoromethanesulfonate
I <sub>corr</sub>	Corrosion current densities
IE%	Inhibition efficiencies
K	Potassium
KBr	Potassium bromide
KF	Karl Fischer titration
Li	Lithium
LiAlH <sub>4</sub>	Lithium Aluminum hydride
LiH	Lithium hydride
LIBs	Lithium-ion batteries
Mg	Magnesium
MeOH	Methanol
Na	Sodium
Ni	Nickel
NMA	<i>N</i> -methyl acetamide
OCV	Open circuit voltage
PC	Propylene carbonate
P <sub>4</sub> O <sub>10</sub>	Phosphorus pentoxide

RABs	Rechargeable aluminum batteries
RTILs	Room temperature ionic liquids
SEM	Scanning electron microscopy
SHE	Standard hydrogen electrode
TCD	Thermal conductivity detector
THF	Tetrahydrofuran
weight%	Weight percentage of an element
WE	Working electrode
XAS	X-ray absorption spectroscopy
XRD	X-ray diffraction
XPS	X-ray photoelectron spectroscopy
Zn	Zinc

## Symbol and constant

$C_f$	Sensitivity factor
$E$	Electromotive force / V
$E^\circ$	Standard electrode potential / V
$\varepsilon$	Specific energy / Wh kg <sup>-1</sup>
$F$	Faraday constant (96485 C mol <sup>-1</sup> )
$I$	Current / A
$m$	Mass / g
$M$	Molecular mass / g mol <sup>-1</sup>
$n$	Number of transferred charge carriers
$Q$	Electrical charge / mAh
$Q_E$	Quality factor
$Q_{th}$	Theoretical capacity of an active material / mAh g <sup>-1</sup>
$\Delta f$	Frequency changes / Hz
$t$	Time / s
$T$	Temperature / K or °C
$T^\circ$	Standard ambient temperature (298.15 K or 25 °C)
$U$	Voltage / V
$z$	Valence number

## Figures

- Figure 1.** Operating principle of a RAB during charging, featuring Al metal as the negative electrode and graphite as the positive electrode in a Lewis acid chloroaluminate ionic liquid electrolyte consisting of  $\text{AlCl}_3$  and  $\text{EMImCl}$ . During charging, electrons ( $e^-$ ) flow to the Al negative electrode while  $\text{AlCl}_4^-$  ions move towards the graphite to intercalate..... 6
- Figure 2.** Timeline of electrolytes which developed in order to enable Al plating, highlighting the evolution from early molten salts to chloride-free electrolytes. <sup>26,27,31,49-82</sup> ..... 9
- Figure 3.** (a) TSC surface cell (b) the vertical section of the TSC Surface cell <sup>125</sup> (c) EL-CELL ECC-Opto-10 test cell mounted on a standard microscope sample stage (d) EL-CELL ECC-Opto-10 sample holder (side-by-side)<sup>162</sup> (e) EQCM Quartz Crystal Microbalance Gamry Instruments<sup>126</sup> (f) Electrodes arrangement in the Swagelok cell ..... 23
- Figure 4.** The Tafel extrapolation defines the corrosion current density ( $I_{\text{corr}}$ ) and corrosion potential ( $E_{\text{corr}}$ ) of AISI 316L in the A15E1 electrolyte. The intersection of the extrapolated anodic and cathodic branches determines these values. .... 26
- Figure 5.** CV curves on the Pt WE in ANU-2000 electrolyte at a scan rate of  $20 \text{ mVs}^{-1}$ . Al were used as reference electrode and counter electrode. .... 33
- Figure 6.** (a) Field emission-scanning electron microscopy (FE-SEM) and (b) energy-dispersive X-ray spectroscopy (EDX) images of the Pt WE polarized at  $-1 \text{ V vs. Al}$  for 2 hours in ANU-20000 electrolyte. .... 34
- Figure 7.** The Optical microscopy images of the Pt electrode were captured during CV measurement in the potential window of  $-1 \text{ V}$  to  $1.2 \text{ V vs. Al}$  at a scan rate of  $20 \text{ mVs}^{-1}$  in the ANU-20000 electrolyte. (a)  $-0.5 \text{ V vs. Al}$  (b)  $-1 \text{ V vs. Al}$  (c)  $0 \text{ V vs. Al}$  (d)  $1 \text{ V vs. Al}$ . .... 35
- Figure 8.** (a) GC spectrum of the collected gas after polarization of the Pt WE at  $-1 \text{ V vs. Al}$  for 30 min in the ANU-20000 electrolyte (contains  $<20000 \text{ ppm}$  of water) (b) GC spectrum of the collected gas from the atmosphere of the glovebox. The intensities of TCD responses are normalized with respect to the peak area of Ar from the glovebox atmosphere. .... 36
- Figure 9.** Electrode mass change vs. charge for the (a) 6<sup>th</sup> (b) 60<sup>th</sup> cycles, and potential vs. charge for the (c) 6<sup>th</sup> (d) 60<sup>th</sup> cycles during CV measurement at a scan rate of  $20 \text{ mVs}^{-1}$  on 5 MHz Pt-coated quartz crystal WE in the ANU-20000 electrolyte for cycles. The blue and black solid lines are measured mass change (EQCM), red and green lines are the theoretical mass change of neat ions calculated from Faraday's law. (f) The proposed mechanism. .... 38

<b>Figure 10.</b> (a) GC spectrum of the collected gas after polarization of the Pt WE at -1 V vs. Al for 30 min in the ANU-2000 electrolyte (containing <20000 ppm of water). (b) GC spectrum of the collected gas after polarization of the Pt WE at -1 V vs. Al for 1 hour in the electrolyte without urea Al(OTf) <sub>3</sub> /NMA=0.05/0.95 (c) GC spectrum of the collected gas from the atmosphere of the glovebox. The intensities of TCD responses are normalized with respect to the peak area of Ar from the glovebox atmosphere.....	39
<b>Figure 11.</b> Electrode mass change vs. charge for the (a) 6 <sup>th</sup> (b) 60 <sup>th</sup> cycles, and potential vs. charge for the (c) 6 <sup>th</sup> (d) 60 <sup>th</sup> cycles during CV measurement on 5 MHz Pt-coated quartz crystal WE in the Al(OTf) <sub>3</sub> /NMA electrolyte. The blue and black solid lines are measured mass change (EQCM), red and green lines are the theoretical mass change of neat ions calculated from Faraday's law. (f) The proposed mechanism. ....	41
<b>Figure 12.</b> CV curves on the Pt WE in the ANU-20000 electrolyte (containing <20000 ppm of water) and the ANU-300 electrolyte (containing 300 ppm of water) at a scan rate of 20 mVs <sup>-1</sup> . Al were used as reference electrode and counter electrode. ....	42
<b>Figure 13.</b> (a) GC spectrum of the collected gas after polarization of the Pt WE at -1 V vs. Al for 30 min in the ANU-2000 electrolyte (containing <20000 ppm of water). (b) GC spectrum of the collected gas after polarization of the Pt WE at -1 V vs. Al for 30 min in the ANU-300 electrolyte (containing 300 ppm of water) (c) GC spectrum of the collected gas from the atmosphere of the glovebox. The intensities of TCD responses are normalized with respect to the peak area of Ar from the glovebox atmosphere.....	43
<b>Figure 14.</b> Al 2s spectra of (a) the Pt WE after polarization at -1 V vs. Al for 2 hours in the ANU-300 (containing 300 ppm water) and (b) Al metal foil. ....	44
<b>Figure 15.</b> The chemical structure of the inhibitors EMImBF <sub>4</sub> (1-ethyl-3-methylimidazolium tetrafluoroborate), EMImOTf (1-ethyl-3-methylimidazolium trifluoromethanesulfonate), and Py <sub>1.4</sub> Cl (1-butyl-1-methylpyrrolidinium chloride).....	47
<b>Figure 16.</b> Potentiodynamic polarization curves for AISI 316L in various electrolytes with and without the presence of inhibitors. The polarization scan ranged from -0.5 V vs. OCV to 3 V vs. Al at a scan rate of 1 mVs <sup>-1</sup> . An Al CE and an Al pseudo-reference electrode were used.	49
<b>Figure 17.</b> CV curves of AISI 316L polarized from OCV up to 2.2 V vs. Al and scanned back again in A15E1Py2 and A15E1OTf2. Al foils were used as CE and pseudo-reference. The scan rate was 1 mVs <sup>-1</sup> .....	51
<b>Figure 18.</b> (a) Potentiodynamic polarization curves for W and AISI 316L in A15E1 electrolytes. The polarization scan ranged from -0.5 V vs. OCV to 3 V vs. Al at a scan rate of 1 mVs <sup>-1</sup> . An Al CE and an Al quasi-reference electrode were used. (b) CA measurement using	

the W working electrode, which is polarized at 1.5V vs. Al for 5 min in various electrolytes with and without inhibitors. An Al CE and an Al quasi-reference electrode were used. ....	52
<b>Figure 19.</b> The Fe 2p spectra for AISI 316L immersed in various electrolytes (a) Full spectra comparing the shapes with AISI 316L pristine foil and FeCl <sub>2</sub> spectra. (b) Fitted Fe 2p spectra highlighting the FeCl <sub>2</sub> satellite peak.....	54
<b>Figure 20.</b> N 1s spectra of AISI 316L samples immersed in different electrolytes, as well as the AISI 316L pristine foil. ....	56
<b>Figure 21.</b> F 1s spectra of AISI 316L samples immersion only in A15E1OTf2 and A15E1BF2. ....	57
<b>Figure 22.</b> Al 2p (a) and Cl 2p (b) spectra of AISI 316L samples immersed in different electrolytes .....	58
<b>Figure 23.</b> Fe 2p spectra for AISI 316L samples polarized at 1.5 V vs. Al for 1 minute (a) Full spectra comparing the shapes with AISI 316L pristine foil and FeCl <sub>2</sub> spectra. (b) Fitted Fe 2p spectra highlighting the Fe metal peak and FeCl <sub>2</sub> satellite peak. ....	60
<b>Figure 24.</b> N 1s spectra of AISI 316L samples polarized at 1.5 V vs. Al for 1 min in different electrolytes, as well as the AISI 316L pristine foil.....	61
<b>Figure 25.</b> F 1s spectra of AISI 316L samples polarized at 1.5 V vs. Al for 1 min A15E1OTf2 and A15E1BF2. ....	62
<b>Figure 26.</b> Al 2p (a) and Cl 2p (b) spectra of AISI 316L samples polarized at 1.5 V vs. Al for 1 min in different electrolytes .....	63
<b>Figure 27.</b> CV curves of the Al WE in various electrolytes, with and without inhibitors. The potential window scanned from -0.5 V to 1 V vs. Al at a scan rate of 10 mVs <sup>-1</sup> . A GC CE and an Al wire pseudo-reference electrode were used. The Al WE was cycled 50 times, and the curves for (a) the 1 <sup>st</sup> and (b) the 50 <sup>th</sup> cycles are shown. (c) the absolute value of the maximum Al plating current density vs. cycle number for various electrolytes. ....	65
<b>Figure 28.</b> CV curves of Al WE in various concentrations of the EMImBF <sub>4</sub> inhibitor at cycle numbers 1, 5, and 10. Al was used as the CE and pseudo-reference. The scan rate was 10 mV s <sup>-1</sup> . Concentrations are as follows: A15E1 (no inhibitor), A15E1BF1 (1 wt% inhibitor), A15E1BF2 (2 wt% inhibitor), A15E1BF5 (5 wt% inhibitor), and A15E1BF10 (10 wt% inhibitor). Increasing the inhibitor concentration led to greater limitations in Al plating and stripping.....	66
<b>Figure 29.</b> N 1s spectra of Al samples immersion in different electrolytes, the N cation can come from EMIm <sup>+</sup> cation and N neutral from the reduced EMIm.....	68



<b>Figure 30.</b> Al 2p (a) and Cl 2p (b) spectra of Al samples immersed for 10 minutes in different electrolytes. ....	70
<b>Figure 31.</b> F 1s and B 1s of Al immersed in A15E1BF2 electrolyte and F1s and S 2p spectra of Al immersed in A15E1OTf2 electrolyte.....	71
<b>Figure 32.</b> N 1s spectra of Al samples after 50 cycles in different electrolytes, the N cation can come from EMIm <sup>+</sup> cation and N neutral from the reduced EMIm. Al foil, GC disc, and Al wire were used as WE, CE, and pseudo-reference electrodes, respectively. The potential window scanned from -0.5 V vs. Al reference electrode to 1 V vs. Al pseudo-reference electrode at a scan rate of 10 mV s <sup>-1</sup> .....	73
<b>Figure 33.</b> Al 2p (a) and Cl 2p (b) spectra of Al samples after 50 cycles in different electrolytes. Al foil, GC disc, and Al wire were used as WE, CE, and pseudo-Reference electrodes, respectively. The potential window scanned from -0.5 V to 1 V vs. Al at a scan rate of 10 mV s <sup>-1</sup> .....	74
<b>Figure 34.</b> A comparison of intensities of Al 2p spectra of Al cycled in the electrolyte containing inhibitors and the Al pristine foil. ....	75
<b>Figure 35.</b> F 1s and B 1s of Al cycled for 50 times in A15E1BF2 electrolyte and F1s and S 2p spectra of Al cycled for 50 times in the A15E1OTf2 electrolyte. Al foil, GC disc, and Al wire were used as WE, CE, and pseudo-reference electrodes, respectively. The potential window scanned from -0.5 V vs. Al to 1 V vs. Al at a scan rate of 10 mV s <sup>-1</sup> .....	77
<b>Figure 36.</b> A graphical illustration highlighting the challenges faced in the research and development of rechargeable aluminum batteries. ....	80

## Tables

<b>Table 1.</b> The summarized research on Al plating in various electrolytes using the synthesized or commercially available Al salts with combination of different solvents. The green color shows Al plating and/or stripping being confirmed. The orange color means no Al plating and/or stripping was observed and the grey color presents that the study did not explicitly evaluate Al plating and stripping by utilizing characterization techniques such as SEM, and XPS. ....	17
<b>Table 2.</b> The materials used for experiments conducted in this study. ....	20
<b>Table 3.</b> The lists of the labels assigned to various electrolytes containing inhibitors, along with their concentrations. ....	22
<b>Table 4.</b> Calculated corrosion potentials and corrosion current densities from the Tafel slope extrapolations and the inhibition efficiency of the inhibitors in the electrolytes. ....	49

## Zusammenfassung

Wiederaufladbare Aluminium-Batterien (engl. Rechargeable aluminum batteries, RABs) gelten als vielversprechendes System zur Energiespeicherung. Aluminium (Al) ist in der Erdkruste reichlich vorhanden und bietet gegenüber Lithium (Li) Vorteile in Bezug auf Umweltverträglichkeit und Sicherheit. Um das volle Potenzial von RABs auszuschöpfen, müssen jedoch Herausforderungen im Bereich der Elektrolytchemie angegangen werden. Die reversible Al-Abscheidung und Auflösung stößt aufgrund verschiedener Faktoren auf Hindernisse, und die vorhandenen Elektrolyte, die Al-Abscheidung und Auflösung ermöglichen, sind hochkorrosiv. Diese Arbeit konzentriert sich daher auf die Bewältigung zweier kritischer Herausforderungen, die die Entwicklung von RABs behindern: (i) die Schwierigkeit, eine reversible Al-Abscheidung und Auflösung aus nicht-korrosiven Elektrolyten zu erreichen, und (ii) die Verringerung der Korrosivität von chloroaluminatbasierten ionischen Flüssigelektrolyten durch den Einsatz von Korrosionsinhibitoren.

Die Machbarkeit der Al-Abscheidung auf einer Platin (Pt)-Elektrode wurde unter Verwendung des  $\text{Al}(\text{OTf})_3/\text{NMA}/\text{urea}$  (ANU-20000) Elektrolyten als nicht-korrosive Alternative zu Chloroaluminat-basierten ionischen Flüssig-Elektrolyten untersucht. Zykelvoltammetrie-Experimente (CV) zeigten Redox-Aktivität auf Pt, aber weitere Analysen ergaben keine signifikante Al-Abscheidung. Stattdessen dominierte die Wasserstoffentwicklung den beobachteten Strom, was durch *operando* Mikroskopie und Gaschromatographie (GC)-Messungen bestätigt wurde. Dies wurde auf Restwasser im Elektrolyten zurückgeführt, welches die Wasserstoffentwicklungsreaktion (engl. Hydrogen evolution reaction, HER) fördert. Während das weitere Trocknen des Elektrolyten auf etwa 300 ppm  $\text{H}_2\text{O}$  (ANU-300) den HER-Strom verringerte, blieb die Al-Abscheidung unter den getesteten Bedingungen aus. Die gleichzeitige Adsorption/Desorption von  $\text{Al}(\text{OH})^{2+}$  und  $\text{Al}^{3+}$  Ionen auf der Pt-Oberfläche während der CV-Messungen wurde durch EQCM-Studien vorgeschlagen. Leider wurde auch im ANU-300 Elektrolyten keine erfolgreiche Al-Abscheidung erreicht. Dennoch wurden wertvolle Erkenntnisse über die unter den experimentellen Bedingungen ablaufenden Nebenreaktionen gewonnen. Die Identifizierung dieser Reaktionen, insbesondere derjenigen, die möglicherweise durch Restwasser (im vermeintlich getrockneten Elektrolyten) beeinflusst werden, ist entscheidend für die laufende Forschung an alternativen Elektrolyten für RABs.

Ein weiterer wichtiger Aspekt war die Verringerung der Korrosivität von chloroaluminatbasierten ionischen Flüssigelektrolyten durch den Einsatz von Korrosionsinhibitoren. Die stark korrosive Natur der chloroaluminatbasierten ionischen Flüssigelektrolyte begrenzt die Auswahl kompatibler Stromkollektormaterialien. Bestehende Optionen sind für praktische Anwendungen oft zu schwer oder zu teuer. Die Wirksamkeit von 1-Ethyl-3-methylimidazolium-Tetrafluoroborat (EMImBF<sub>4</sub>), 1-Ethyl-3-methylimidazolium-Trifluormethansulfonat (EMImOTf) und 1-Butyl-1-methylpyrrolidiniumchlorid (Py<sub>1,4</sub>Cl) Inhibitoren zur Verringerung der Korrosion von Edelstahl AISI 316L als potenzielle Stromkollektoren im chloroaluminatbasierten ionischen Flüssigelektrolyten aus AlCl<sub>3</sub> und EMImCl im Molverhältnis 1,5:1 wurde untersucht. Tafel-Plots und Röntgen-Photoelektronen-Spektroskopie (XPS)-Analysen zeigten, dass diese Inhibitoren am Ruhepotential (OCV) einen gewissen Korrosionsschutz bieten. Die Adsorption und Reduktion von Inhibitor-Kationen (EMIm<sup>+</sup> und Py<sup>+</sup>) auf der Oberfläche von AISI 316L kann der Grund für die begrenzte Korrosionsrate sein. Darüber hinaus ergab die XPS-Analyse die geringste Menge an Eisenchloridbildung auf der Oberfläche von AISI 316L, was auf die effektivste Korrosionsminderung durch EMImOTf am OCV und EMImBF<sub>4</sub> bei höheren Potenzialen hindeutet.

Jedoch beeinträchtigte die Gegenwart von Inhibitoren das Al-Abscheidungs- und Auflösungsverhalten, welches mittels zyklischer Voltammetrie untersucht wurde. Zwar zeigten alle Elektrolyte nach dem Laden und Entladen eine Erhöhung der Stromdichte bei der Al-Abscheidung und Auflösung, jedoch wurden die ersten Zyklen durch die Adsorption der Inhibitoren auf der Aluminiumoberfläche negativ beeinflusst. Dies verdeutlicht den Zielkonflikt zwischen Korrosionsschutz und dem Erzielen einer effizienten Al-Deposition und Ablösung. Bemerkenswerterweise wies der Elektrolyt mit EMImOTf den geringsten Einfluss auf die Al-Abscheidung und Auflösung im Vergleich zu anderen Elektrolyten mit Inhibitoren auf.

Zusammenfassend untersucht diese Arbeit die nachteilige Rolle von Nebenreaktionen bei der Al-Plattierung in Elektrolyten frei von AlCl<sub>3</sub>. Die Identifizierung dieser Reaktionen ist entscheidend für die Entwicklung leistungsfähiger Elektrolyte. Des Weiteren bietet ein Ansatz zur Verringerung der Korrosivität von chloroaluminatbasierten ionischen Flüssigelektrolyten durch den Einsatz von Inhibitoren wertvolle Erkenntnisse über das Verhalten der Inhibitoren auf den Oberflächen von Aluminium und Edelstahl AISI 316L. Die Studie deckte eine

unerwartete Konsequenz auf: Inhibitoren wirken sich negativ auf die Al-Abscheidung und Auflösung an der negativen Elektrode aus. Diese Erkenntnisse liefern ein tieferes Verständnis der Herausforderungen bei der Anwendung von Korrosionsinhibitoren in Elektrolyten für RAB-Technologien.

## Abstract

Rechargeable aluminum batteries (RABs) hold great promise as an energy storage system. Aluminum (Al), abundant in Earth's crust, offers advantages over lithium (Li) in terms of environmental impact and safety. Nevertheless, gaining the full potential of RABs requires addressing challenges related to electrolyte chemistry. The reversible Al plating and stripping process faces obstacles due to various factors, and the existing electrolytes that facilitate Al plating and stripping are highly corrosive. This thesis focuses on tackling two critical challenges hindering the RABs development: (i) struggle to achieve reversible Al plating and stripping from non-corrosive electrolytes and (ii) mitigating the corrosivity of chloroaluminate-ionic liquid electrolytes through the application of corrosion inhibitors.

The feasibility of Al plating on a platinum (Pt) electrode was explored using trifluoromethanesulfonate ( $\text{Al}(\text{OTf})_3$ )/*N*-methylacetamide (NMA)/urea (ANU-20000) electrolyte as a non-corrosive alternative composition to chloroaluminate-based ionic liquid electrolytes. Cyclic voltammetry measurements (CV) indicate redox activity on Pt, but further analysis reveals no meaningful Al plating. Instead, hydrogen evolution reaction (HER) dominates the observed current, confirmed by *operando* microscopy and gas chromatography (GC) measurements. The residual water in the electrolyte promotes the HER. While further drying the electrolyte, up to approximately 300 ppm of  $\text{H}_2\text{O}$  (ANU-300), reduced the HER current, Al plating remained elusive under the tested conditions. The concurrent adsorption/desorption of  $\text{Al}(\text{OH})^{2+}$  and  $\text{Al}^{3+}$  ions on the Pt surface during CV measurements was proposed according to electrochemical quartz crystal microbalance (EQCM) studies. Unfortunately, no successful Al plating was achieved even in the ANU-300 electrolyte. Yet, valuable insights were gained into the side reactions occurring under the experimental conditions. Identifying these reactions, particularly those potentially influenced by residual water (in the supposedly dried electrolyte), is crucial for the ongoing research into alternative electrolytes for RABs.

Another crucial aspect was mitigating the corrosivity of the chloroaluminate ionic liquid electrolytes using corrosion inhibitors. The highly corrosive nature of the chloroaluminate ionic liquid electrolytes limits compatible current collector materials. Existing options are often excessively dense or expensive for practical applications. The effectiveness of 1-Ethyl-3-methylimidazolium tetrafluoroborate ( $\text{EMImBF}_4$ ), 1-Ethyl-3-methylimidazolium

trifluoromethanesulfonate (EMImOTf), and 1-Butyl-1-methylpyrrolidinium chloride (Py<sub>1.4</sub>Cl) inhibitors in mitigating the corrosion of AISI 316L stainless steel as potential current collectors in the chloroaluminate ionic liquid electrolyte composed of AlCl<sub>3</sub> and EMImCl with the molar ratio of 1.5:1 was investigated. Tafel plots and X-ray photoelectron spectroscopy (XPS) analysis revealed that these inhibitors offered a degree of corrosion protection at the open-circuit voltage (OCV). The adsorption and reduction of inhibitor cations (EMIm<sup>+</sup> and Py<sup>+</sup>) on the AISI 316L surface can be the reason for the limited corrosion rate. Moreover, XPS analysis revealed the least amount of iron chloride formation on the AISI 316L surface, indicating the most effective corrosion mitigation by EMImOTf at OCV and EMImBF<sub>4</sub> at higher potentials.

However, the presence of inhibitors affected Al plating and stripping behavior as evaluated by CV. While all electrolytes exhibited an increase in Al plating and stripping current density after cycling, the initial cycles were negatively affected by the inhibitor adsorption on the surface of Al. This highlights a trade-off between corrosion protection and achieving efficient Al plating/stripping. Notably, the electrolyte containing EMImOTf demonstrated the least impact on Al plating/stripping compared to other inhibitor-containing electrolytes.

Overall, this study explores the detrimental role of side reactions in Al plating within the AlCl<sub>3</sub>-free electrolyte. Identifying these reactions is crucial for the development of efficient electrolytes. Secondly, an approach to mitigate the corrosivity of chloroaluminate ionic liquid electrolytes by incorporating inhibitors provides valuable insights into the inhibitor's behavior on Al and AISI 316L surfaces. It revealed an unexpected consequence: the inhibitor negatively impacts Al plating and stripping at the negative electrode. These findings offer a deeper understanding of the challenges of applying the corrosion inhibitor in the electrolytes for RAB technologies.

# 1 Introduction and Motivation

The growing demand for energy storage is driven by two major forces: the rapid electrification of transportation through electric vehicles (EVs), and the increasing integration of renewable energy sources like solar and wind power.<sup>1</sup> While these advancements are crucial for fighting against climate change, they introduce a significant challenge – grid instability. Unlike traditional fossil fuel sources, renewable energy sources are intermittent, which means their availability fluctuates depending on weather conditions. To ensure a reliable and secure energy supply, efficient and scalable energy storage systems are paramount.

While Lithium-ion batteries (LIBs) currently dominate the market due to their high energy densities, concerns regarding resource availability, price fluctuations, and environmental impact associated with key components like lithium (Li), nickel (Ni), and cobalt (Co), require exploring other battery technologies as well.<sup>1–7</sup>

Recognizing the limitations of LIBs, other battery technologies including sodium (Na), potassium (K), magnesium (Mg), aluminum (Al), calcium (Ca), and zinc (Zn) battery technologies have garnered significant interest.<sup>8,9,18,19,10–17</sup>

Among them, Al arises as a promising candidate due to its abundant sources on the earth's crust, lower environmental impact, and inherent safety compared to Li. Theoretically, bulk Al is able to offer a significantly higher volumetric capacity of 8046 mAh cm<sup>-3</sup> (nearly four times that of Li with 2062 mAh cm<sup>-3</sup>) due to the trivalent nature of Al ion, allowing for more efficient energy storage. Additionally, Al offers comparable gravimetric capacity to Li (2980 mAh g<sup>-1</sup> for Al and 3860 mAh g<sup>-1</sup> for Li) and it is stable under ambient conditions, ensuring safe handling, especially in case of accidental breakage of the battery cell.<sup>20–25</sup>

However, realizing the full potential of RABs requires overcoming challenges related to electrolyte chemistry. Developing an electrolyte that facilitates reversible Al plating and stripping is challenging, due to strong interactions between Al cations and their counter-ions.<sup>26</sup> Those electrolytes that enable Al plating and stripping exhibit high corrosiveness, attacking various cell components including stainless steel current collectors or even the often-used coin cells.<sup>5,6,20</sup> This corrosion compromises their suitability for practical applications. Research has been conducted to address this issue, exploring various electrolyte systems ranging from early experiments with molten salts to more recent advancements in liquid polymer electrolytes.<sup>4,22,23,25,27–31</sup>



The transition to sustainable energy sources necessitates the exploration of battery technologies beyond lithium-ion, highlighting the critical role of RABs development. This dissertation explores two primary approaches to address the critical challenge of the RABs electrolytes:

**1- Investigation of a non-corrosive electrolyte:**

This section delves deeper into the understanding of an electrolyte based on aluminum tris(trifluoromethanesulfonate) salt ( $\text{Al}(\text{OTf})_3$ ), which has been previously reported with claims of successful Al plating and stripping,<sup>15</sup> though concrete evidence has been lacking. Therefore, a comprehensive exploration of this electrolyte is essential to demonstrate Al plating and stripping from this electrolyte, which can help uncover the key to achieving reliable Al plating and stripping.

**2- Mitigating corrosivity of chloroaluminate ionic liquid electrolytes:**

This approach focuses on incorporating inhibitors into chloroaluminate ionic liquid electrolytes. The aim is to create a protective film on ASIS 316L as a potential current collector and prevent its corrosion while enabling reversible Al plating and stripping.

By addressing these challenges, this research aspires to pave the way for the development of RABs, ultimately contributing to a cleaner and more secure energy future.

## 2 Theoretical background

### 2.1 Key parameters of battery electrochemistry

Rechargeable battery cells, typically consist of two electrodes that are electronically conductive and separated by an ion-conductive electrolyte phase. These electrochemical cells function through reversible electrochemical reactions, enabling them to undergo multiple charge and discharge cycles.

This cyclic operation hinges on the electrolyte's ability to facilitate the smooth movement of charged ions between the negative and positive electrodes during charge and discharge cycles. Therefore, a key parameter for the electrolyte is its ionic conductivity. Equally important is the stability of the electrolyte within the operational voltage window of the battery. It must withstand the operating voltage without degrading, ensuring long-term battery performance.

During cell discharge, the electrode where oxidation reactions take place (loss of electrons) is called the anode, while the electrode undergoing reduction reactions (gain of electrons) is called the cathode. During the charging process, an external electrical current drive positively charged ions from the cathode toward the anode, essentially storing energy in the system. Conversely, when the battery discharges, the process reverses, and the stored energy is released as the ions flow back from the anode to the cathode, powering the connected device. For the sake of clarity, the terminology of "negative electrode" and "positive electrode" throughout the rest of this discussion will be used instead of more technical terms of anode and cathode.

The voltage of a cell is determined by the potential difference between the two electrodes. To achieve a high cell voltage, the positive electrode should ideally have a relatively high potential, while the negative electrode should have a low potential. This potential difference between the electrodes acts as the driving force for the flow of electrons in the external circuit and ions' movement within the electrolyte.

Cell capacity, another critical parameter, refers to the amount of electrical charge ( $Q$ ) a battery can store or deliver. This capacity is directly proportional to the time ( $t$ ) in which a constant current ( $I$ ) can be applied and is typically measured in milliampere-hours per gram (mAh g<sup>-1</sup>) as per standard battery nomenclature.

$$Q = I * t \tag{1.}$$

However, it is important to understand the concept of theoretical capacity. The theoretical capacity of an active material within a battery can be calculated using a specific formula mentioned in equation (2).

$$Q_{th} = \frac{z * n * F}{M} \quad (2.)$$

that considers the maximum number of ions that can be inserted and/or extracted ( $n$ ), Faraday's constant of 96485 C mol<sup>-1</sup> ( $F$ ), the valence number of the charge carrier ( $z$ ), and the molecular mass of the active material ( $M$ ).<sup>32</sup>

Unfortunately, cells rarely achieve their full theoretical capacity due to various factors. Inefficiencies in the charging and discharging processes, limitations of the electrode materials themselves (such as their ability to reversibly accept and release ions as well as material defects), side reactions, and cycle life (the number of charge-discharge cycles a battery can undergo before significant degradation) all contribute to this gap between theoretical and practical capacity.

Gravimetric capacity and volumetric capacity refer to the maximum amount of charge a cell can hold per unit mass, typically measured in milliampere-hours per gram (mAh g<sup>-1</sup>) and the amount of charge stored per unit volume, commonly in milliampere-hours per cubic centimeter (mAh cm<sup>-3</sup>). In simpler terms, it tells us how much energy a cell can store per unit of its weight or volume. Both the theoretical gravimetric and volumetric capacities depend on the specific chemistry employed in the cell. Different battery chemistries, such as Li, Al, or Na, utilize different electrode materials and reaction mechanisms, leading to distinct capacity values.

Finally, specific energy ( $\varepsilon$ ), measured in Watt-hours per kilogram (Wh kg<sup>-1</sup>), is another key parameter that represents the energy stored per unit mass of the cell. This value is calculated by dividing the total energy delivered during discharge (in Watt-hours) by the mass of the cell mass

$$\varepsilon = \frac{1}{3600 * m} \int_{t_i}^{t_f} I(t) * U(t) dt \quad (3.)$$

In the mentioned equation,  $m$  is electrode active mass in kg,  $I$  is current in A,  $U$  is cell voltage in V and  $t_i$  and  $t_f$  are initial time and final time of charge/discharge in s.<sup>33</sup> In equation (3), integration arises from the need to account for the varying voltage during discharge.

## 2.2 Understanding of rechargeable aluminum batteries (RABs)

RABs fall under the category of secondary batteries, offering the advantage of repeated charging and discharging cycles. Unlike their counterparts that rely on alkali metals like Li and Na, RABs utilize Al foil as the negative electrode. This is a significant advantage as Al is inherently stable under ambient conditions, making it easier and safer to handle compared to highly reactive alkali metals and in theory can yield to a higher volumetric capacity.

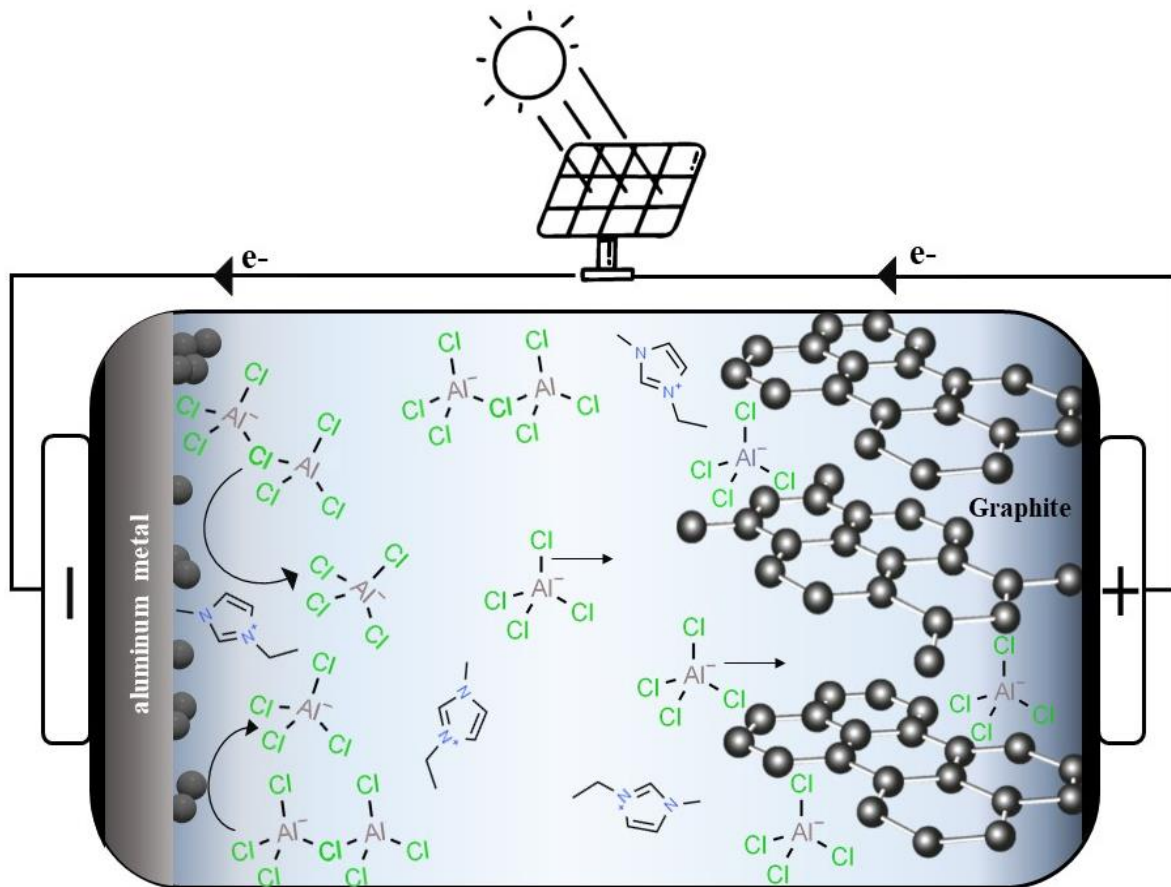
The positive electrode in RABs can be made from various materials, including carbon-based compounds (like graphite), organic compounds and polymers (such as polypyrrole), and transition metal oxides (like  $V_2O_5$  or  $Mn_2O_4$ ), transition metal chalcogenides which can be tailored to the properties of the battery to specific requirements.<sup>34–37</sup> Since carbon-based materials are the most commonly used cathodes in RABs with chloroaluminate ionic liquid electrolytes, the following section focuses on graphite<sup>37</sup>.

The electrolyte used in RABs plays a crucial role in their performance. A more detailed discussion on electrolytes used in RABs to date will be provided in chapter 2.3. However, it is worth noting that unlocking the full potential of RABs requires addressing challenges related to electrolyte chemistry and developing an electrolyte which facilitate the reversible plating and stripping of Al ions or complexes. This difficulty is mostly due to strong interactions between Al cations and their counter-ions as well as solvent molecules.<sup>26</sup> This highlights a crucial point: beyond the general characteristics of the electrolyte, such as ionic conductivity, the specific species present within the electrolyte significantly influence the battery's performance.

However, this section focuses specifically on chloroaluminate ionic liquid electrolytes, particularly the most commonly used variant containing 1-Ethyl-3-methylimidazolium chloride (EMImCl). To illustrate the basic operating principle of RABs, an example using a chloroaluminate ionic liquid electrolyte composed of aluminum chloride ( $AlCl_3$ ) and EMImCl is presented.

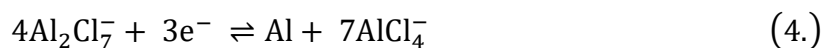
A simple schematic of the RABs configuration during the charging process is presented in Figure 1, featuring an Al foil as the negative electrode and graphite as the positive electrode, using a predominant Lewis acid chloroaluminate ionic liquid electrolyte ( $AlCl_3$ :EMImCl with

a molar ratio exceeding 1). In this electrolyte, Al complexes of  $[\text{AlCl}_4]^-$  and  $[\text{Al}_2\text{Cl}_7]^-$  are present.

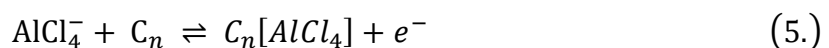


**Figure 1.** Operating principle of a RAB during charging, featuring Al metal as the negative electrode and graphite as the positive electrode in a Lewis acid chloroaluminate ionic liquid electrolyte consisting of  $\text{AlCl}_3$  and  $\text{EMImCl}$ . During charging, electrons ( $e^-$ ) flow to the Al negative electrode while  $[\text{AlCl}_4]^-$  ions move towards the graphite to intercalate.

During charging, Al species from the electrolyte migrate towards the negative electrode, readily plating onto the Al foil by the following redox reaction



Simultaneously, negatively charged  $[\text{AlCl}_4]^-$  intercalate into the layered structure of the graphite as a positive electrode through the following reaction



This synchronized exchange of ions is the core mechanism by which energy is stored within the Al battery.<sup>20,38</sup>

It is important to mention that intercalation of  $[\text{AlCl}_4]^-$  can lead to the expansion of the positive electrode material due to their larger volume compared to single  $\text{Al}^{3+}$  ions. However, graphite can maintain its stacking pattern even after the interaction of  $[\text{AlCl}_4]^-$ .<sup>39</sup>

### 2.2.1 Key points when discussing RABs

- Realistic rechargeable capacities

A significant difficulty lies in the discrepancy between the theoretical and experimental capacity of RABs. The theoretical gravimetric capacity of RABs needs careful consideration based on the Al plating reaction at the negative electrode during charging. This reaction requires 8 Al atoms to transfer 3 electrons. Consequently, the maximum achievable capacity for an RAB system using a typical chloroaluminate electrolyte is around  $67 \text{ mAh g}^{-1}$ . This value falls short of the often-cited theoretical capacity of  $2980 \text{ mAh g}^{-1}$ , which considers the metallic Al deposition and dissolution rather than Al plating and stripping through redox active species in the electrolyte. Moreover, intercalation of  $[\text{AlCl}_4]^-$  into the graphite structure (as an example) instead of  $\text{Al}^{3+}$  ions not only causes the volume expansion of graphite but also an average of 36 repeating units of carbon atoms is needed per  $[\text{AlCl}_4]^-$  for the intercalation. This reduces the overall energy density of the battery by diluting the carbon mass.<sup>40</sup>

- Electrolyte volume

Electrolyte volume in RABs is a critical factor that demands careful consideration. Electrolyte species, particularly  $[\text{Al}_2\text{Cl}_7]^-$ , play a vital role in the reversible plating and stripping of Al at the negative electrode (refer to equation (4)). Since redox activity is correlated to the species in the electrolyte during charge and discharge cycles, ensuring a sufficient amount of electrolyte is present within the system is crucial. Consumption of electrolyte species during charging can negatively impact the overall energy density of the RAB.

The specific capacity of a RAB is essentially determined by the combined capacities of the negative and positive electrodes. While altering the molar ratio of the electrolyte might not significantly affect the capacity of the positive electrode, it has a profound impact on the capacity of the negative electrode and consequently, the overall specific capacity of the RAB. This is because the capacity of the negative electrode is not directly related to the mass of Al

metal used, but rather the chloroaluminate complex available within the electrolyte that can be plated during charging, in particular  $[\text{Al}_2\text{Cl}_7]^-$ .<sup>20</sup>

The presence of  $[\text{Al}_2\text{Cl}_7]^-$ , the key species responsible for reversible Al plating and stripping, is directly dependent on the molar ratio of  $\text{AlCl}_3$  to EMImCl in the electrolyte. Consequently, the capacity of the negative electrode, and the entire RAB, is intricately linked to both the volume and the molar ratio of the electrolyte.<sup>20</sup> Research has shown that increasing the  $\text{AlCl}_3$ :EMImCl ratio from 1.3 to 2 can significantly enhance the energy density of the RAB, from 33 Wh  $\text{kg}^{-1}$  to 62 Wh  $\text{kg}^{-1}$ , at an average operating voltage of 1.4 V.<sup>41</sup>

This highlights a crucial point: while maintaining a high  $\text{AlCl}_3$ :EMImCl ratio (greater than 1) is generally necessary to create a Lewis acid electrolyte containing  $[\text{Al}_2\text{Cl}_7]^-$  for reversible Al plating and stripping, the optimal ratio plays a significant role in the overall performance of the RABs.

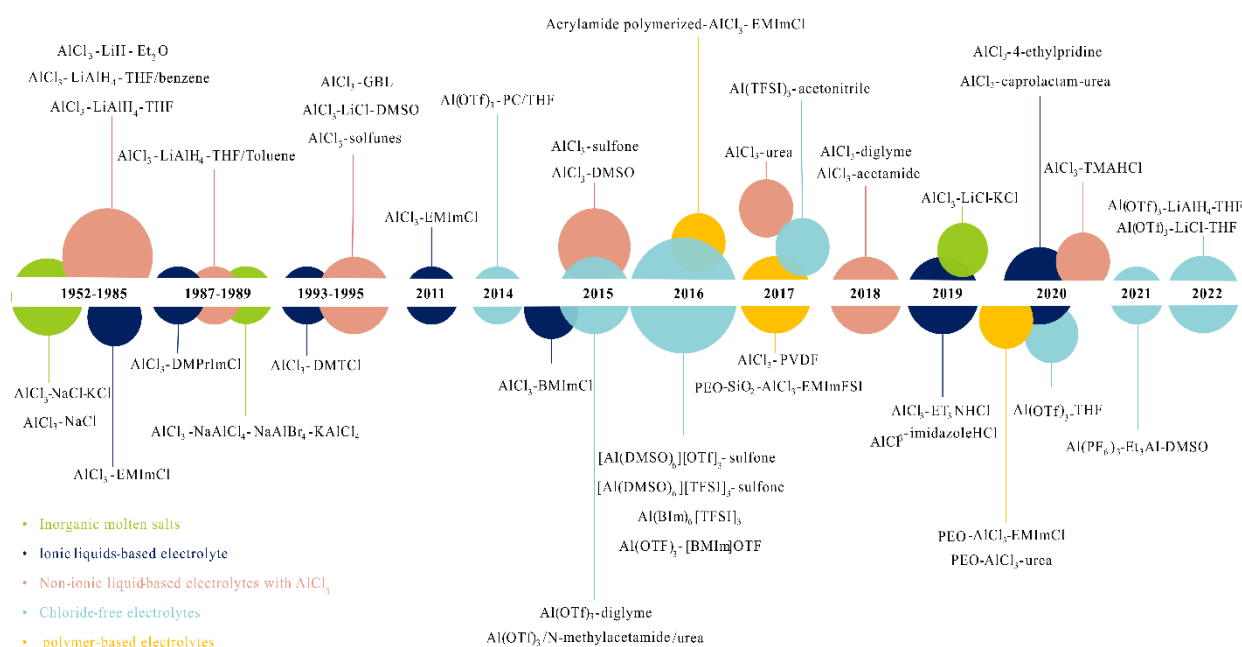
- Current collector selection

The current collector acts as a bridge, establishing an electrical connection between the active material of the electrode and the external circuit. Ideally, the current collector should be stable in the electrolyte and compatible with the operating voltage window. Metals (*e.g.*, copper (Cu), stainless steel (AISI), aluminum (Al), and titanium (Ti)) are typically preferred as current collectors due to their good conductivity. However, in RABs using chloroaluminate ionic liquid electrolytes, commonly used metals can be susceptible to corrosion. The corrosive nature of these electrolytes can damage and degrade the current collectors, compromising their structural integrity and ultimately affecting battery performance.<sup>42</sup>

One effective strategy to hinder corrosion in general, involves the use of corrosion inhibitors. These inhibitors, established in the field of corrosion science, mitigate corrosion by forming a protective layer on the metal surfaces. This protective layer acts as a barrier that shields the metal from direct contact with the aggressive electrolytes. By hindering the access of the electrolyte to the metal surface, inhibitors effectively reduce corrosion rates.<sup>43–48</sup> Corrosion inhibitors are widely used across various industries to protect metals like mild steel and stainless steel in harsh environments such as seawater or acidic industrial solutions. This research leverages established knowledge from corrosion science to evaluate the effectiveness of these inhibitors in mitigating the corrosion of current collectors within RAB cells.

## 2.3 Electrolyte evolution in RABs: A journey from molten salts to chloride-free organics

Besides discussing the components used in the cell, more details are provided in this section about the electrolytes used in RABs. The electrolyte, which provides a medium for ionic conductivity, is necessary for the electrochemical reaction to occur which significantly impacts the performance of the cell. Figure 2 illustrates the timeline of electrolytes used in the Al plating process, showcasing the progression from early molten salts to polymer-based electrolytes. 26,27,56–65,31,66–75,49,76–82,50–55 The following section will provide a detailed overview of various electrolyte categories.



**Figure 2.** Timeline of electrolytes which developed in order to enable Al plating, highlighting the evolution from early molten salts to chloride-free electrolytes. 26,27,56–65,31,66–75,49,76–82,50–55

### 2.3.1 High-temperature molten salts electrolytes

Indeed, the development of RABs involves the incorporation of high-temperature chloroaluminate molten salts. These electrolytes mostly consist of Al chlorides combined with alkali metal chlorides, each of them, separately, has a high melting point individually. However, by mixing these metal halides, the binary or ternary molten salt mixtures are forming, and the melting point can be significantly reduced. These electrolytes typically function within a temperature range of 100-200 °C.<sup>83</sup>



Historically, these molten salts were used in the field of Al plating, where they were initially employed as protective layers on various substrates. However, their application in RABs represents a novel utilization within the battery field.<sup>84–86</sup>

In 1972, Holleck *et al.*<sup>73</sup> first explored the use of a ternary mixture of aluminum chloride-potassium chloride-sodium chloride ( $\text{AlCl}_3\text{-KCl-NaCl}$ ) in RABs, employing Al metal as the anode.<sup>73</sup> Researchers then synthesized a ternary electrolyte composed of  $\text{AlCl}_3$ , lithium chloride ( $\text{LiCl}$ ), and  $\text{KCl}$ .<sup>74</sup> This electrolyte exhibits a low melting point of around 95 °C. An Al/graphite battery incorporating this electrolyte delivered a substantial capacity of 107 mAh g<sup>-1</sup> at 99 °C. Furthermore, the battery exhibited excellent rate capability, recovering 97.9% of its capacity after repeated cycling at high current densities (500 mA g<sup>-1</sup>). Additionally, it demonstrated a long cycle life with high coulombic efficiency.<sup>74</sup>

However, the practical application of high-temperature chloroaluminate molten salt electrolytes has been hindered by factors such as the high operating temperatures, dendrite formation during Al plating, and the formation of chlorine gas ( $\text{Cl}_2$ ), which poses health risks.<sup>73</sup> Subsequently, room-temperature chloroaluminate ionic liquids (ILs) replaced molten salt electrolytes in RABs.

### **2.3.2 Room-temperature chloroaluminate ionic liquid electrolyte**

Ionic liquids, discovered nearly a century ago, offer a solution to the high operating temperatures required by molten salt electrolytes. Room-temperature ionic liquids (RTILs) consist entirely of salts and often have a melting point below 100°C. They possess excellent physical and chemical properties such as low flammability, low vapor pressure, relatively high ionic conductivity, electrochemical stability, and wide electrochemical windows, making them highly attractive as electrolytes for RABs.<sup>22,87–89</sup>

The history of ionic liquids is multifaceted, with various independent discoveries contributing to their development. The point particularly interesting in ionic liquids development is the substitution of alkali metal cations (such as Na, Ca) of the high-temperature molten salt electrolytes with long-chain organic cations.<sup>90,91</sup> This substitution lowers the melting point, resulting in RTILs that operate effectively at ambient temperatures, offering operational ease compared to high-temperature alternatives.<sup>20,21,92,93</sup>

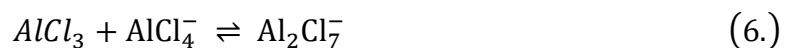
Research over the years has paved the way for RTILs as electrolytes in RABs.<sup>27,75–77</sup> The type of cation in the RTILs significantly impacts the electrolyte's viscosity, melting point, and ionic

conductivity. Imidazolium cations ( $M^+$ ) with varying alkyl chains, such as 1-Butyl-3-methylimidazolium ( $BMIM^+$ ) and 1-Ethyl-3-methylimidazolium ( $EMIM^+$ ), are the most explored for this application,<sup>94,95</sup> while  $Cl^-$  is the most common anion ( $X^-$ ), other halogens like bromide ( $Br^-$ ) and iodide ( $I^-$ ) can also be used with imidazolium cations. However, RABs rely predominantly on chloride  $Cl^-$  due to its superior conductivity and electrochemical stability compared to  $Br^-$  and  $I^-$ . Notably, increasing the ionic radius of the anion reduces ionic conductivity and narrows the electrochemical stability window, as a higher HOMO (highest occupied molecular orbital) energy level in the anion leads to easier oxidation.<sup>96</sup>

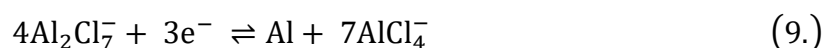
Chloroaluminate ionic liquid electrolytes, consisting of  $AlCl_3$  and  $EMImCl$ , are one of the most studied electrolytes in RABs.<sup>78</sup> Al plating in RTIL electrolytes is primarily determined by the concentration of Al salt and the equilibrium between various anionic species, as Al-complexes exist rather than free  $Al^{3+}$ .<sup>58,97</sup> Depending on the molar ratio of  $AlCl_3$  to  $EMImCl$ , the electrolyte can be basic, neutral, or acidic, which affects the dominant species present of tetrachloroaluminate ( $[AlCl_4]^-$ ) and/or heptachlorodialuminate ( $[Al_2Cl_7]^-$ ).<sup>29,98–101</sup>

When the ratio of  $AlCl_3$  to (1-Ethyl-3-methylimidazolium chloride)  $EMImCl$  is equal to or lower than 1, the electrolyte is considered neutral and basic respectively. In the neutral electrolyte,  $[AlCl_4]^-$  anionic species would be presented while in the basic electrolyte, the coexisting anionic species of  $[AlCl_4]^-$  and  $Cl^-$  would be expected.<sup>102,103</sup>

In contrast, when the molar ratio of  $AlCl_3$  to  $EMImCl$  exceeds 1 (known as an acidic electrolyte), the dominant species becomes  $[Al_2Cl_7]^-$ , which coexists with  $[AlCl_4]^-$  through reversible self-ionization through reactions (6) and (7):<sup>4,104</sup>



Al plating can occur through reactions (8) and (9), although only reaction (9) is reversible. The reduction of  $[AlCl_4]^-$  to Al requires higher temperatures, leading to the irreversibility of the reaction due to the reduction of organic cations before  $[AlCl_4]^-$ .<sup>105</sup> Therefore,  $[Al_2Cl_7]^-$  is believed to be the "active" species, and its presence is essential for reversible Al stripping and plating, meaning that a Lewis acid RTIL electrolyte is necessary.<sup>102,104,106</sup>



The acidity of electrolytes can be advantageous for removing the protective oxide layer on the Al metal surface, allowing reactions at the negative electrode. However, the extreme corrosivity of chloroaluminate ionic liquids can lead to corrosion, posing safety hazards and complicating the selection of compatible current collector materials and auxiliary parts of the battery.<sup>5,6,20,107</sup> Stainless steels, for example, experience severe corrosion, hindering the use of traditional coin cells.<sup>5</sup>

Moreover, the  $[\text{Al}_2\text{Cl}_7]^-$  species exhibit high sensitivity to moisture.<sup>4,20,108</sup> To address this challenge, the  $[\text{AlCl}_2(4\text{-Pr-Py})_2]^+$  complex, representing a cationic electroactive species, has been investigated, by employing a neutral ligand, 4-propylpyridine, in a molar ratio of 1.3:1. In  $\text{AlCl}_3$ :4-propylpyridine electrolyte, Al plating facilitated through this complex, alongside with  $[\text{Al}_2\text{Cl}_7]^-$ , which presents a promising alternative to conventional chloroaluminate ionic liquids.<sup>108</sup> Yet, optimizing cell performance while mitigating the corrosivity of RTILs remains a significant challenge in battery research.

### 2.3.3 Non-ionic liquid electrolytes with $\text{AlCl}_3$

To potentially reduce the corrosiveness of the electrolyte, researchers investigated the use of  $\text{AlCl}_3$  salt in organic solvents. Various solvents such as tetrahydrofuran (THF), acetonitrile (ACN), and gamma-butyrolactone (GBL) were explored by different research groups (summarized in Table 1).<sup>54,55,57</sup> However, some of these studies did not investigate the possibility of reversible Al plating and stripping, as they were not oriented toward battery research.

One of the limiting factors in these studies can be a low concentration (around 1 M) of  $\text{AlCl}_3$  in the organic solvent, leading to the formation of  $[\text{AlCl}_4]^-$  and  $[\text{AlCl}_2(\text{solvent})_n]^{2+}$  in the electrolyte. However, as the presence of a Lewis acidic anion like  $[\text{Al}_2\text{Cl}_7]^-$  is necessary for reversible Al plating and stripping, most of these studies have failed to obtain such a reversible process. Increasing the  $\text{AlCl}_3$  salt concentration in organic solvents reached a critical concentration, usually a 1:1 molar ratio of solvent to salt, results in a behavior similar to ionic liquids, termed "solvate ionic liquids".<sup>109,110</sup> Some examples of such electrolytes are discussed below.

Increasing the concentration of  $\text{AlCl}_3$  salts in sulfones as solvents facilitated the formation of Lewis acid anions such as  $[\text{Al}_2\text{Cl}_7]^-$ , enabling Al plating at room temperature. However, concerns about corrosivity and low anodic stability persist.<sup>51</sup>

Using  $\text{AlCl}_3$  in GBL as an organic solvent, with a molar ratio of  $\text{AlCl}_3\text{:GBL} = 1.5\text{:}1$ , allows the formation of the electrochemically active  $[\text{Al}_3\text{Cl}_{10}]^-$  anion, resulting in Al plating, however, no Al stripping from this electrolyte was observed.<sup>55</sup>

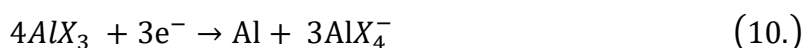
$\text{AlCl}_3$ /diglyme ( $\text{G}_2$ ) electrolytes result in the formation of cationic active species  $[\text{AlCl}_2(\text{G}_2)_2]^+$  which allowed for successful Al plating and stripping, despite a lower molar ratio of  $\text{AlCl}_3$  compared to conventional chloroaluminate ionic liquid, making it less corrosive.<sup>53</sup> However, Al plating was not observed with triglyme ( $\text{G}_3$ ) and tetraglyme ( $\text{G}_4$ ) solvents, possibly due to stronger interactions between Al-cations and these solvents.<sup>53</sup>

In brief, it seems that investigation of  $\text{AlCl}_3$  in organic solvents holds potential for improving electrolyte performance in terms of reversible Al plating/stripping.

### 2.3.4 Al halides-based electrolytes

A combination of  $\text{AlCl}_3$  with metal hydrides such as lithium hydride ( $\text{LiH}$ ) or lithium aluminum hydride ( $\text{LiAlH}_4$ ) in organic solvents, has been explored in earlier research as a deposition bath for plating of Al onto substrates on an industrial scale. The initial investigations focused on  $\text{AlCl}_3$  with  $\text{LiH}$  in diethyl ether ( $\text{Et}_2\text{O}$ ) as the solvent.<sup>56</sup> While successful Al plating was achieved using this electrolyte, subsequent studies explored less volatile solvents like THF along with various additives and solvent combinations, as summarized in Table 1.

These investigations delved into several key aspects, including the mechanism of Al plating (with different molar ratios of  $\text{AlCl}_3$  and  $\text{LiAlH}_4$  in THF), the ionic conductivity of the electrolytes, the quality of the plated Al layer in terms of smoothness and homogeneity, and the plating current density.<sup>57–62</sup> The findings suggest that higher molar ratios of  $\text{LiAlH}_4$  to  $\text{AlCl}_3$  enhance Al plating by promoting the charge transfer process facilitated by hydride ( $\text{H}^-$ ).<sup>59–62</sup> Additionally, using a mixture of THF with benzene or toluene increases the current densities for Al plating.<sup>57,58</sup> In summary, these studies provide valuable insights into the feasibility of Al plating from  $\text{AlCl}_3/\text{LiAlH}_4$  in THF solution through the overall reaction.<sup>59</sup>



where  $X$  can be H or Cl.

However, since these systems were not originally designed for RABs, investigations on the possibility of reversible Al plating and stripping in this electrolyte remain unexplored.

It appears that Lewis acids, like  $\text{AlCl}_3$ , play a crucial role in the Al plating and stripping process, but they possess inherent corrosiveness. Surprisingly, existing research lacks quantitative data on the corrosivity of these electrolytes and their comparison to chloroaluminate ionic liquid electrolytes. Ultimately, achieving truly practical RABs demands the development of chloride-free systems that address these limitations.

### 2.3.5 Chloride-free electrolytes

The pursuit of chloride-free Al electrolytes to mitigate corrosion necessitates the exploration of alternative salts to  $\text{AlCl}_3$  salt. However, this path presents several challenges. Firstly, the options for commercially available Al salts with weakly coordinating anions are limited.<sup>63</sup> Secondly, even readily available options like  $\text{Al}(\text{OTf})_3$  raise concerns regarding their ability to effectively dissociate in the electrolyte, which can negatively impact the solubility and electrochemical activity of  $\text{Al}^{3+}$  cations.<sup>68,111</sup> Finally, the stability of the anions during Al plating and stripping is a potential pitfall. Since decomposing fluoride anions may lead to the formation of insulating surface compounds like fluorides.<sup>112</sup> These hinder the crucial reversible Al plating and stripping process. Therefore, identifying an electrolyte combination that utilizes a stable, weakly coordinating anion for the Al salt remains a significant challenge in developing high-performance, chloride-free organic electrolytes for RABs.

Recent research efforts have focused on developing new electrolytes for RABs that could eliminate the highly corrosive  $\text{AlCl}_3$  salt. Here, we review the outcome of several approaches using synthesis Al salts and commercially available  $\text{Al}(\text{OTf})_3$  (summarized in Table 1).

Cationic Al complexes with different ligands and anions were explored by Mandai and Johansson, aiming to achieve active species for Al plating and stripping. Among their tested electrolytes, the low-melting coordination complex of  $[\text{Al}(\text{BIm})_6][\text{TFSI}]_3$  exhibited both cathodic and anodic currents, that they associated with Al plating and stripping, but with poor cycling efficiency due to electrolyte decomposition.<sup>63</sup>

Chiku *et al.*<sup>64</sup> considered aluminum tris(trifluoromethanesulfonyl)imide ( $\text{Al}(\text{TFSI})_3$ ) to utilize the TFSI-containing salt. This research was motivated by the larger size of the  $\text{TFSI}^-$  compared to  $\text{OTf}^-$ . This size difference was hypothesized to lead to weaker electrostatic interactions between the  $\text{TFSI}^-$  and  $\text{Al}^{3+}$  cations. Consequently, this weaker interaction could promote better dissociation of the Al salt in solution, potentially reducing the overpotential required for Al

plating. They achieved Al plating on molybdenum (Mo) in acetonitrile (AN) but required high overpotential for Al metal plating due to the presence of  $\text{Al}_2\text{O}_3$ .<sup>64</sup>

Later on, synthesized aluminum hexafluorophosphate ( $\text{Al}(\text{PF}_6)_3$ ) in dimethyl sulfoxide (DMSO) was investigated by Wen *et al.*<sup>65</sup>.  $\text{Al}^{27}$  NMR studies confirmed  $\text{Al}^{3+}$  cations coordinated by six DMSO molecules. This combination showed Al plating and stripping *via* CV and SEM/EDS confirmed Al plated on Cu. However,  $\text{Al}_2\text{O}_3$  formation occurred during the initial stages due to DMSO decomposition. Additionally, aluminum fluoride ( $\text{AlF}_3$ ) formation was observed near the deposit surface due to trace water in  $\text{Al}(\text{PF}_6)_3$ . Introducing  $\text{Et}_3\text{Al}$  as a water scavenger mitigated this issue, but electrolyte stability remains a challenge.<sup>65</sup>

Apart from the synthesized Al salts, several studies examined commercially available  $\text{Al}(\text{OTf})_3$  in various solvents seeking to achieve Al plating.

In 2014, Jayaprakash *et al.*<sup>68</sup> studied  $\text{Al}(\text{OTf})_3$  in a 1:1 (v/v) mixture of PC and THF. Their CV experiments revealed no electrochemical activity of Al ions, suggesting the unsuitability of this combination for Al plating.<sup>68</sup>

Subsequently,  $\text{Al}(\text{OTf})_3$  was explored in other solvents, such as  $\text{G}_2$ . The FTIR results from the study conducted by Reed and Menke using  $\text{G}_2$  as solvent showed that the presence of OTf exists as either free ions in dilute solutions (0.04 M) or bound to  $\text{Al}(\text{G}_2)_2$  complex at higher concentrations. Despite this, CV did not detect Al plating, possibly due to chelation and electrode passivation by the electrolyte.<sup>69,70</sup>

Mandai and Johansson<sup>26</sup> studied  $\text{Al}(\text{OTf})_3$  in n-methylacetamide (NMA) solution with urea as a room-temperature ternary electrolyte. The optimized composition ( $\text{Al}(\text{OTf})_3/\text{NMA}/\text{urea} = 0.05/0.76/0.19$  in mole fraction) exhibited high ionic conductivity of 2.5 mS/cm at 30 °C. FT-IR and Raman were used to elucidate the dissociation state of  $\text{Al}(\text{OTf})_3$  with varying urea concentrations, revealing the formation of Al complexes like  $[\text{AlOTf-solvent}_x\text{-urea}_2]^{2+}$ .<sup>71</sup> This ternary electrolyte displayed a wider electrochemical stability window of approximately 3.5 V, with redox activity which has been corresponded to the possibility of Al plating and stripping on a Pt substrate.<sup>26</sup> However, further analytical investigation is required to confirm the occurrence of Al plating in this system.

The most recent study on  $\text{Al}(\text{OTf})_3$ , conducted by Slim and Menke<sup>66</sup>, explored Al plating and stripping in THF. This system facilitated Al plating near 0 V *vs.* Al on a gold electrode using

CV, indicating the formation of fully solvated Al complexes ( $\text{Al}(\text{THF})_4^{3+}$ ). However, the absence of a strong Lewis base in the electrolyte hindered Al stripping, resulting in a non-reversible process.<sup>66</sup> The addition of LiCl to  $\text{Al}(\text{OTf})_3/\text{THF}$  demonstrated the enhancing effect of  $\text{Cl}^-$  on Al ion activity. While electrochemical activity increased, Al stripping remained elusive even with a 1:3 ratio of  $\text{Al}(\text{OTf})_3:\text{LiCl}$ .<sup>67</sup> Further investigation of  $\text{Al}(\text{OTf})_3/\text{THF}$  employed  $\text{LiAlH}_4$  as an additive. This study revealed the crucial role of  $\text{H}^-$  in facilitating reversible Al plating and stripping even in the absence of active halides. XPS and SEM confirmed Al plating through the reduction of Al-hydride species on Cu and gold substrates.<sup>72</sup>

The investigation into achieving Al plating and stripping from chloride-free electrolytes suggests that challenges lie beyond achieving effective dissociation of the Al salt within the electrolyte. Even if successful Al plating and stripping occur, side reactions and electrolyte instability can significantly hinder long-term cyclability and efficiency.

Moreover, the critical interplay between electrolyte composition and substrate for successful Al plating and stripping should be highlighted. While some chloride-free electrolytes demonstrate Al plating, these attempts often utilize Cu or W substrates instead of Al. This suggests that the native oxide layer on Al in non-corrosive electrolytes poses a barrier to Al plating and needs further consideration. To address the challenges of Al plating and stripping from non-chloride electrolytes, we must focus on several key questions:

- Which Al salt and electrolyte formulations effectively dissociate the Al salt while minimizing side reactions?
- What types of side reactions are to be expected, and what are their sources? How can these reactions be limited, and what is their impact on Al plating and stripping?
- Can Al metal be utilized as a substrate (negative electrode) in the cell? If not, what alternative options exist?

This work explored Al plating and stripping behavior within a previously proposed  $\text{Al}(\text{OTf})_3/\text{NMA}/\text{urea}$  electrolyte.<sup>26</sup> The study aimed to elucidate the side reactions occurring on a Pt substrate within this electrolyte and their subsequent influence on Al plating. However, further and broader research is crucial to gain a deeper understanding of the electrolyte chemistry to overcome the challenges associated with Al plating and stripping in non-chloride electrolytes.

**Table 1.** The summarized research on Al plating in various electrolytes using the synthesized or commercially available Al salts with combination of different solvents. The green color shows Al plating and/or stripping being confirmed. The orange color means no Al plating and/or stripping was observed and the grey color presents that the study did not explicitly evaluate Al plating and stripping by utilizing characterization techniques such as SEM, and XPS.

Al salt	Additive	Solvent	Al plating	Al stripping	Ref.
AlCl <sub>3</sub>	-	DMSO			49
AlCl <sub>3</sub>	LiCl	DMSO			50
AlCl <sub>3</sub>	-	Dialkylsulfone			51,52
AlCl <sub>3</sub>	-	G <sub>2</sub>			53
AlCl <sub>3</sub>	-	G <sub>3</sub>			53
AlCl <sub>3</sub>	-	G <sub>4</sub>			53
AlCl <sub>3</sub>	-	Acetamide			54
AlCl <sub>3</sub>	-	GBL			55
AlCl <sub>3</sub>	LiH	Diethyl Ether			56
AlCl <sub>3</sub>	LiAlH <sub>4</sub>	THF/Benzene			57
AlCl <sub>3</sub>	LiAlH <sub>4</sub>	THF/Toluene			58
AlCl <sub>3</sub>	LiAlH <sub>4</sub>	THF			59–62
[Al(DMSO) <sub>6</sub> ][OTf] <sub>3</sub>	-	Sulfone			63
[Al(DMSO) <sub>6</sub> ][TFSI] <sub>3</sub>	-	Sulfone			63
[Al(MIm) <sub>6</sub> ][TFSI] <sub>3</sub>	-	Acetonitrile			63
[Al(BIm) <sub>6</sub> ][TFSI] <sub>3</sub>	-	-			63
Al(TFSI) <sub>3</sub>	-	AN			64
Al(PF <sub>6</sub> ) <sub>3</sub>		DMSO			65
Al(OTf) <sub>3</sub>		THF			66
Al(OTf) <sub>3</sub>	LiCl	THF			67
Al(OTf) <sub>3</sub>	-	PC/ THF			68
Al(OTf) <sub>3</sub>	-	G <sub>2</sub>			69,70
Al(OTf) <sub>3</sub>	urea	NMA			26
Al(OTf) <sub>3</sub>	urea	Formamide			71
Al(OTf) <sub>3</sub>	LiAlH <sub>4</sub>	THF			72

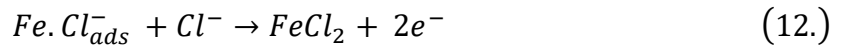


## 2.4 Mitigating corrosion using inhibitors

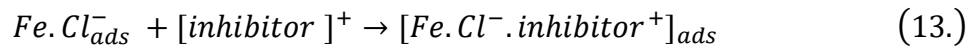
Beyond their role in RABs, ILs are attracting increasing interest as corrosion inhibitors. They have demonstrably reduced corrosion rates for various metals and alloys, including iron, stainless steel (AISI), Cu, Al, and brass, when exposed to aggressive media.<sup>46,113,114</sup> Imidazolium-based IL derivatives, in particular, are effective inhibitors for mild steel in acidic solutions.<sup>43,114–116</sup>

The effectiveness of these ILs is attributed to their heterocyclic structures, the presence of heteroatoms like nitrogen (N), oxygen (O), and sulfur (S), and the presence of multiple bonds. Notably, the  $-C=N-$  group within the imidazole ring acts as a key adsorption site for the IL. This allows the IL molecule to effectively attach to the metal surface, forming a protective layer that can be either physical (a barrier film) or chemical (through a reaction between the IL and the metal).<sup>117–119</sup>

The corrosion process of mild steel in chloride-containing solutions typically involves the following steps: <sup>45,113,117,118</sup>



However, in the presence of inhibitors like imidazolium-based ILs, a protective layer forms *via* the reaction of the cationic part of IL with the metal surface.<sup>120,121</sup>



Cations like pyridinium  $[Py]^+$  and imidazolium  $[EMIm]^+$  interact with negative metal surfaces through electrostatic attraction due to their positive charges. However, they exhibit distinct adsorption behaviors.  $[Py]^+$ , with its localized positive charge, forms a strong initial bond with the negatively charged metal surface immersed in the electrolyte. This leads to slower but ultimately stronger adsorption, providing a stable and long-lasting corrosion inhibition effect. In contrast,  $[EMIm]^+$ , featuring a delocalized positive charge, adsorbs faster due to its multiple potential interaction points with the metal surface. However, this initial advantage may be compromised by a weaker overall bond, potentially leading to a less stable inhibition effect over time<sup>122,123</sup> Moreover, the presence of a longer alkyl chain in the  $Py^+$  cation compared to  $[EMIm]^+$  offers an additional advantage in terms of corrosion inhibition. This extended chain can facilitate the formation of a more compact and protective film at the interface between the

metal and the electrolyte solution. As the alkyl chain length increases, the surface coverage by the adsorbed inhibitor layer also increases. This enhanced surface coverage effectively hinders the interaction between the corrosive species in the electrolyte and the metal surface, leading to corrosion mitigation.<sup>124</sup>

Further studies have explored the role of the anion in ILs in corrosion inhibition.<sup>113,120</sup> For instance, research compared 1-Hexyl-3-methylimidazolium trifluoromethanesulfonate ([HMIM][OTf]) and 1-Hexyl-3-methylimidazolium tetrafluoroborate (HMIM)[BF<sub>4</sub>]) as inhibitors for mild steel in 1 M HCl solution. Interestingly, [HMIM][OTf] demonstrated superior efficacy in reducing the corrosion rate. This difference is attributed to the varying electron-donating abilities of the anions.<sup>105</sup>

Highlighting the importance of anions in ILs, research suggests that 1-Butyl-3-methylimidazolium tetrafluoroborate (BMImBF<sub>4</sub>) functions not only by adsorption but also by fostering the formation of a {Fe[(BMIM)BF<sub>4</sub>]<sub>3</sub>}<sup>2+</sup> complex at imperfections within the native oxide passivating layer, contribute to the self-healing through the inhibitor layer in alkaline environments.<sup>122</sup> Thus, the cations are primarily responsible for initial adsorption on the metal surface.

While corrosion inhibitors offer promise, their effectiveness must be evaluated for reducing the corrosivity of the chloroaluminate ionic liquid. Considerations like:

- How well does the inhibitor prevent corrosion of the current collector in the RABs?
- Does it maintain the desired protective layer over extended periods of battery operation?
- Does it withstand the charge-discharge cycles?

The answers to these questions will be explored in this work.

### 3 Experimental

#### 3.1 Chemicals and Metal foils

All materials used for the preparation of the electrolytes and conducted electrochemical measurements in this study are listed in Table 2.

**Table 2.** The materials used for experiments conducted in this study.

Chemicals	Abbreviation	Purity	Supplier
Aluminum trifluoromethanesulfonate	Al(OTf) <sub>3</sub>	99.9 %	Sigma Aldrich
N-methylacetamide	NMA	99.9 %	Sigma Aldrich
urea	-	99.9 %	Sigma Aldrich
Aluminum chloride	AlCl <sub>3</sub>	99.99 %	Sigma Aldrich
1-Ethyl-3-methylimidazolium chloride	EMImCl	95 %	Sigma Aldrich
1-Butyl-1-methylpyrrolidinium chloride	Py <sub>1.4</sub> Cl	99 %	Sigma Aldrich
1-Ethyl-3-methylimidazolium tetrafluoroborate	EMImBF <sub>4</sub>	95 %	IoLiTec-Ionic Liquids Technologies GmbH
1-Ethyl-3-methylimidazolium trifluoromethanesulfonate	EMImOTf	99 %	IoLiTec-Ionic Liquids Technologies GmbH
Sulfuric acid	H <sub>2</sub> SO <sub>4</sub>	97 %	Sigma Aldrich
Phosphoric acid	H <sub>3</sub> PO <sub>4</sub>	85 %	VWR Chemicals
Nitric acid	HNO <sub>3</sub>	65 %	PanReac AppliChem GmbH
Metal foils	Abbreviation	Thickness Purity	Supplier
Aluminum	Al	0.075 mm, 99.0 %	Goodfellow
Tungsten	W	0.025 mm, 99.96 %	Goodfellow
Platinum	Pt	0.4 mm, 99.9%	rhod Instruments GmbH & Co. KG
Stainless steel 316L	AISI 316L	0.017mm, X2CrNiMo17-12-2	Auerhammer Metallwerk GmbH

## 3.2 Electrolytes preparation

### 3.2.1 Non-corrosive electrolyte based on $\text{Al}(\text{OTf})_3$

$\text{Al}(\text{OTf})_3$ , NMA, and urea underwent vacuum drying at 80 °C for 48 hours in a glass oven (BÜCHI Glass Oven B-585) according to literature guidelines,<sup>26</sup> before electrolyte preparation. The non-corrosive electrolyte based on  $\text{Al}(\text{OTf})_3$  salt was prepared in an argon-filled glovebox (MBraun, <0.1 ppm  $\text{H}_2\text{O}$  and  $\text{O}_2$ ). Initially, NMA was melted at 40 °C, followed by the addition of the appropriate amount of urea and  $\text{Al}(\text{OTf})_3$  to achieve a mole fraction composition of  $\text{Al}(\text{OTf})_3/\text{NMA}/\text{urea}=0.05/0.76/0.19$ . The mixture was stirred using a magnetic bar at room temperature overnight to ensure homogeneity. Following the method outlined in literature,<sup>26</sup> the electrolyte contained over 20000 ppm of water, determined *via* Karl Fisher (KF) titration, and is therefore referred to as ANU-20000 in this study.

To further reduce the water content, an additional drying step was implemented for the ANU-20000 electrolyte. A four-month drying process using calcium chloride ( $\text{CaCl}_2$ ) and Phosphorus pentoxide ( $\text{P}_4\text{O}_{10}$ ) as drying agents was conducted. These agents were not directly dispersed into the electrolyte but stored in the same container inside the argon-filled glovebox to prevent possible contaminations from drying agents. Consequently, the water content decreased to 300 ppm, confirmed by KF titration. The resulting dried electrolyte is referred to as ANU-300.

An urea-free electrolyte was prepared by melting NMA at 40 °C and adding the appropriate amount of  $\text{Al}(\text{OTf})_3$  to achieve a 0.05 mole fraction of  $\text{Al}(\text{OTf})_3$  in NMA. Subsequently, the electrolyte was stirred overnight inside the argon-filled glovebox.

### 3.2.2 Chloroaluminate ionic liquid electrolytes

The electrolyte was prepared within an argon-filled glovebox (MBraun, <0.1 ppm  $\text{H}_2\text{O}$  and  $\text{O}_2$ ) by slowly mixing  $\text{AlCl}_3$  and EMImCl with the appropriate amounts to achieve a molar ratio of 1.5:1 of  $\text{AlCl}_3$ : EMImCl and then was stirred overnight. This electrolyte is labeled as A15E1 in this study.

Given the exothermic nature of the reaction between  $\text{AlCl}_3$  and EMImCl, the mixing process was conducted gradually, with careful attention to prevent excessive temperature elevation and potential thermal decomposition of EMImCl. The mixture was stirred overnight to ensure complete dissolution and obtain a clear solution.

The electrolytes containing inhibitors were prepared by adding 2 wt% of the inhibitors (EMImOTf, EMIBF<sub>4</sub>, and Py<sub>1.4</sub>Cl) to the prepared A15E1 electrolyte and were stirred overnight using a magnetic stirrer. The final electrolytes are labeled as mentioned in Table 3.

**Table 3.** The lists of the labels assigned to various electrolytes containing inhibitors, along with their concentrations.

Electrolyte	Inhibitor	Labeling
AlCl <sub>3</sub> : EMImCl (molar ratio 1.5:1)	2 w% EMImBF <sub>4</sub>	A15E1BF2
AlCl <sub>3</sub> : EMImCl (molar ratio 1.5:1)	2 w% EMImOTf	A15E1OTf2
AlCl <sub>3</sub> : EMImCl (molar ratio 1.5:1)	2 w% Py <sub>1.4</sub> Cl	A15E1Py2

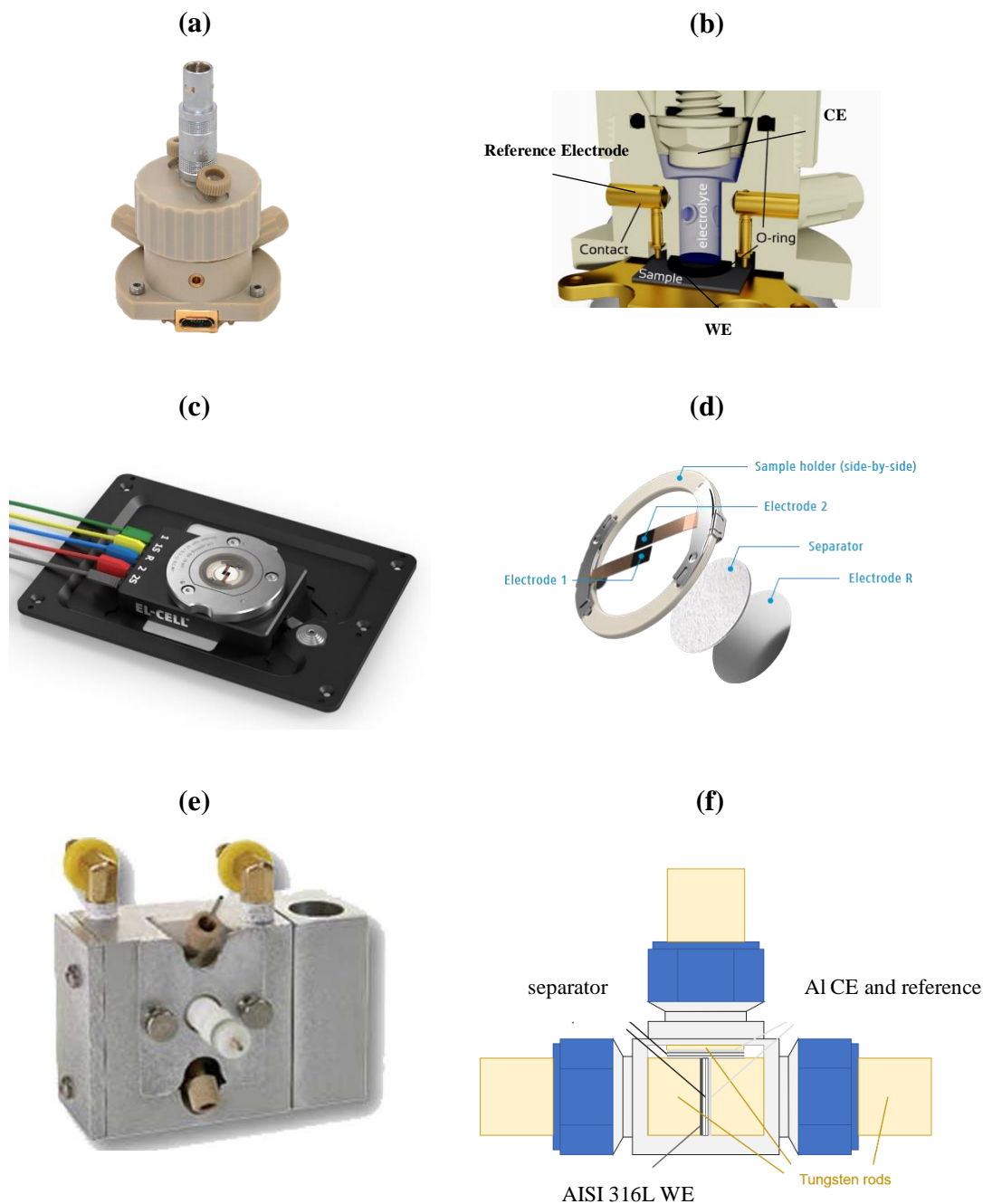
### 3.3 Electrochemical analysis

#### 3.3.1 Cells preparation

The airtight TSC surface (from rhd Instruments GmbH & Co. KG company, Germany),<sup>125</sup> served as a three-electrode system for electrochemical measurements. The TSC Surface cell, provides a sealed PEEK housing, as an electrolyte reservoir, making it suitable for air- and moisture-sensitive samples as well as corrosive electrolytes. The cell was assembled within an argon-filled glovebox with the working electrode (WE) consisting of metal foils (the surface area of 0.28 cm<sup>2</sup>) and the counter electrode (CE) which could be either a glassy carbon (GC) disc or an Al disc, depending on the specific experiment. An Al wire was utilized as the pseudo-reference electrode. Each experiment employed 800  $\mu$ L of electrolyte. The Al wire, used as a quasi-reference, was immersed in two acidic solutions of H<sub>2</sub>SO<sub>4</sub>:HNO<sub>3</sub>: H<sub>3</sub>PO<sub>4</sub> (in a 25: 5: 70 volume ratio) and HNO<sub>3</sub>:H<sub>3</sub>PO<sub>4</sub> (in a 5:95 volume ratio) before any measurements to remove the oxide layer to some extent. Then rinsed with acetone and immediately transferred to the glovebox. The GC electrode was mechanically polished with 250 nm diamond polishing paste and rinsed with deionized water before any measurements.

One advantage of the special design of this cell is that the separator is eliminated. This feature proves invaluable for preparing samples for post-mortem analysis such as SEM and XPS, as it reduces the interference caused by the glass fiber separator during observation. The cell is

shown in Figure 3 (a) and (b). Additionally, the TSC Surface cell was equipped with a self-made gas-tight connection from rhd Instruments, allowing for gas collection for Gas Chromatography (GC) measurements.



**Figure 3.** (a) TSC surface cell (b) the vertical section of the TSC Surface cell <sup>125</sup> (c) EL-CELL ECC-Opto-10 test cell mounted on a standard microscope sample stage (d) EL-CELL ECC-Opto-10 sample holder (side-by-side) <sup>162</sup> (e) EQCM Quartz Crystal Microbalance Gamry Instruments <sup>126</sup> (f) Electrodes arrangement in the Swagelok cell

Optical microscopy observation was performed by an airtight optical cell, known as ECC-Opto-10 (EL-CELL, Germany), equipped with a window seal. The cell is presented in Figures 3 (c) and (d). This cell employed a three-electrode setup, featuring a face-to-face arrangement of WE and CE, along with pseudo-reference electrodes positioned as discs beneath the other electrode, separated by a separator. Each measurement utilized 10  $\mu$ l of electrolyte within this cell.

The air-protected QCM Flow Cell Kit, manufactured by Gamry Instruments, was used for EQCM (Electrochemical Quartz Crystal Microbalance) measurements (shown in Figure 3 (e)<sup>126</sup>). The microbalance was configured with a 5 MHz quartz crystal coated with a thin Pt film, covering a working area of 1.1 cm<sup>2</sup>. To ensure an inert environment, the cell assembly took place within an argon-filled glovebox (<0.1 ppm H<sub>2</sub>O and O<sub>2</sub>), utilizing a Pt-coated quartz crystal as WE, an Al wire as CE, and an Al wire as the quasi-reference. Prior to any measurement, the Pt-coated quartz crystal was calibrated in a 5 mM solution of copper (II) sulfate (CuSO<sub>4</sub>) in 1 M H<sub>2</sub>SO<sub>4</sub>.

The Swagelok cell, depicted in Figure 3 (f), has a body made of PEEK, which was utilized for electrochemical measurements. The PEEK material is stable in the acidic chloroaluminate ionic liquid electrolytes. A 12 mm diameter tungsten (W) bar was also used in this cell as a current collector, chosen for its resistance to the corrosivity of the AlCl<sub>3</sub>:EMImCl (1.5:1) electrolyte used in this study. Glass microfiber separators (GF/A from Whatman) were placed between the electrodes.

In the experiments conducted with the Swagelok cell, an AISI 316L foil was used as WE, with two Al foils serving as CE and pseudo-reference electrodes. A total of 600 microliters of electrolyte were used in this cell. The cells were assembled in an argon-filled glovebox (MBraun, <0.1 ppm H<sub>2</sub>O and O<sub>2</sub>).

### **3.3.2 Electrochemical characterization**

Electrochemical measurements, as described below, were carried out in a climate chamber at 25 °C mostly using a VMP3 multi-channel potentiostat/galvanostat (Bio-logic Science Instrument, France), equipped with the EC-Lab® software. If another potentiostat/galvanostat has been used, it would be mentioned directly in the experimental details.

### 3.3.2.1 Cyclic voltammetry measurements (CV)

The CV measurements were conducted in chapters 4.1 and 4.2 using a scan rate of 20 mVs<sup>-1</sup> within the potential range of -1 V to 1.2 V vs. Al. The setup included a Pt WE, an Al disc, and an Al wire as the CE and the pseudo-reference electrode, respectively. We employed two electrolytes ANU-20000 and ANU-300 based on the specific measurement.

The CV measurement described in Section 4.1 was conducted in an *operando* optical microscopy cell using a potentiostat/galvanostat (SP200, Biologic Science Instrument GmbH, France) equipped with EC-Lab software. The applied potentials ranged from -1 V to 1.2 V vs. Al, with a scan rate of 20 mVs<sup>-1</sup>.

CV measurement, section 4.1 and 4.2, was performed using with an EQCM 10M combined with the Interface™ 1010 B Potentiostat/Galvanostat/ZRA (Gamry Instruments Inc, USA). The electrochemical test program includes several steps: 5 activation cycles in the potential region -0.6/1.2 V vs. Al, followed by 55 further cycles in the potential region -1.0/1.2 V vs. Al with a scan rate of 20 mV/s. However, as the Al pseudo-reference experiences slight shifts during cycling,<sup>127</sup> the potential window was adjusted to maintain overpotential throughout the cycles

In chapter 5.2.1, CV measurements were performed with a scan rate of 10 mVs<sup>-1</sup> in the potential range of -0.5 V to 1 V vs. Al. The setup included an Al foil as WE, a GC disc as CE, and an Al wire as the pseudo-reference electrode. Different electrolytes—A15E1, A15E1Py2, A15E1OTf2, and A15E1BF2— were used for this series of measurements. The CV was repeated for 50 cycles. The Al foils were prepared for X-ray Photoelectron Spectroscopy (XPS) measurements.

### 3.3.2.2 Chronoamperometry measurements (CA)

CA was also performed in chapter 4.1 by polarizing the Pt WE at -1 V vs. Al for 2 hours. The sample polarized in ANU-20000 was prepared for Thermal Field Emission Scanning Electron Microscope (FE-SEM) measurements and the sample polarized in ANU-300 was prepared for XPS measurements.

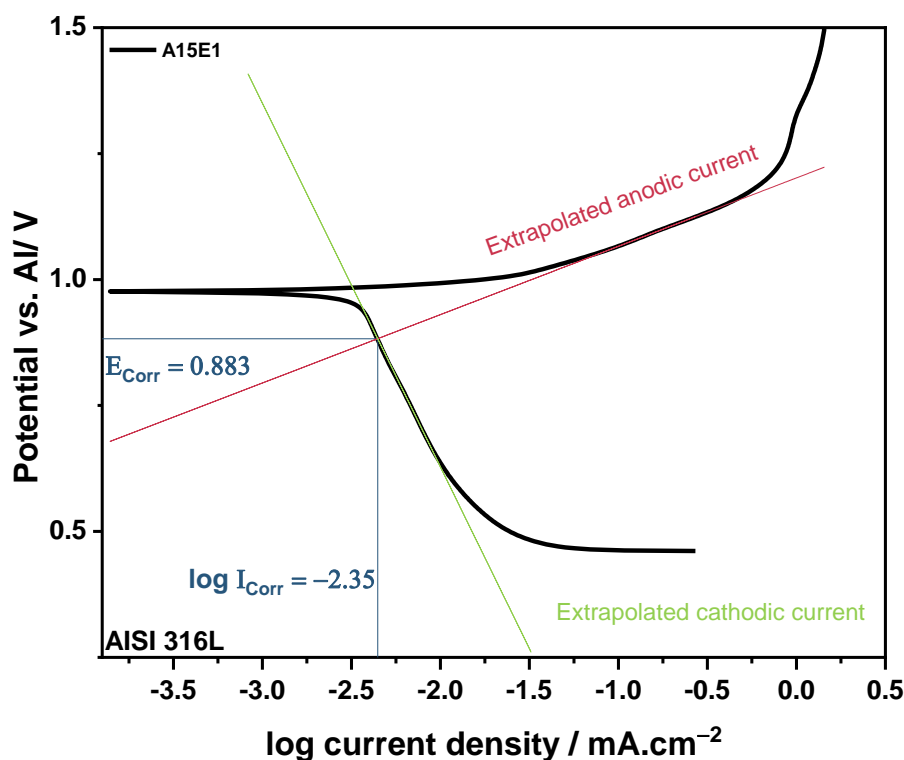
CA was also performed in the chapter 5.1.2.2 and 5.1.1 by polarizing the AISI 316L and W WE at 1.5 V vs. Al for 1 minute and 5 minutes, respectively in A15E1, A15E1Py2, A15E1OTf2, and A15E1BF2 electrolytes. These AISI 316L samples were then prepared for XPS measurements.



### 3.3.2.3 Potentiodynamic polarization measurements

Potentiodynamic polarization experiments were utilized to measure the corrosion current densities of AISI 316L in the  $\text{AlCl}_3\text{:EMImCl}$  (1.5:1) electrolyte, as well as to evaluate the impact of inhibitors introduced into the electrolyte. This evaluation was achieved by comparing the corrosion current densities. The potentiodynamic polarization was also performed for the W WE in the same condition as AISI 316L in the A15E1 electrolyte.

In the potentiodynamic polarization experiments, the potential was swept at a scan rate of 1 mV/s, starting from 0.5 V below the open-circuit potential (OCV) and extending to 3 V vs. Al. The current was measured and presented in a logarithmic form to determine corrosion potentials ( $E_{\text{corr}}$ ) and corrosion current densities ( $I_{\text{corr}}$ ) using Tafel slope extrapolation. This method is commonly used in electrochemical investigations to determine  $E_{\text{corr}}$  and  $I_{\text{corr}}$ .<sup>128</sup>



**Figure 4.** The Tafel extrapolation defines the corrosion current density ( $I_{\text{corr}}$ ) and corrosion potential ( $E_{\text{corr}}$ ) of AISI 316L in the A15E1 electrolyte. The intersection of the extrapolated anodic and cathodic branches determines these values.

In the Tafel extrapolation method, linear regions of both the oxidation and reduction branches, which follow linearity for at least a decade in the vicinity of OCV, are extrapolated. The intersection of the extrapolated anodic and cathodic currents defines the  $E_{\text{corr}}$  and  $I_{\text{corr}}$ . This

process is demonstrated in Figure 4 as an example for AISI 316L in the A15E1 electrolyte. The  $E_{\text{corr}}$  and  $I_{\text{corr}}$  determined by this method can indicate the corrosivity of the electrolytes on AISI 316L when it is immersed in the electrolyte without the application of any potential.

Inhibition efficiencies (IE) of the inhibitors were computed from  $I_{\text{corr}}$  using the following equation:<sup>128</sup>

$$IE\% = \left[ \frac{I_{\text{corr}} - I_{\text{corr}}^0}{I_{\text{corr}}^0} \right] \times 100 \quad (14.)$$

where  $I_{\text{corr}}^0$  represents the corrosion current density in the electrolyte without inhibitors and  $I_{\text{corr}}$  denotes the corrosion current density in the electrolyte with inhibitors.

In the experimental methodology of this study, we employed the upper-lower bound method to estimate the standard error of IE. This method, chosen for its simplicity and robustness, provides an estimation of uncertainty by considering extreme values of  $I_{\text{corr}}^0$  and  $I_{\text{corr}}$ , essentially presenting the best and worst-case scenarios. By calculating the maximum variation possible in IE, we gained insights into the range of possible outcomes.

To illustrate the application of this method, the IE of EMImBF<sub>4</sub> inhibitor was considered along with its standard error calculated using the upper-lower bound method.

First, we determined the nominal IE based on the average current densities of  $I_{\text{corr}}^0$  and  $I_{\text{corr}}$ :

$$IE_{\text{nominal}}\% = \left[ \frac{4.4 - 3.1}{4.4} \right] \times 100 \approx 30 \quad (15.)$$

Next, we determined the range of IE values by selecting the maximum and minimum possible values. In our case, the maximum IE was 49% and the minimum IE was 9%, thus the range of IE was approximately 40%.

$$IE_{\text{upper } I_{\text{corr}}^0, \text{ lower } I_{\text{corr}}}\% = \left[ \frac{4.5 - 2.3}{4.5} \right] \times 100 \approx 49 \quad (16.)$$

$$IE_{\text{lower } I_{\text{corr}}^0, \text{ upper } I_{\text{corr}}}\% = \left[ \frac{4.3 - 3.9}{4.3} \right] \times 100 \approx 9 \quad (17.)$$

Finally, the standard error was calculated as half of this IE range, resulting in 20%. This means that the IE for the A15E1BF2 electrolyte is around 30% with an error of 20%.

The current density for AISI 316L at each potential can also be read directly from the polarization curve obtained using the potentiodynamic polarization tests.

### 3.4 Materials characterization techniques

### **3.4.1 Scanning electron microscopy and energy-dispersive X-ray spectroscopy (SEM/EDX)**

Surface morphology analysis was conducted by a thermal field emission scanning electron microscope (FE-SEM, Carl Zeiss SMT AG) at an acceleration voltage of 5.00 kV. The FE-SEM device is equipped with an energy-dispersive X-ray spectroscope (EDX, Quantax 400 SDD, Bruker). The sample was fixed on a steel sample holder using sticky carbon tape.

SEM and EDS analyses were performed on the Pt sample polarized at -1 V *vs.* Al for 2 hours in the ANU-2000 electrode (using CA technique). After the measurement, the cell was disassembled in an Ar-filled glovebox. The Pt foil was washed with pure anhydrous methanol (MeOH) and dried for 30 minutes at room temperature under vacuum immediately after the measurement. The sample was affixed to a steel sample holder using sticky carbon tape for FE-SEM measurements. The samples were constantly kept in an inert gas atmosphere at all times.

### **3.4.2 Optical microscopy**

During the CV measurement on the Pt WE in ANU-2000 electrolyte, optical microscopy images were taken to observe any optical or morphological changes during the potential changes. The images of the Pt electrode were captured at different potentials: -0.5 V *vs.* Al, -1 V *vs.* Al, 0 V *vs.* Al, and 1 V *vs.* Al using a LEICA M205C microscope (Germany) at 2.5x magnification. The images were processed using GIMP software version 2.10.32.

### **3.4.3 X-ray photoelectron spectroscopy (XPS)**

XPS measurements were conducted using a K-Alpha XPS spectrometer from ThermoFisher Scientific (UK). The instrument utilized a monochromated Al K $\alpha$  X-ray source with a spot size of 400  $\mu$ m. Photoelectrons were detected using a hemispherical 180 dual-focus analyzer equipped with 128 channel detectors. The sample preparation involved placing the samples on a holder using clips within an Ar-filled glovebox, which remained connected to the spectrometer. Throughout the process, an inert gas atmosphere was maintained to prevent unwanted reactions.

XPS analysis was performed on three different types of samples: Pt (chapter 4.3), AISI 316L (chapter 5.1), and Al (chapter 5.2).

In ex-situ XPS Analysis (chapter 4.3), the Pt sample was analyzed after being polarized at -1 V vs. Al for 2 hours using the CA technique in ANU-300 electrolyte. After the measurement, the cell was disassembled in an Ar-filled glovebox. The Pt foil was thoroughly washed with pure anhydrous MeOH and vacuum-dried for 30 minutes at room temperature. XPS measurements were also performed on an Al foil, which served as a pristine sample without any additional treatment.

In chapters 5.1 and 5.2, XPS measurements were performed on two series of AISI 316L samples:

- The samples immersed in the A15E1, A15E1Py2, A15E1OTf2, and A15E1BF2 electrolytes for 10 minutes.
- AISI 316L samples polarized at 1.5 V vs. Al for 1 minute using the CA technique in the same electrolytes.

After each treatment (immersion or polarization), all samples were washed with 1,2-difluorobenzene solvent and vacuum-dried at room temperature. XPS measurements were also, performed on as received Al foil for reference.

Additionally, XPS analysis was conducted on two series of Al samples:

- Al samples immersed for 10 minutes in A15E1, A15E1Py2, A15E1OTf2, and A15E1BF2 electrolytes.
- Al samples cycled 50 times by CV measurement in the same electrolytes.

Similar to the AISI 316L samples, all Al samples were washed with 1,2-difluorobenzene and vacuum-dried after treatment.

Data acquisition and processing were carried out using the Thermo Advantage software (Version 5.9931, Thermo Scientific). The spectra were fitted with one or more Voigt profiles (binding energy uncertainty:  $\pm 0.15$  eV). All spectra were referenced to the hydrocarbon C 1s peak (C–C, C–H) at 285.0 eV. For clear presentation and comparability, the intensity was normalized by setting the maximum peak height to 1.

### **3.5 Analytical techniques**

### 3.5.1 Electrochemical quartz crystal microbalance (EQCM)

EQCM is a highly sensitive technique that measures the change in mass on a piezoelectric quartz crystal electrode. As mass accumulates or departs from the electrode surface, the crystal's oscillating frequency changes. This frequency shift can be correlated to the mass change using the Sauerbrey method.<sup>129</sup>

The mass change at the Pt WE was monitored during CV measurement in ANU-2000 and Al(OTf)<sub>3</sub>/NMA electrolytes. The EQCM results were modeled using the Sauerbrey method.<sup>129</sup> In this method, the change in frequency ( $\Delta f$ ) of oscillating quartz during the experiment can be related to the experimental mass change ( $m_{exp}$ ) as described in equation (13.):

$$\Delta m_{exp} = \frac{-\Delta f * A}{C_f} \quad (18.)$$

where  $C_f$  is the sensitivity factor for the crystal used (i.e. 56.6 Hz  $\mu\text{g}^{-1} \text{cm}^2$  for a 5MHz quartz crystal at room temperature, which is checked by standard calibration procedure with a solution of CuSO<sub>4</sub> (5 mM) in 1 M H<sub>2</sub>SO<sub>4</sub> and the electroactive crystal area  $A$  was 1.1 cm<sup>2</sup>.

The theoretical mass change ( $m_{th}$ ), on the other hand, can also be calculated through equation 19.

$$\Delta m_{th} = \frac{Q * M}{z * F} \quad (19.)$$

where  $Q$  is the charge passed through the electrode in Coulomb (C),  $M$  is the molecular weight of adsorbed ions,  $F$  is the Faraday constant (96 485 C/mol), and  $z$  is the valence number of the ion.

The main principle of WE mass changing calculation is the assumption that the calculated theoretical mass should be equal to the measured experimental mass. Practically obtained differences between these values can be compensated by appropriate values of  $M$  of adsorbed species, which can also include solvate shells. In this study, various species were calculated to identify the closest value to the measured experimental mass. The values of molecular mass and the valence number of the ion for Al are 26.982 and 3, while for Al(OH)<sup>+2</sup>, the corresponding values are 176.044 and 2, respectively.

It is well known<sup>130</sup> that not only an additional mass induces a frequency shift of a quartz resonator, but also immersion of the quartz crystal in a very viscous liquid or changes in the viscoelastic properties of the liquids adjacent to the quartz, induces changes of its resonant

frequency. This can be mistaken as a mass change. In the present work, the viscosity of ANU electrolyte is 33.4 mPa\*s<sup>127</sup> (viscosity of AlCl<sub>3</sub>:EMImCl with a molar ratio of 1.5:1 is 14.82 mPa\*s).<sup>131</sup> In such cases, the resonance frequency shift is more significant than the damping shift, allowing us to use the Sauerbrey method.<sup>130</sup>

The influence of the gas formation on Sauerbrey equation validity was also estimated using the quality factor ( $Q_E$ ), which fluctuated within the range of  $3 \times 10^3$  to  $6 \times 10^3$ . The  $Q_E$  is commonly defined as the ratio of the energy stored in the oscillation to the dissipated energy. It typically falls within the range of  $10^3$  to  $10^6$ , when the surrounding environment does not dampen the oscillation.  $Q_E$  has been calculated with the Gamry software “Gamry Echem Analyst.”

### **3.5.2 Gas chromatography (GC)**

GC was performed using a Clarus 690 GC (Perkin Elmer, USA) coupled to an ARNEL 4019 system (Perkin Elmer, USA) and mass spectroscopy (MS, SQ8S, Perkin Elmer, USA). The collected gas sample was introduced with a syringe into a loop system (Vici Valco) that was connected to various separation columns and injectors, namely a thermal conductivity detector (TCD) and a double TCD. The setup allowed the detection of the gases H<sub>2</sub>, CO<sub>2</sub>, CO, CH<sub>4</sub>, C<sub>2</sub>H<sub>2</sub>, C<sub>2</sub>H<sub>4</sub>, C<sub>2</sub>H<sub>6</sub>, O<sub>2</sub>, He, N<sub>2</sub>, and Ar starting at a concentration of about 100 ppm. The gas samples were injected at room temperature and switched to the columns at normal pressure after the samples were depressurized. Evaluations were performed using TotalChrom 6.3.4 software (Perkin Elmer, USA) and Origin (OriginLab 2021). To increase the comparability between chromatograms, the intensities of TCD responses were normalized to the peak area of Ar derived from the glovebox atmosphere.

### **3.5.3 Karl Fisher (KF) Titration**

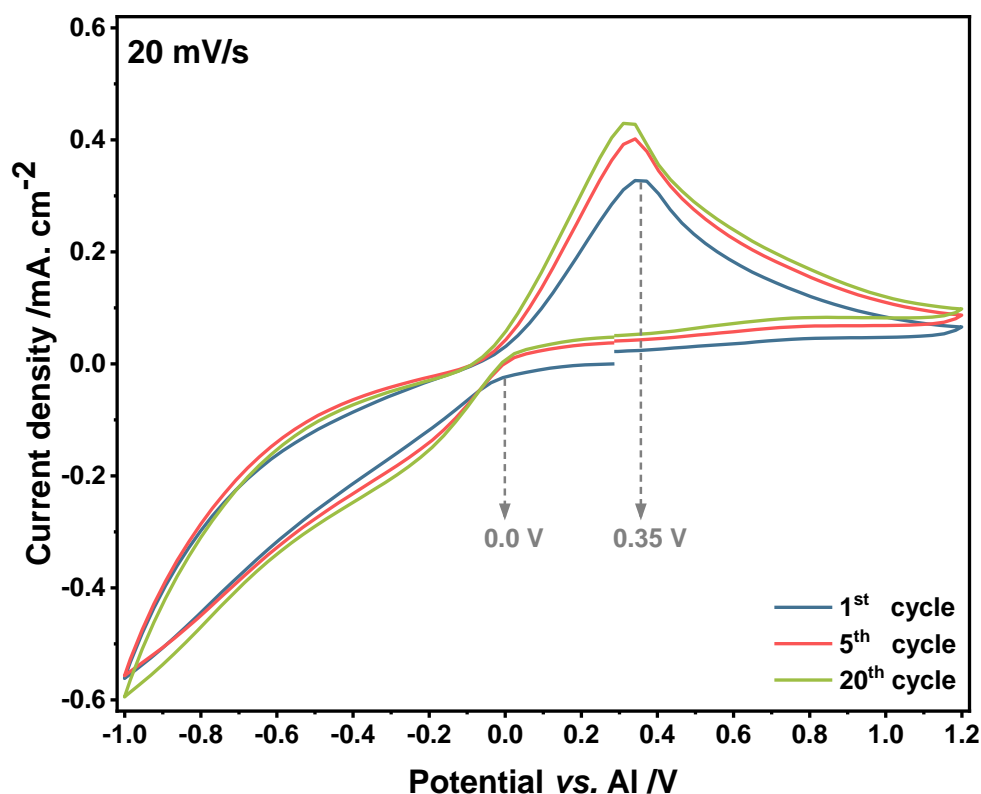
KF titration was performed using SI Analytics Automatic titrator TitroLine® 7500 KF Trace for coulometric water determination. The KF titrator setup was calibrated with a 0.1% water standard (Honeywell International Inc., HYDRANAL Standard). The electrolyte samples of ANU-2000 and ANU-300 were introduced into the KF titration cell using a syringe.

## 4 Assessing the feasibility of Al plating/stripping from a non-corrosive $\text{Al}(\text{OTf})_3$ -based electrolyte

The development of suitable electrolytes for RABs is a significant challenge that limits their market potential. In the last years, a non-corrosive ternary electrolyte has been proposed composed of aluminum trifluoromethanesulfonate ( $\text{Al}(\text{OTf})_3$ ), *N*-methylacetamide (NMA), and urea in molar fractions of 0.05/0.76/0.19.<sup>26</sup> Among various molar ratios of components in this ternary electrolyte, this composition has demonstrated optimal physicochemical properties, including high ionic conductivity (2.5 mS/cm at 30 °C).<sup>26</sup> This electrolyte has been suggested as an alternative to chloroaluminate ionic liquid electrolytes for RABs, potentially enabling Al plating and stripping. In this chapter, we aim to explore the Al plating and stripping capabilities of this electrolyte, addressing an aspect that has been overlooked in earlier studies.

### 4.1 Investigation on Al plating/stripping from ANU-20000 Electrolyte

CV was used to investigate the possibility of Al plating from the ANU-20000 electrolyte and the voltammograms of Pt electrode in the ANU-20000 electrolyte are presented in Figure 5. The voltammograms reveal an oxidation peak at 0.35 V *vs.* Al and a reductive process that starts at around 0 V *vs.* Al. Additionally, the same redox behavior can be observed within the cycles, showing the reproducibility of consecutive cycles. These reductive/oxidative currents were previously assigned to the Al plating and stripping along with possible electrolyte decomposition.<sup>26</sup>

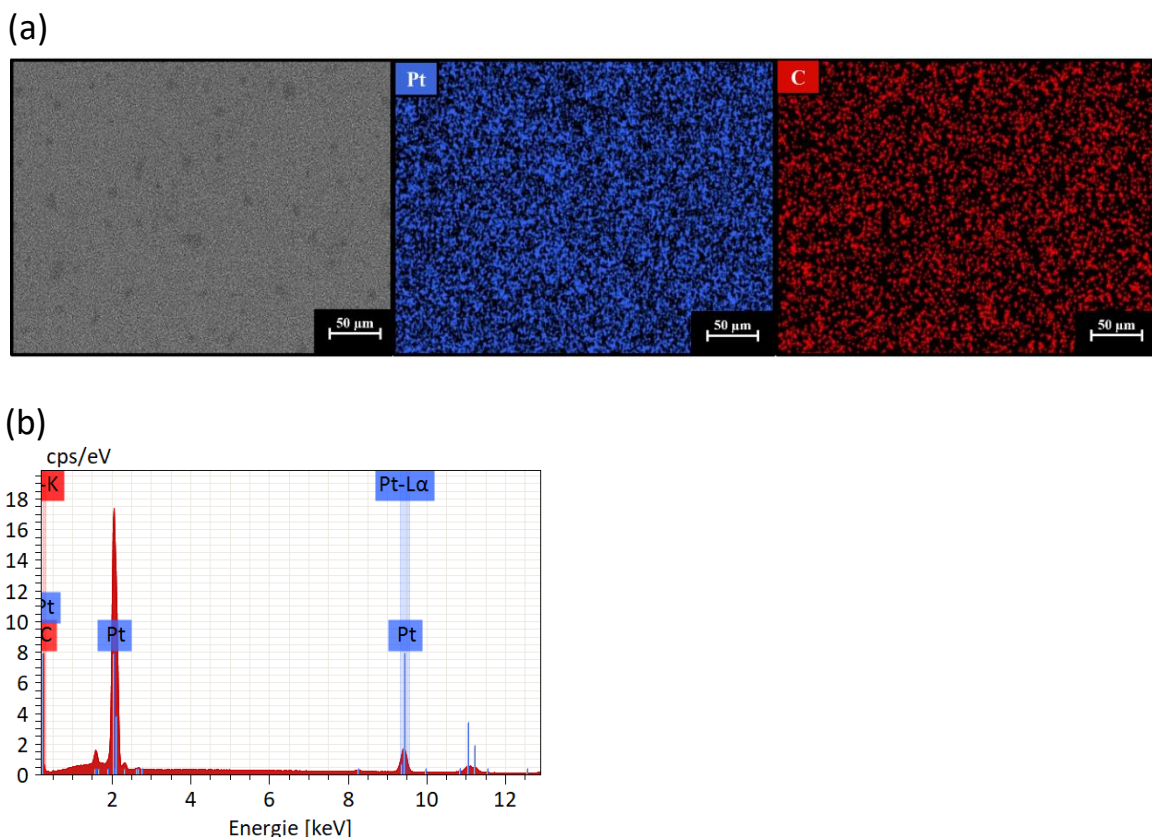


**Figure 5.** CV curves on the Pt WE in ANU-2000 electrolyte at a scan rate of  $20 \text{ mVs}^{-1}$ . Al were used as reference electrode and counter electrode.

To corroborate that the reduction current is due to Al plating, the Pt was polarized and then investigated using FE-SEM/EDX. The potential was chosen based on the work of Mandai and Johansson<sup>15</sup> which has mentioned that the reduction process, starting at ca.  $-0.7 \text{ V vs. Al}$ , is supposed to be Al plating with a possible simultaneous decomposition of urea and NMA as bubbles formed on the Pt WE at ca.  $-1.2 \text{ V vs. Al}$ .<sup>15</sup> To avoid side reactions at lower potentials, the potential of  $-1 \text{ V vs. Al}$  was chosen.

In the experiments conducted with other electrolytes reported so far, such as  $\text{AlCl}_3\text{:EMImCl}$  at the molar ratio of 2:1 and  $\text{Al(OTf)}_3\text{:LiAlH}_4$  at a 3:1 molar ratio in THF, the plated Al was detectable by FE-SEM and EDX.<sup>72,132</sup> However, no plated Al can be detected on the Pt electrode surface with this non-corrosive electrolyte of ANU-20000 as shown in Figure 6 (a) and (b) showing FE-SEM and EDX, respectively.

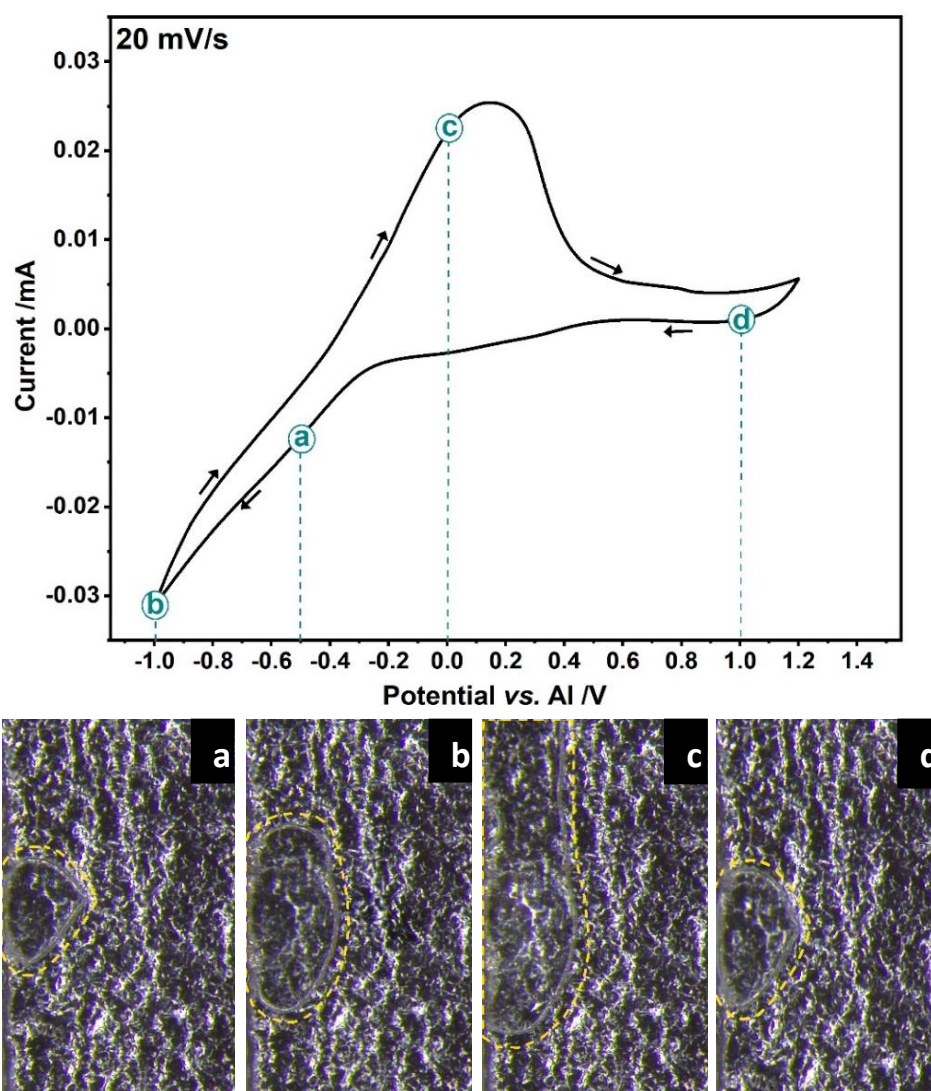




**Figure 6.** (a) Field emission-scanning electron microscopy (FE-SEM) and (b) energy-dispersive X-ray spectroscopy (EDX) images of the Pt WE polarized at -1 V *vs.* Al for 2 hours in ANU-20000 electrolyte.

The *operando* optical microscopy imaging of the Pt electrode was conducted to explore any optical/morphological change correlated to changes in potential. Figure 7 shows the images of the Pt electrode taken at different potentials while measuring CV. It can be seen in Figure 7 from points (a) to (d) that the formed gas bubbles (highlighted with a yellow-dashed circle) are reversibly growing and shrinking during the CV cycle. The reaction, which leads to the formation of gas (points (a) to (c)) can be attributed to the hydrogen generated through the onset of hydrogen evolution (HER). The standard reduction potentials ( $E^\circ$ ) for HER is approximately 0 V *vs.* the standard hydrogen electrode (SHE), whereas the Al reduction ( $Al^{+3} + e^- \rightleftharpoons Al$ ) would be -1.66 V *vs.* SHE.<sup>133</sup> This implies that even under non-standard conditions (not at 25 °C, 1 atm) and in non-aqueous electrolytes, the HER reaction can occur before Al reduction. The HER would point towards a considerable amount of water in the electrolyte. Indeed, despite strictly following the literature's guidelines,<sup>26</sup> including vacuum drying of all electrolyte components at 80 °C, over 20,000 ppm of water remained, as measured using the KF titration technique. This results in the formation of “stable gas pockets”,<sup>37</sup> which

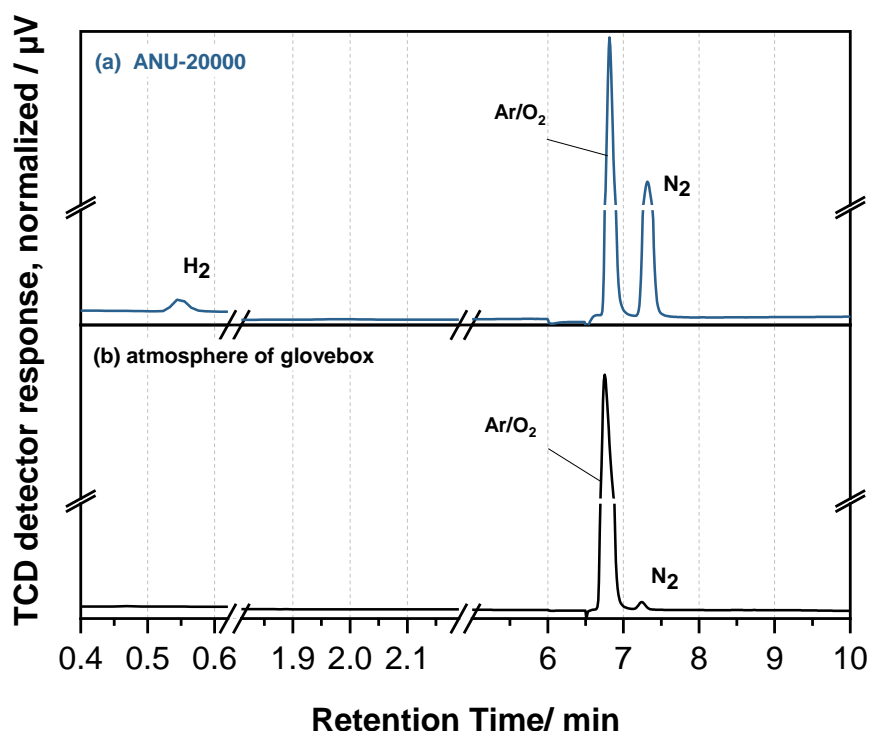
may hinder the plating process of Al on Pt. Similar findings were also previously observed in the case of  $\text{Cr}^{38}$  and  $\text{Ni}^{39}$  plating.



**Figure 7.** The Optical microscopy images of the Pt electrode were captured during CV measurement in the potential window of -1 V to 1.2 V vs. Al at a scan rate of  $20 \text{ mVs}^{-1}$  in the ANU-20000 electrolyte. (a) -0.5 V vs. Al (b) -1 V vs. Al (c) 0 V vs. Al (d) 1 V vs. Al.

GC analysis was performed to analyze the gases that are formed during polarization at Pt electrode. For this purpose, the Pt electrode was polarized in the ANU-20000 electrolyte, which was dried in the same way reported in the literature<sup>26</sup>, and the resulting gas was collected and transferred into a GC. Figure 8 (a) shows the chromatogram of the analyzed gas. The peak consisting of Ar and  $\text{O}_2$ , which could not be separated in the case of the chromatogram shown here, was separated in a second separation line, which considers only the Ar/ $\text{O}_2$  separation. This shows that no oxygen was present, confirming the tightness of the cell and the appropriate gas transfer process (the cells were prepared under Ar inside the glovebox). The GC analysis

reveals that the formed gas during the polarization of the Pt electrode is mainly nitrogen gas ( $N_2$ ) and hydrogen gas ( $H_2$ ). No  $H_2$  can be observed in the “blank” chromatogram of the atmosphere of the glovebox, Figure 8 (b). Moreover, the  $N_2$  peak in Figure 8 (a) is significantly more pronounced than the one obtained in the blank. Therefore, based on these measurements it can be concluded that  $N_2$  and  $H_2$  gases are formed during the polarization of Pt in the ANU-20000 electrolyte.



**Figure 8.** (a) GC spectrum of the collected gas after polarization of the Pt WE at -1 V vs. Al for 30 min in the ANU-20000 electrolyte (contains <20000 ppm of water) (b) GC spectrum of the collected gas from the atmosphere of the glovebox. The intensities of TCD responses are normalized with respect to the peak area of Ar from the glovebox atmosphere.

The mechanism of the redox reaction may be supplemented by the EQCM technique. This technique would help us to model the electrochemical reactions on the interface of Pt and the electrolyte through the mass changes of the Pt electrode. Figure 9 shows the electrode mass change vs. charge passed (a) cycle 6<sup>th</sup> and (b) cycle 60<sup>th</sup> and potential vs. charge passed (c) cycle 6<sup>th</sup> and (d) cycle 60<sup>th</sup> obtained from the EQCM measurement during the CV. A comparison is made between the 6<sup>th</sup> cycle and the 60<sup>th</sup> cycle to observe long-term cycling effects.

During the reduction process, HER can occur (previously confirmed by GC analysis), which is facilitated by hydrogen-bonded water molecules on the Pt surface in the ANU-20000 electrolyte.

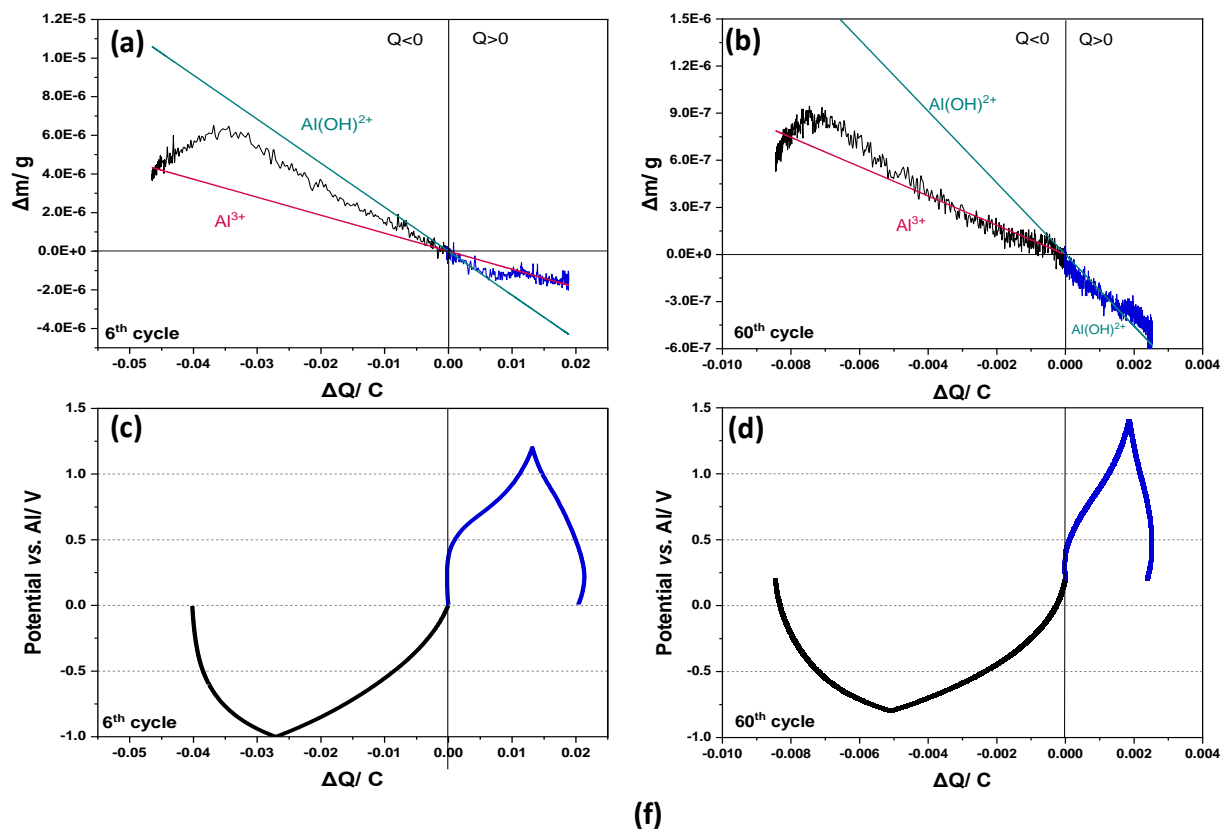
As it is reported, under open circuit voltage (OCV) conditions in an acidic solution, a distinctive arrangement of hydrogen-bonded water molecules attached to the adsorbed hydroxyl groups on the Pt surface can be expected.<sup>134</sup> The initial step of HER (known as Volmer step, equation 20) involves the adsorption of hydrogen ( $H^*$ ) onto the electrode surface. This process combines an electron transferred from a conductive substrate with a proton from the solution. However, in an alkaline solution, an additional prerequisite step of water dissociation is necessary before this reaction can occur, which may reduce the reaction rate.<sup>135,136</sup>

For the subsequent step, two possible reaction pathways have been generally accepted. This first pathway is the Heyrovsky reaction (equation 21), where the adsorbed hydrogen atom combines with an electron and proton to form a hydrogen molecule, and the second pathway is the Tafel reaction (equation 22), wherein two adjacent adsorbed hydrogen atoms combine to form a single  $H_2$  molecule.<sup>43</sup> Free energies calculated by Density Functional Theory (DFT) highlight the prevalence of the Volmer-Tafel route as the dominant mechanism over a wide range of pH.<sup>43</sup>



The HER mechanism model was combined with the model for reducing Al ions on the Pt surface, by incorporating EQCM measurements. Additionally, desorption of the hydroxyl groups can happen from the surface-active sites (\*) together with a reduction of  $OH^*$  to the  $OH^-$ . The formed  $Al^{3+}$  cations after dissociation of the solvated complex  $[AlOTf-solvent_x-urea_2]^{2+}$  near the Pt surface react with the  $OH^-$  anions. The formation of  $Al(OH)^{2+}$  complex ion on the Pt surface can play an important role in suppressing the Al plating from the proposed electrolyte.<sup>137</sup> Notably, the experimental mass change of the adsorbed species on the Pt surface during the reduction process at the 6<sup>th</sup> cycle is close to the molecular weight of the proposed formula of  $Al(OH)^{2+}$  ions rather than the molecular weight of  $Al^{3+}$  ions. However, at the 60<sup>th</sup> cycle, the adsorption of  $Al^{3+}$  becomes more predominant in comparison to the adsorption of  $Al(OH)^{2+}$  ions. The mathematically modeled molecular masses of active ions from the EQCM

data suggest the concurrent adsorption of two species:  $\text{Al}(\text{OH})^{2+}$  and  $\text{Al}^{3+}$  ions on the Pt surface (Figure 9 (a) and (b)). Based on these assumptions, the proposed mechanism is illustrated in Figure 9(f).



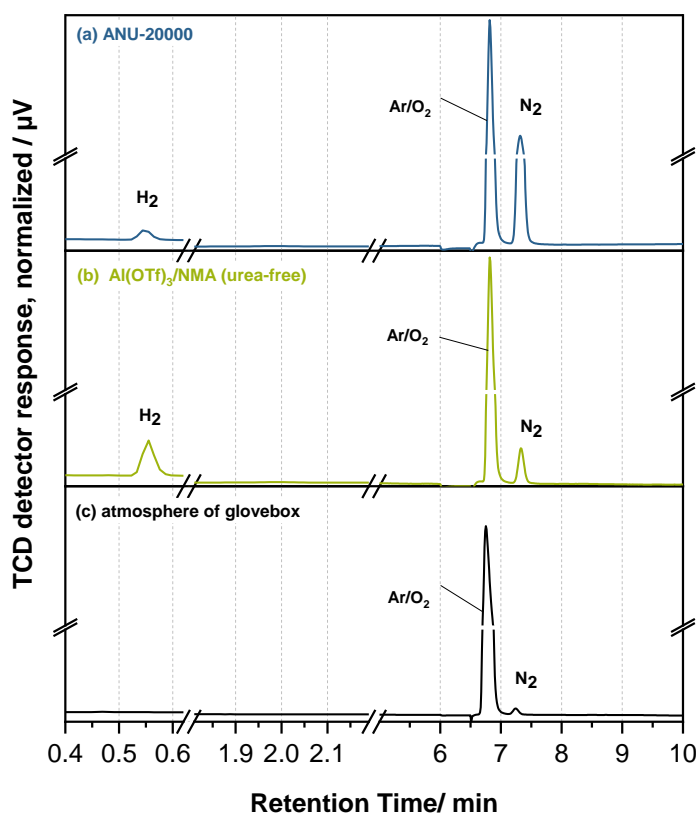
**Figure 9.** Electrode mass change vs. charge for the (a) 6<sup>th</sup> (b) 60<sup>th</sup> cycles, and potential vs. charge for the (c) 6<sup>th</sup> (d) 60<sup>th</sup> cycles during CV measurement at a scan rate of 20 mVs<sup>-1</sup> on 5 MHz Pt-coated quartz crystal WE in the ANU-20000 electrolyte for cycles. The blue and black solid lines are measured mass change (EQCM), red and green lines are the theoretical mass change of neat ions calculated from Faraday's law. (f) The proposed mechanism.

The results of this study suggest that the hydrogen evolution reaction can coexist with Al solvating complex dissociation within the water-containing electrolyte near the Pt electrode

surface. This implies that vacuum drying of the electrolyte at elevated temperatures, according to the literature,<sup>26</sup> is insufficient. For instance,  $\text{Al}(\text{OTf})_3$  salt contains crystalline water, which cannot be removed by thermal desorption.<sup>19</sup>

## 4.2 The Impact of urea on electrochemical reactions

To explore the possibility of  $\text{N}_2$  formation as a result of urea decomposition during the polarization, an electrolyte with the composition of  $\text{Al}(\text{OTf})_3/\text{NMA}=0.05/0.95$  (urea-free) was prepared for comparison. The Pt electrode was polarized under the same conditions in the urea-free electrolyte and Figure 10 (b) for the GC spectrum of the collected gas. Comparative semiquantitative analysis of the GC spectra indicates a greater formation of  $\text{N}_2$  in the presence of urea, despite the shorter polarization time, underscoring urea's significant role in  $\text{N}_2$  formation.

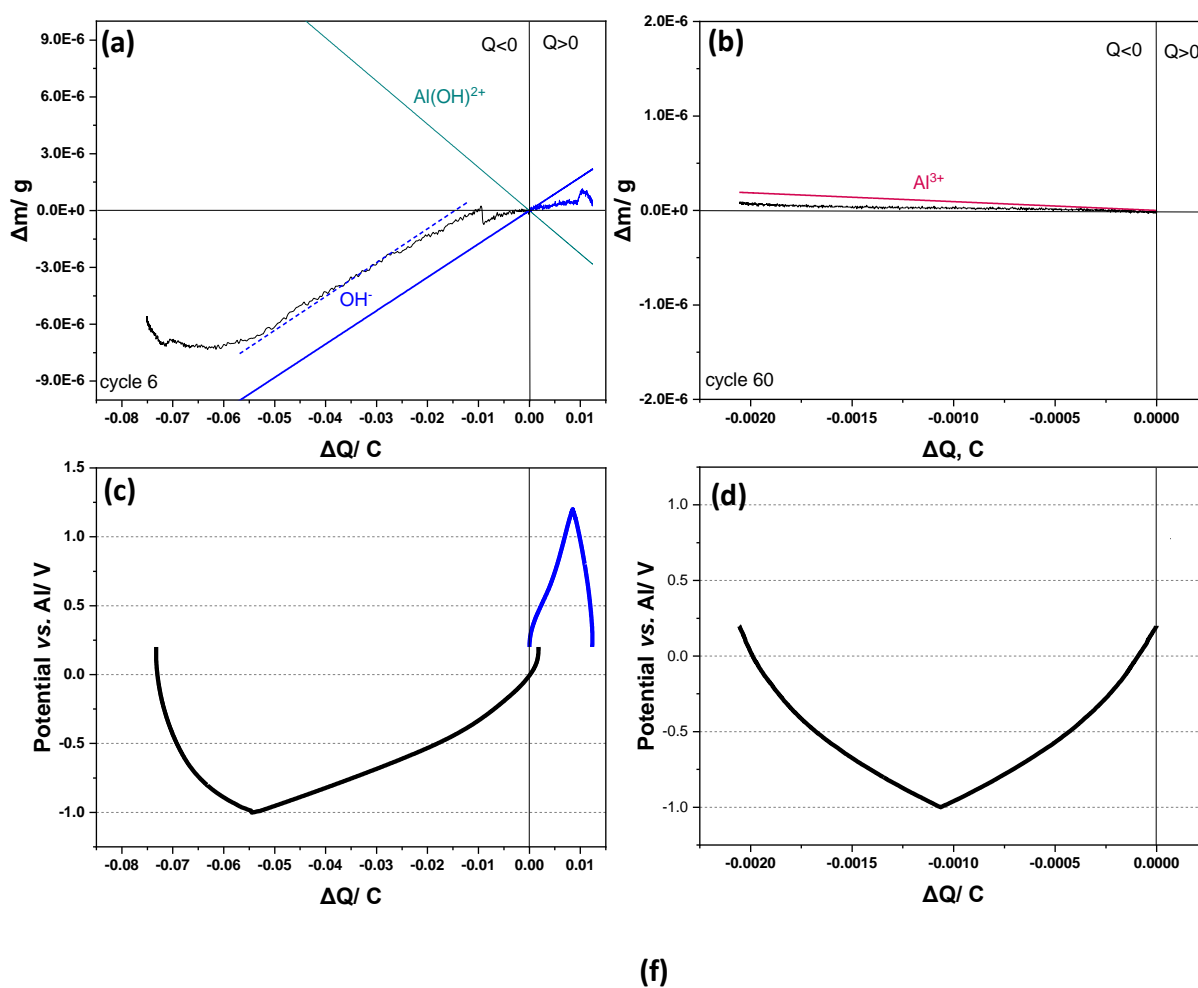


**Figure 10.** (a) GC spectrum of the collected gas after polarization of the Pt WE at -1 V vs. Al for 30 min in the ANU-2000 electrolyte (containing <20000 ppm of water). (b) GC spectrum of the collected gas after polarization of the Pt WE at -1 V vs. Al for 1 hour in the electrolyte without urea  $\text{Al}(\text{OTf})_3/\text{NMA}=0.05/0.95$  (c) GC spectrum of the collected gas from the atmosphere of the glovebox. The intensities of TCD responses are normalized with respect to the peak area of Ar from the glovebox atmosphere.

Moreover, the heightened hydrogen peak in the chromatogram for the urea-free electrolyte may be linked to the extended polarization duration. Because the GC analysis demonstrates the influence of urea on  $N_2$  gas formation in the electrolyte, further investigations were conducted to explore urea's effect on species adsorbing on the Pt surface during CV. Figure 11 shows the electrode mass change *vs.* charge passed (a) cycle 6<sup>th</sup> and (b) cycle 60<sup>th</sup> and potential *vs.* charge passed (c) cycle 6<sup>th</sup> and (d) cycle 60<sup>th</sup> obtained from the EQCM measurement during CV in the urea-free  $Al(OTf)_3/NMA$  electrolyte. EQCM results reveal less dissociation of  $Al(OTf)_3$  salt, potentially leading to a more intense desorption process of  $OH^-$  species during reduction, with no cation adsorption observed. Consequently, the process becomes irreversible and results in no cation activity during subsequent oxidation, as it has been shown in Figure 11.

Combining the results from GC and EQCM analyses of the urea-free electrolyte,  $N_2$  formation is likely linked to electrolyte decomposition, possibly occurring at the CE. The potential of CE (Al disc in the TSC surface cell) can exceed 3 V *vs.* Al during the measurements. It is important to highlight that when collecting the gas from the cell it is not possible to distinguish between gases generated at WE and CE. Therefore, precise identification of specific reactions involved in electrolyte decomposition and  $N_2$  formation requires further investigation, beyond the scope of this research





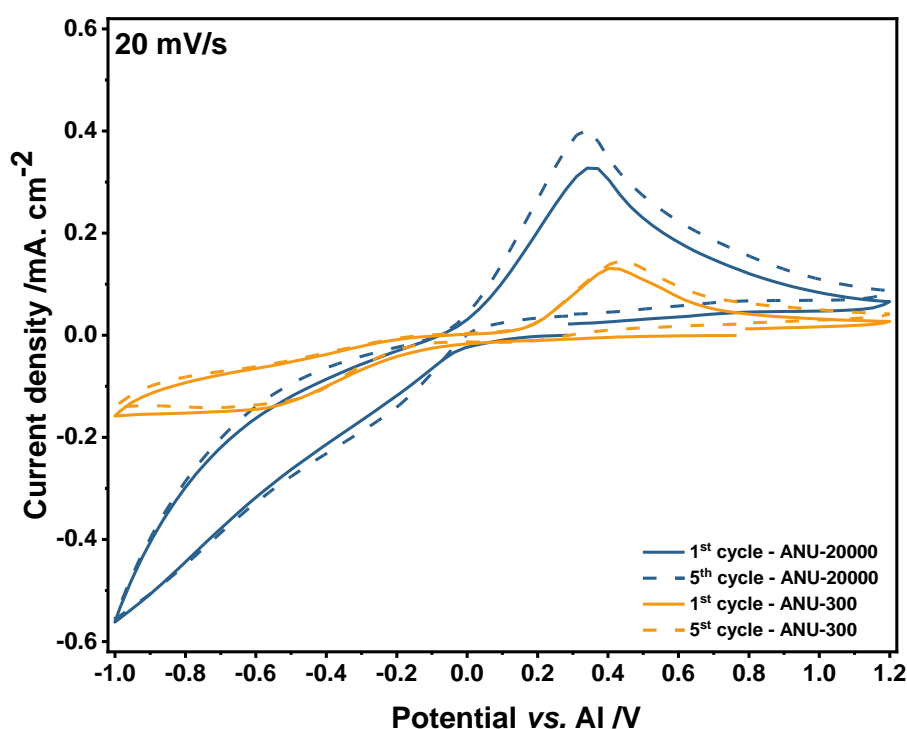
**Figure 11.** Electrode mass change vs. charge for the (a) 6<sup>th</sup> (b) 60<sup>th</sup> cycles, and potential vs. charge for the (c) 6<sup>th</sup> (d) 60<sup>th</sup> cycles during CV measurement on 5 MHz Pt-coated quartz crystal WE in the  $Al(OTf)_3/NMA$  electrolyte. The blue and black solid lines are measured mass change (EQCM), red and green lines are the theoretical mass change of neat ions calculated from Faraday's law. (f) The proposed mechanism.



### 4.3 Impact of water content on the electrochemical reactions

To emphasize the role of water content in the electrochemical reactions, we conducted supplementary experiments (CV, GC, and XPS) on an electrolyte with reduced water content. The ANU-300 electrolyte underwent a drying process, and the water content of this electrolyte was measured as 300 ppm, *via* KF titration. It is crucial to highlight that the drying of such electrolyte composition is not so simple and difficult to apply in real systems because it requires such a long time.

Figure 12 illustrates the CV measurements of the Pt electrode in the ANU-300 electrolyte compared with results obtained from electrolyte ANU-20000. The reductive and oxidative currents display a substantial reduction after the electrolyte drying process, unveiling a clear correlation between water content and current.



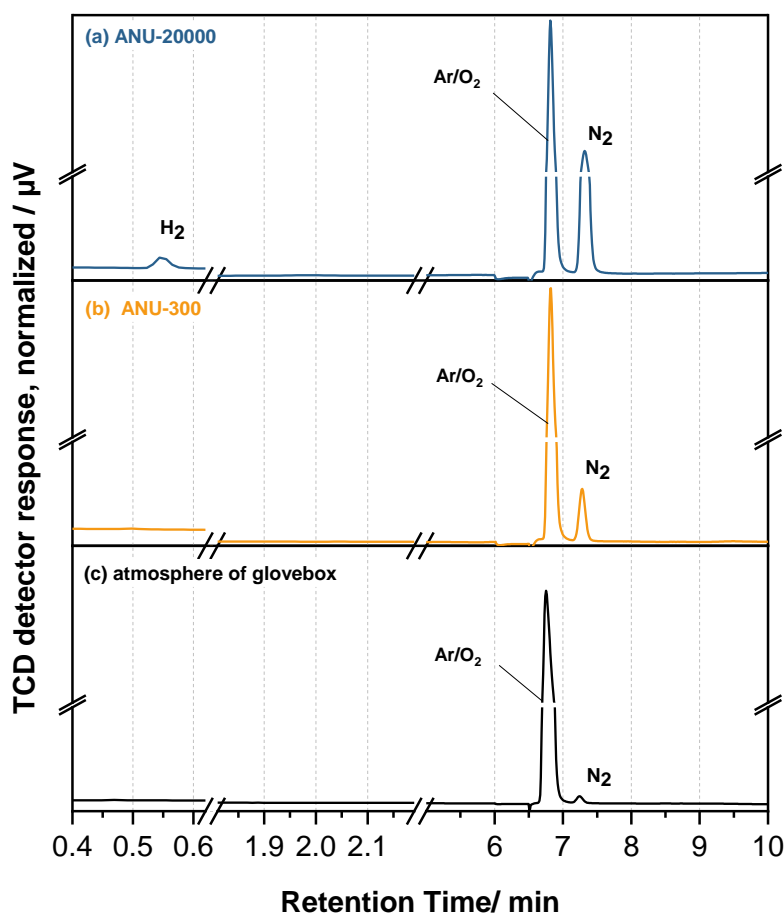
**Figure 12.** CV curves on the Pt WE in the ANU-20000 electrolyte (containing <20000 ppm of water) and the ANU-300 electrolyte (containing 300 ppm of water) at a scan rate of 20 mVs<sup>-1</sup>. Al were used as reference electrode and counter electrode.

To further validate the impact of water on the HER, GC analysis was conducted to assess the gases formed following the Pt polarized in the ANU-300 electrolyte, as shown in Figure 13 (b). This was compared with the GC measurement of the ANU-20000 electrolyte (Figure 13(a)). The gas produced during the 30 minutes was minimal, indicating a significant decrease in the

HER, with nearly undetectable  $\text{H}_2$  in the GC measurement.  $\text{N}_2$  was detected, possibly attributed to electrolyte decomposition. These measurements underscore that water is the predominant source of HER. Yet, a crucial question remains: does reducing the water content of the electrolyte facilitate meaningful Al plating?

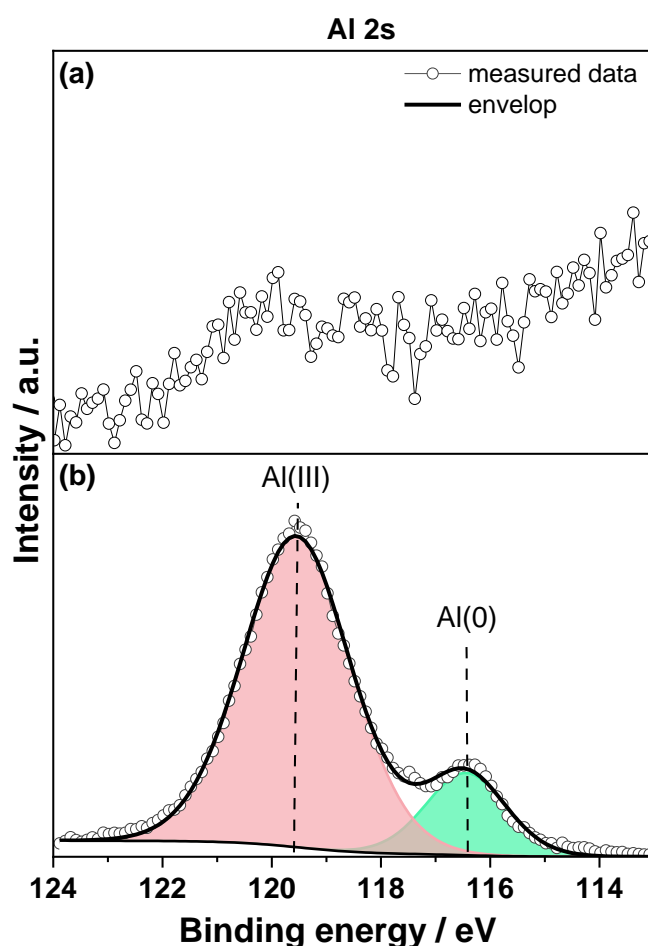
To address this question, XPS characterization was employed to examine the presence of metallic Al on Pt surfaces after polarization at -1 V vs. Al for 2 hours in the ANU-300 electrolyte.

It is noteworthy that the main photoelectron lines for Al and Pt, Al 2p and Pt 4f respectively, share the same binding energy range, hindering the investigation of eventual plated metallic Al solely through Al 2p (overlap). To overcome this, the Al 2s photoelectron line was utilized to determine the presence of metallic Al on the Pt electrode surface (Figure 14 (a)) by comparison with the Al 2s spectrum of Al metal foil (Figure 14 (b)) as a reference sample.



**Figure 13.** (a) GC spectrum of the collected gas after polarization of the Pt WE at -1 V vs. Al for 30 min in the ANU-2000 electrolyte (containing <20000 ppm of water). (b) GC spectrum of the collected gas after polarization of the Pt WE at -1 V vs. Al for 30 min in the ANU-300 electrolyte (containing 300 ppm of water) (c) GC spectrum of the collected gas from the atmosphere of the glovebox. The intensities of TCD responses are normalized with respect to the peak area of Ar from the glovebox atmosphere.

The Al 2s spectrum of Al metal foil exhibits two peaks at 116.5 eV and 119.6 eV, correlating to metallic Al (Al(0)) and Al native oxide (Al(III)) on the surface, respectively. The spectra of Al 2s for the Pt electrode, Figure 14 (a), were not fitted due to the poor signal-to-noise ratio. It is likely because of the very small amount of Al on the surface (near the detection limit). However, upon comparing the Al 2s spectra of Al foil with those on Pt after polarization, the absence of metallic Al peak around 116.5 eV is evident. A small increase in the signal at around 120 eV is observed, potentially attributed to Al(III). This may be due to residue from the electrolyte remaining on the surface after washing with methanol. This implies that even after reducing the water content, the residue of water may still interfere with Al plating. Unfortunately, no plated Al could be identified using the experimental conditions applied.



**Figure 14.** Al 2s spectra of (a) the Pt WE after polarization at -1 V vs. Al for 2 hours in the ANU-300 (containing 300 ppm water) and (b) Al metal foil.

## 4.4 The key findings of this chapter

This chapter investigated the Al plating possibility on the Pt electrode from  $\text{Al}(\text{OTf})_3/\text{NMA}/\text{urea}$  (ANU-20000) electrolyte in the molar fraction of 0.05/0.76/0.19, which is one of the previously proposed alternatives to  $\text{AlCl}_3$ -based electrolytes has been examined. While the electrolyte exhibited redox currents (a reduction current followed by the corresponding oxidative current), these are attributed to HER rather than Al plating. This conclusion is supported by  $\text{H}_2$  detection and the absence of conclusive Al plating evidence through SEM analysis.

Further investigation using EQCM revealed an adsorption/desorption corresponding to  $\text{Al}(\text{OH})^{2+}$  and  $\text{Al}^{3+}$  ions on the Pt surface during cycling. The presence of urea facilitated the dissociation of solvated Al species, leading to the preferential adsorption of  $\text{Al}^{3+}$  ions after extended cycling. However, these adsorbed ions do not translate to successful Al plating due to competing side reactions.

In the absence of urea, the complete dissociation of  $\text{Al}(\text{OTf})_3$  and reversible cation adsorption are not observed. A low-water version of the electrolyte (ANU-300) reduces the hydrogen evolution reaction, although XPS analysis does not definitively confirm Al plating, suggesting limitations in the technique's detection limit or the plating process itself. Another possibility might be that residual water-related substances in the electrolyte still hinder the plating of Al on the Pt surfaces or the composition of the electrolyte itself is not compatible with achieving successful Al plating or stripping.

In addressing the challenges of Al plating and stripping, an approach for wider adoption within society might be exploring alternative Al salt sources by synthesizing them, rather than using the commercially available  $\text{Al}(\text{OTf})_3$ . Additionally, investigating alternative electrolyte combinations using dry solvents, ideally with enhanced solubility for the synthesized Al salt, holds promise. Notably, the limited achievable concentration of  $\text{Al}(\text{OTf})_3$  within the NMA/urea mixture may contribute to the observed incompatibility with Al plating.

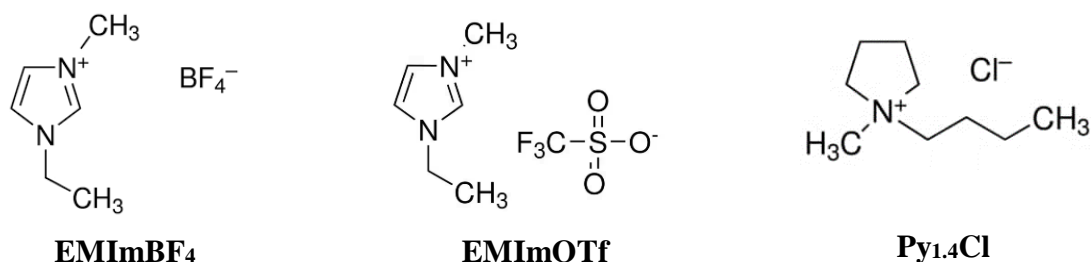
Given the challenges associated with developing  $\text{AlCl}_3$ -free electrolytes, an alternative strategy involves applying inhibitors in the chloroaluminate ionic liquid electrolytes to mitigate their corrosivity. This strategy will be explored in greater detail in the following chapter.

## 5 Mitigating corrosivity of $\text{AlCl}_3\text{:EMImCl}$ electrolyte using inhibitors

RTILs, particularly chloroaluminate ionic liquid electrolytes composed of  $\text{AlCl}_3$  and imidazolium chloride (EMImCl) with a molar ratio of higher than 1, have been studied for their application in rechargeable aluminum batteries (RABs). However, these electrolytes are highly corrosive to various metals. This not only poses safety hazards, especially in the event of accidental cell leakage but also complicates the selection of suitable cell components, such as current collectors. For instance, stainless steels, a conventional current collector material, suffer from severe corrosion<sup>5,6,20</sup>.

To mitigate the corrosive nature of these electrolytes, we are investigating the use of additives as inhibitors. These inhibitors function by adsorbing onto the surface of the current collector to form a protective layer, thereby reducing corrosion rates. Recent studies have shown that imidazolium-based ionic liquids exhibit promising corrosion inhibition properties for mild steel and stainless steels in aggressive acidic solutions used in industries such as solutions containing HCl.<sup>44,45,138</sup> These compounds can adsorb onto metallic surfaces *via* electron lone pairs on nitrogen (N) atoms, effectively protecting them from corrosion. Additionally, 1-Butyl-1-methylpyrrolidinium chloride ( $\text{Py}_{1.4}\text{Cl}$ ) has demonstrated potential in passivating AISI 316L surfaces in magnesium battery electrolytes containing magnesium chloride complexes.<sup>139</sup>

Considering the excellent corrosion resistance of AISI 316L in various environments, including chloride solutions, it was selected as a potential current collector in the chloroaluminate ionic liquid electrolytes composed of  $\text{AlCl}_3$  and EMImCl in a 1.5:1 ratio for this study. Inhibitors such as 1-Ethyl-3-methylimidazolium tetrafluoroborate ( $\text{EMImBF}_4$ ), 1-Ethyl-3-methylimidazolium trifluoromethanesulfonate ( $\text{EMImOTf}$ ), and  $\text{Py}_{1.4}\text{Cl}$  were chosen to reduce the corrosion rate of AISI 316L in this electrolyte. Figure 15 depicts the chemical structure of these inhibitors.



**Figure 15.** The chemical structure of the inhibitors EMImBF<sub>4</sub> (1-ethyl-3-methylimidazolium tetrafluoroborate), EMImOTf (1-ethyl-3-methylimidazolium trifluoromethanesulfonate), and Py<sub>1.4</sub>Cl (1-butyl-1-methylpyrrolidinium chloride).

The idea behind using EMImOTf and EMImBF<sub>4</sub> as inhibitors, apart from evaluating their effectiveness, was to examine the influence of anions (OTf<sup>-</sup> and BF<sub>4</sub><sup>-</sup>), whether through direct interaction or by affecting EMIm<sup>+</sup> cation adsorption. When the AISI 316L is immersed in the electrolyte, the EMIm<sup>+</sup> cation can adsorb onto the negatively charged metal surface *via* the N-heteroatom and limit corrosion by reducing active sites. In this context, OTf<sup>-</sup> and BF<sub>4</sub><sup>-</sup> anions are used instead of Cl<sup>-</sup>, as the bulky and large size of these anions is expected to facilitate adsorption of the EMIm<sup>+</sup> on the AISI 316L surface more effectively than Cl<sup>-</sup>, thus offering enhanced corrosion resistance. At higher potentials, the anions from the inhibitors are expected to adsorb onto the positively charged AISI 316L surface, directly mitigating corrosion.

On the other hand, the Py<sub>1.4</sub>Cl inhibitor offers the advantage of having a more localized charge on the single N atom in the Py<sup>+</sup> cation compared to the two N atoms in the imidazolium ring of EMIm<sup>+</sup>. This characteristic is expected to result in more stable adsorption of Py<sup>+</sup> on the metal surface, thereby enhancing corrosion resistance.

Due to the complexity of naming inhibitors throughout the text, electrolytes have been assigned labels to simplify recall. For instance, an electrolyte comprising AlCl<sub>3</sub> and EMImCl in a molar ratio of 1.5:1 is denoted as A15E1. Subsequently, upon adding 2 wt% of inhibitors such as Py<sub>1.4</sub>Cl, EMImOTf, and EMImBF<sub>4</sub>, the electrolyte variations are referenced as A15E1Py2, A15E1OTf2, and A15E1BF2, respectively. The selection of 2 wt% inhibitor concentration was based on its impact on Al plating and stripping behavior at the negative electrode, as will be discussed in greater detail in chapter 5.2.1. There are various inhibitor ratios (1, 2, 5, and 10 wt% EMImBF<sub>4</sub>), and their impact on Al plating and stripping as an example is illustrated.

In the following section, the effect of inhibitors on the corrosion of AISI 316L was assessed using potentiodynamic polarization measurements. The corrosion rates of AISI 316L in electrolytes with and without inhibitors at open circuit voltage (OCV) were determined,

simulating the interaction of AISI 316L with the electrolyte. Additionally, considering the applied potential during the charging/discharging process, the corrosion of AISI 316L at higher potentials was also evaluated. The potentiodynamic polarization measurements were combined with XPS surface analysis to monitor the surface changes of AISI 316L when exposed solely to the electrolyte and when subjected to high potential.

## 5.1 Impact of inhibitors on corrosion behavior of AISI 316L

### 5.1.1 Evaluation of corrosion current density *via* electrochemical assessments

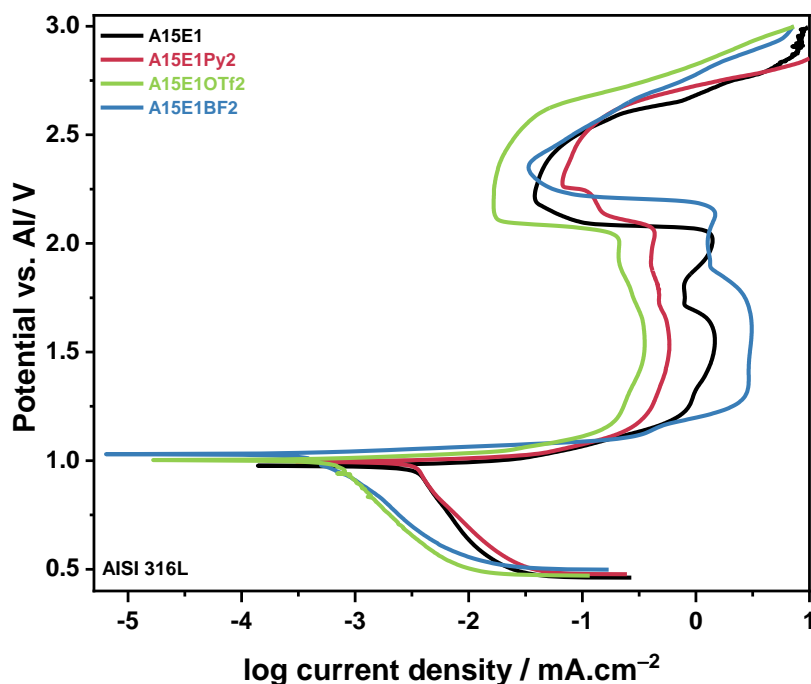
The study of AISI 316L corrosion behavior in electrolytes with and without inhibitors was conducted *via* potentiodynamic polarization tests. Figure 16 depicts the potentials *versus* the logarithm of current densities for the AISI 316L samples in various electrolytes. Tafel slope extrapolation was applied in the vicinity of the OCV to identify the intersection of extrapolated anodic and cathodic currents and to determine the corrosion potential ( $E_{\text{corr}}$ ) and current density ( $I_{\text{corr}}$ ), which are summarized in Table 4.

It is worth noting that our main objective is to comprehend the behavior of the inhibitors and their impact on AISI 316L corrosion. As the precise  $I_{\text{corr}}$  value is not our primary focus, the data in Table 4 represents average values derived from a minimum of 3 repetitions for each measurement. Although Figure 16 only shows one curve per measurement, this curve is representative of the reproducible results. These averages offer reliable estimations, minimizing interpretational errors. Additionally, the standard error, which is the standard deviation of the mean values, is reported to highlight the uncertainty stemming from potential errors.

To account for potential errors in inhibition efficiencies (IE) of inhibitors, we used the upper-lower bound method, as a straightforward estimation of the standard error of IE. While the propagation of uncertainty method is more precise, its complex calculations are unnecessary for our primary focus. In this method, we calculated IE using the upper and lower bounds of both the  $I_{\text{corr}}^{\circ}$  and  $I_{\text{corr}}$ , to capture the maximum possible variation in the IE. The standard error reported is half the range of the maximum variation of IE.

Results suggest that inhibitors lowered  $I_{\text{corr}}$  at OCV, with varying degrees. This suppression of corrosion likely stems from the formation of a protective layer of adsorbed inhibitor molecules on AISI 316L surfaces when exposed to electrolytes-containing inhibitors. Notably, A15E1OTf2 electrolyte exhibits more pronounced changes compared to A15E1BF2. The

values of  $E_{\text{corr}}$  for AISI 316L are not significantly changed by inhibitor addition, only slightly shifted to a positive direction.



**Figure 16.** Potentiodynamic polarization curves for AISI 316L in various electrolytes with and without the presence of inhibitors. The polarization scan ranged from -0.5 V vs. OCV to 3 V vs. Al at a scan rate of 1 mVs<sup>-1</sup>. An Al CE and an Al pseudo-reference electrode were used.

The IE provides an understanding of the performance of inhibitors with a reasonable level of reliability, even when the precise  $I_{\text{Corr}}$  values are not the main concern. The reported IEs reveal that EMImOTf appears as the most effective inhibitor, while EMImBF<sub>4</sub> is noted as the least reliable, which can potentially also be the least effective.

**Table 4.** Calculated corrosion potentials and corrosion current densities from the Tafel slope extrapolations and the inhibition efficiency of the inhibitors in the electrolytes.

Electrolyte	$I_{\text{corr}}$ ( $\mu\text{A}\cdot\text{cm}^{-2}$ )	$E_{\text{corr}}$ (mV)	IE%
A15E1	$4.4\pm0.1$	$847\pm17$	-
A15E1Py2	$2.7\pm0.6$	$918\pm7$	$39\pm15$
A15E1OTf2	$1.6\pm0.4$	$922\pm11$	$64\pm9$
A15E1BF2	$3.1\pm0.8$	$877\pm14$	$30\pm20$

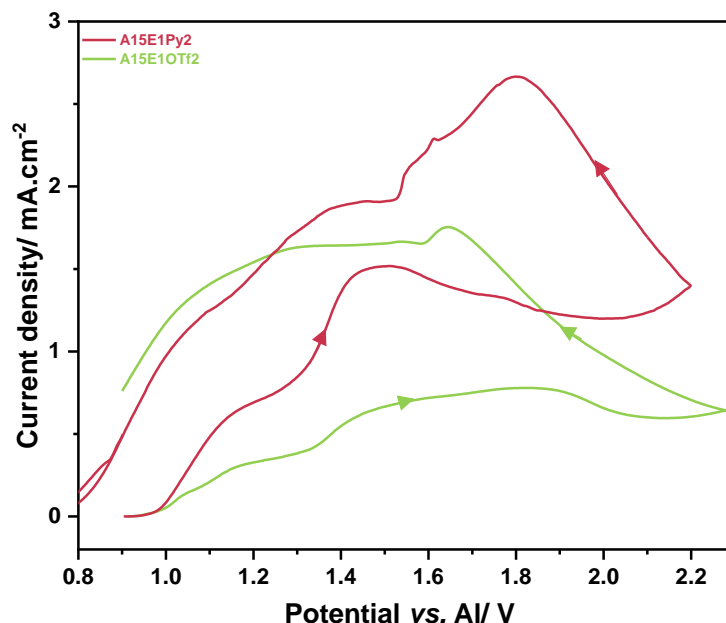


Figure 16 displays the complete polarization curves for the various listed electrolytes. The current observed after the Tafel region increases significantly, indicating that no passivation layer has formed on the AISI 316L surface. It is more likely that the corrosion current density has been limited in the higher potential range due to diffusion control, possibly stemming from the accumulation of corrosion products on the AISI surface with corrosion products such as iron (II) chloride ( $\text{FeCl}_2$ ).

The adsorption of  $\text{Cl}^-$  ions, facilitated by increasing the potential to more positive values, can break the passivation layer on AISI316L through a local attack on the chromium(III) oxide ( $\text{Cr}_2\text{O}_3$ ) layer.<sup>140</sup> The adsorption of inhibitor molecules on the surface of AISI 316L may not effectively prevent the adsorption of  $\text{Cl}^-$ , and therefore, the corrosion process may continue even in the presence of inhibitors.

The exact value of the current in this area is not of primary interest because it can be influenced by several factors, including the risk of the unhomogenized surface of AISI 316L foil as well as errors such as human errors and random errors. Yet, given the high current observed in this region for all the electrolytes, it can be expected that the buildup of corrosion products on the surface of AISI 316L limited the current density. To investigate further if a stable and protective layer has formed on AISI 316L in A15E1Py2 and A15E1OTf2 at high potential, AISI 316L is polarized up to 2.2 V vs. Al and then the potential is returned to around 0.9 V vs. Al. If a protective layer forms on the surface of these two electrolytes, the current density in the reverse scan should be lower. However, as evidenced in Figure 17, the current density further increased in the reverse scan. This is likely caused by a combination of inhibitor adsorption and the build-up of unstable corrosion products. These products can dissolve, leaving the exposed surface susceptible to further corrosion.

Since these corrosion products may not remain stable on the surface each time the experiment is conducted, the exact current value is not consistently reproducible, and this variability should be considered in the interpretation. However, it is important to consider the trend in the behavior of the inhibitors.

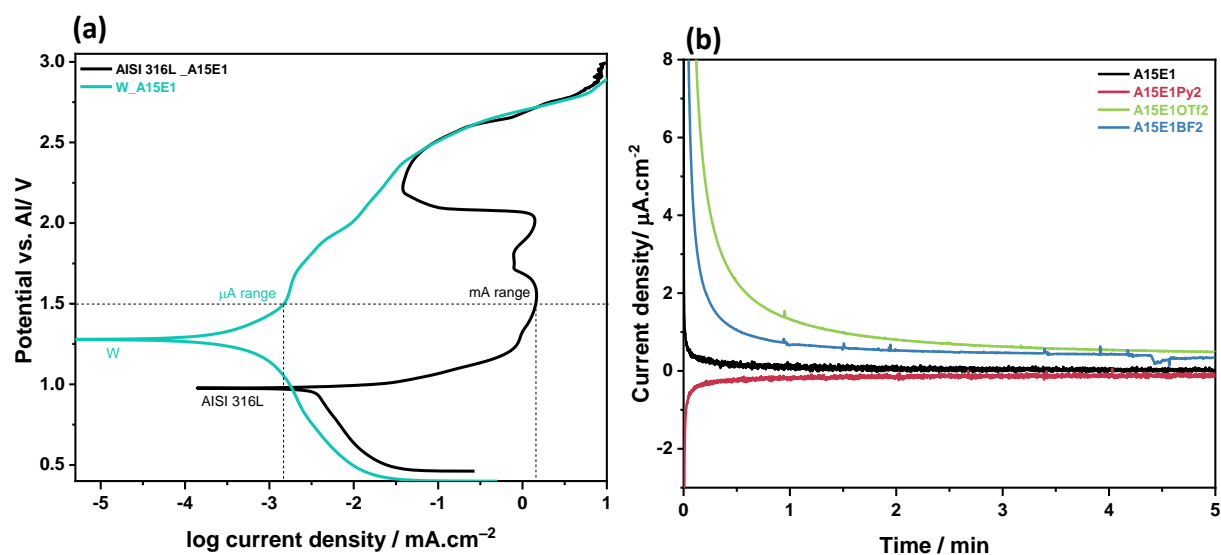


**Figure 17.** CV curves of AISI 316L polarized from OCV up to 2.2 V *vs.* Al and scanned back again in A15E1Py2 and A15E1OTf2. Al foils were used as CE and pseudo-reference. The scan rate was 1 mVs<sup>-1</sup>.

The Py<sub>1.4</sub>Cl and EMImOTf inhibitors result in lower current densities of AISI 316L both at OCV and at the higher potentials, however, EMImBF<sub>4</sub> inhibitor causes an increase in current densities at high potential. Interestingly, this is contrary to the behavior of the AISI 316L at OCV in A15E1BF<sub>2</sub>. This increase in current densities at high potential might be due to the decomposition of the inhibitor or accelerated corrosion of AISI 316L in the presence of the inhibitors.

To investigate the possibility of inhibitor decomposition at high potentials, tungsten (W) was employed as a non-corroding electrode. Potentiodynamic polarization measurements (Figure 18 (a)) show that W, unlike AISI 316L, exhibits significantly lower current densities (microampere range) at high potentials in A15E1, indicating minimal corrosion. Subsequently, W was polarized at 1.5 V *vs.* Al in all electrolytes (Figure 18(b)). W exposed to A15E1OTf2 and A15E1BF2 displayed an oxidation current, suggesting possible adsorption (and/or decomposition) of the anionic part of the inhibitor on its surface. Conversely, W in A15E1 and A15E1Py2 showed near-zero current density, implying minimal interaction of W with these electrolytes at this potential. The potential of 1.5 V *vs.* Al was chosen for further XPS investigation due to two considerations. Firstly, this potential is expected to reveal more pronounced surface changes on AISI 316L due to the observed variations in current densities across different electrolytes. Secondly, it remains a safe operating potential, well below the

metal dissolution threshold of around 2 V vs. Al. This ensures that the observed surface modifications are primarily due to inhibitor behavior and not substantial metal breakdown.



**Figure 18.** (a) Potentiodynamic polarization curves for W and AISI 316L in A15E1 electrolytes. The polarization scan ranged from -0.5 V vs. OCV to 3 V vs. Al at a scan rate of 1 mVs<sup>-1</sup>. An Al CE and an Al quasi-reference electrode were used. (b) CA measurement using the W working electrode, which is polarized at 1.5 V vs. Al for 5 min in various electrolytes with and without inhibitors. An Al CE and an Al quasi-reference electrode were used.

### 5.1.2 Surface characterization of AISI 316L using XPS

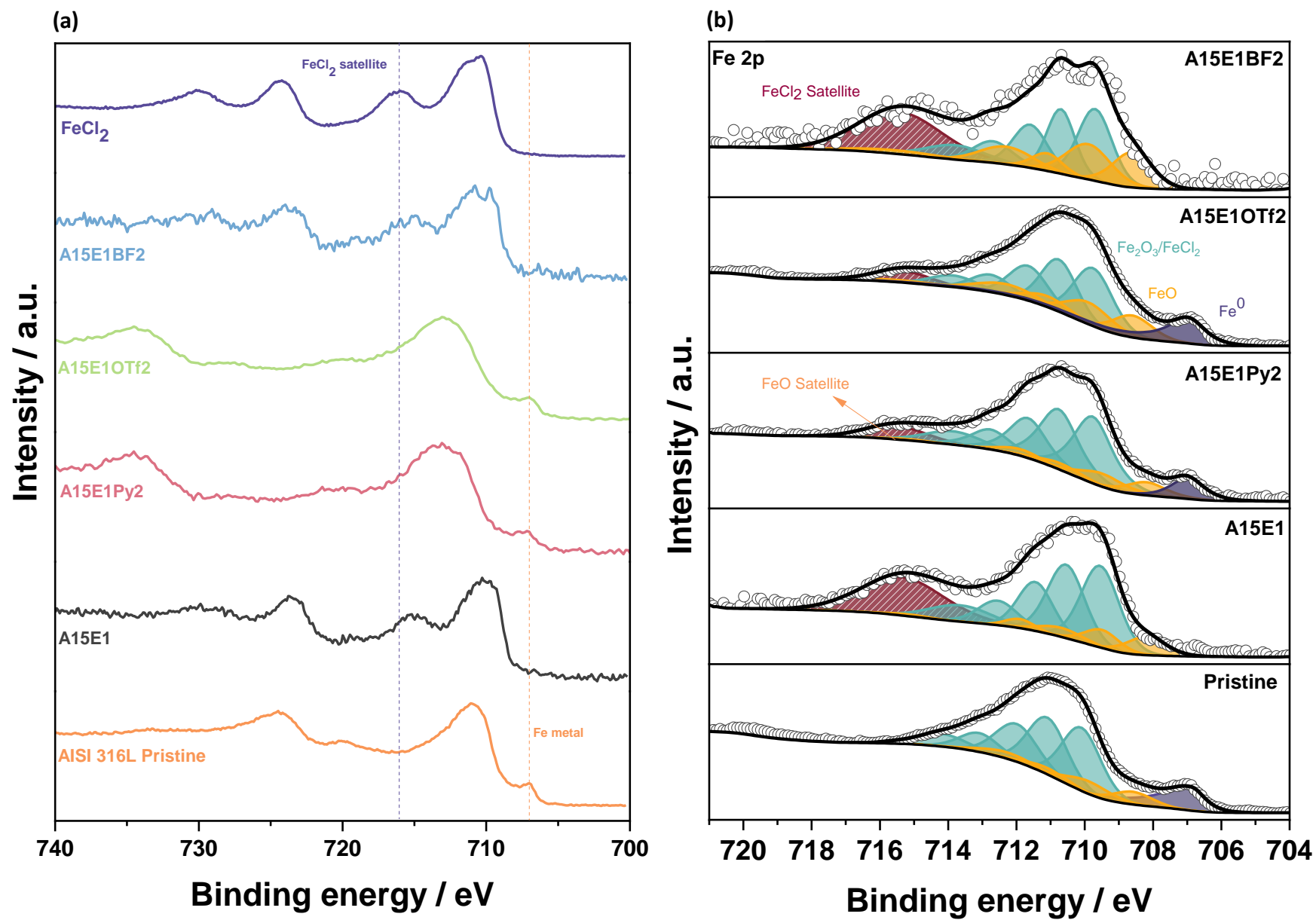
To further understand the surface composition of AISI 316L and identify possible species formed in the presence of inhibitors, we conducted XPS characterization on two series of samples. Firstly, AISI 316 foil was immersed in electrolytes with and without inhibitors, which represents the OCV condition in potentiodynamic polarization measurements and secondly, AISI 316 foils were polarized at 1.5 V vs. Al for 1 minute in different electrolytes as a representative of the higher potential condition. The 1-minute polarization time was chosen for a specific reason. The excess polarization time significantly alters the AISI 316L surface. A 5-minute polarization time at 1.5 V vs. Al was previously attempted but the results were unsuitable for XPS analysis. Because a thick and uneven layer of corrosion products formed. This increased surface heterogeneity, leading to difficulties in removing excess electrolytes for XPS analysis. These changes ultimately render the iron (Fe) spectra detectable using XPS, hindering the evaluation of the surface composition. Therefore, a 1-minute duration was chosen as a balance between capturing relevant information and maintaining a surface suitable for XPS analysis.

### 5.1.2.1 XPS studies of immersed AISI 316L in the electrolyte containing inhibitors

To comprehend the corrosion behavior of AISI 316L in the electrolyte, the Fe spectra of various samples were initially compared as depicted in Figures 19 (a) and (b). Due to the complexity of fitting several multiplet peaks from iron oxides and iron chloride, and the resulting overlap of their binding energies, the approach which was involved comparing the overall shape of Fe 2p spectra with the AISI 316L pristine sample, as a reference with a native oxide film and a FeCl<sub>2</sub> reference spectrum (directly sourced from the knowledge view of Avantage software version 5.9931) was adopted. In this comparison, emphasis was placed on the peak associated with metallic iron, and the satellite peak related to the FeCl<sub>2</sub> as a primary indicator of corrosion. A more pronounced metal iron peak and a lower peak associated with the FeCl<sub>2</sub> satellite suggest less corrosion and fewer chloride species covering the surface.

Subsequently, the Fe spectra of the samples were also fitted to gain more insights into the surface layer, as illustrated in Figure 19 (b). Notably, iron chloride species and iron oxide species such as iron (II) oxide (FeO) and iron (III) oxide (Fe<sub>2</sub>O<sub>3</sub>) should be fitted by multiplet peaks, which complicate the analysis due to overlapping peaks. To address this, the fitting model for the Fe spectra was limited to multiplet peaks for FeO and Fe<sub>2</sub>O<sub>3</sub>, which in fact also involve iron chloride species due to their similar peak position with the oxides. The binding energy differences between multiplet peaks and the relative ratios of peak heights and full width at half maximum (FWHM) of peaks for different iron species were selected based on literature data.<sup>141,142</sup> These multiplets are labeled as FeO and Fe<sub>2</sub>O<sub>3</sub>/FeCl<sub>2</sub> in the spectra. However, distinct satellite peaks corresponding to FeCl<sub>2</sub> and FeO served as clear indicators of the species present on the surface. The satellite peak of Fe<sub>2</sub>O<sub>3</sub>, which is far from those of FeO and FeCl<sub>2</sub>, closely aligns with the Fe metal 2p<sub>1/2</sub> peak, making it difficult to distinguish; thus, it has not been shown here.

It is worth mentioning that iron chloride can exist as either FeCl<sub>3</sub> or FeCl<sub>2</sub>. However, according to the literature, the binding energy of FeCl<sub>3</sub> and FeCl<sub>2</sub> satellite peaks differs by approximately 0.5 eV (the satellite peak corresponding to FeCl<sub>3</sub> is more positive).<sup>141</sup> By examining the Fe spectra obtained for the samples, it can be concluded that the formation of FeCl<sub>3</sub> is unlikely. In contrast, the presence of FeCl<sub>2</sub> is more probable, as indicated by the observed satellite peak binding energy in the Fe 2p spectra.



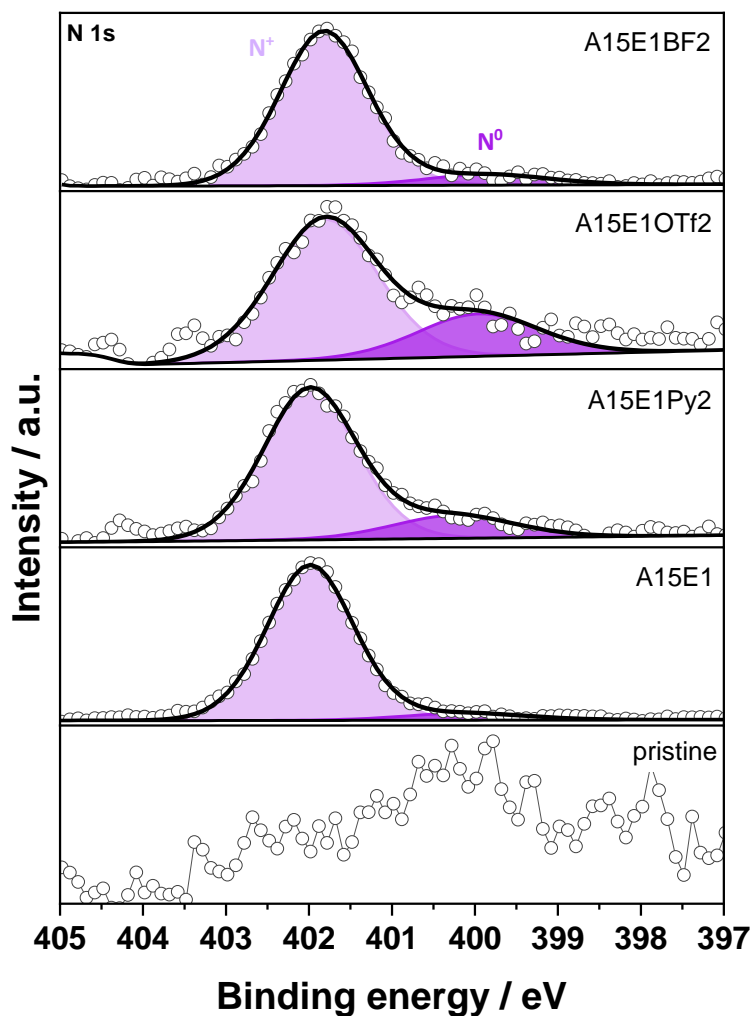
**Figure 19.** The Fe 2p spectra for AISI 316L immersed in various electrolytes (a) Full spectra comparing the shapes with AISI 316L pristine foil and FeCl<sub>2</sub> spectra. (b) Fitted Fe 2p spectra highlighting the FeCl<sub>2</sub> satellite peak.

By comparing the Fe 2p spectra for AISI 316L samples immersed in various electrolytes, alongside the AISI 316L pristine and FeCl<sub>2</sub> spectra, as shown in Figure 19 (a) and (b) the following observations were made:

1. **Samples immersed in A15E1 and A15E1BF2:** These samples do not exhibit a peak related to Fe metal. Additionally, the satellite peaks associated with FeCl<sub>2</sub> are more clearly observed for these two samples compared to the others. This suggests that the surfaces of these samples are likely covered by iron chlorides, indicating that the inhibitor has less effect in protecting the surface from corrosion.
2. **Samples immersed in A15E1OTf2 and A15E1Py2:** These samples show a Fe metal peak at around 706.6 eV and lower intensities of the FeCl<sub>2</sub> satellite peak. This indicates that these samples likely experienced less surface corrosion. This conclusion from XPS measurement can be further supported by results from the potentiodynamic polarization measurements. AISI 316L shows lower  $I_{\text{corr}}$  values in A15E1OTf2 and A15E1Py2 in comparison to the A15E1BF2 and A15E1 electrolytes.

It has been mentioned that inhibitors prevent corrosion by adsorbing onto the surface through the N in the EMIm<sup>+</sup> ring.<sup>120,121,139</sup> To confirm the presence of these inhibitors on the surface of AISI 316L when immersed in electrolytes, N 1s spectra were analyzed, as shown in Figure 20. In the pristine sample, N content is notably low. However, in all other samples, a signal at 401.8 eV is evident, attributed to the positively charged N atom in the imidazolium ring (EMIm<sup>+</sup>), indicating the presence of adsorbed EMIm<sup>+</sup> cations from the electrolyte and/or residue from the electrolyte after washing.

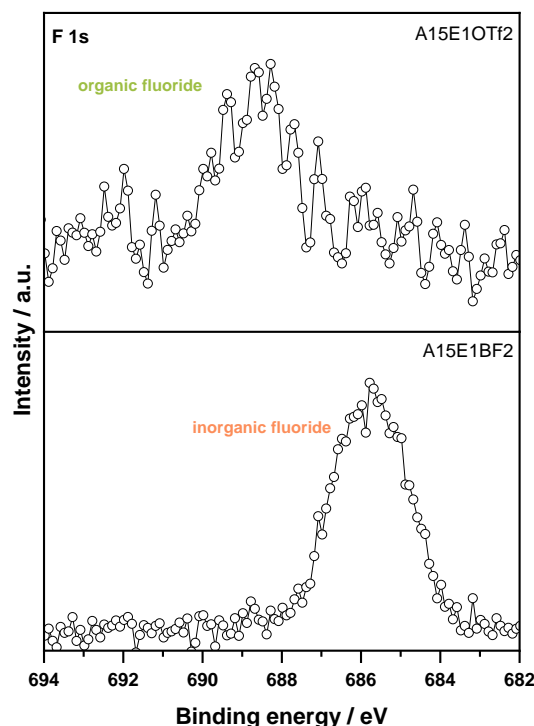
Another peak, situated around 400 eV, is attributed to neutral N, likely stemming from the reduction of EMIm<sup>+</sup> on the surface. This peak is more pronounced with respect to the peak related to N<sup>+</sup> for AISI 316L immersed in A15E1OTf2. Considering the relatively higher Fe metal peaks in the Fe spectra for this sample, it can be assumed that the surface has undergone fewer changes and is most likely less corroded. This observation suggests that the presence of reduced cations on the AISI 316L surface might mitigate corrosion by forming a protective layer. This is further confirmed by the lower  $I_{\text{corr}}$  measured in potentiodynamic polarization on AISI 316L when compared to the other inhibitor-containing electrolytes. The increase in reduced EMIm on the surface in the case of A15E1OTf2 might be correlated to the larger anion of OTf compared to Cl<sup>-</sup> (as in EMImCl), which likely facilitates the adsorption of EMIm on the surface.



**Figure 20.** N 1s spectra of AISI 316L samples immersed in different electrolytes, as well as the AISI 316L pristine foil.

It is worth mentioning that in the A15E1Py2 electrolyte, the peaks related to positively charged and neutral N can be attributed to both EMIm and Py cations, which adsorb on the surface. The relatively higher peak related to neutral N, can be seen here compared to A15E1, which can further relate to the small decrease in  $I_{\text{corr}}$  observed in this electrolyte. Notably, no additional peak was observed in the N 1s spectrum when the additive was applied to the A15E1 electrolyte.

To understand the effects of OTf<sup>-</sup> and BF<sub>4</sub><sup>-</sup> anions on the corrosion of AISI 316L and whether any decomposition products form on the surface when these inhibitors are present, the F 1s spectra for AISI 316L immersed in A15E1OTf2 and A15E1BF2 electrolytes, are depicted in Figure 21.



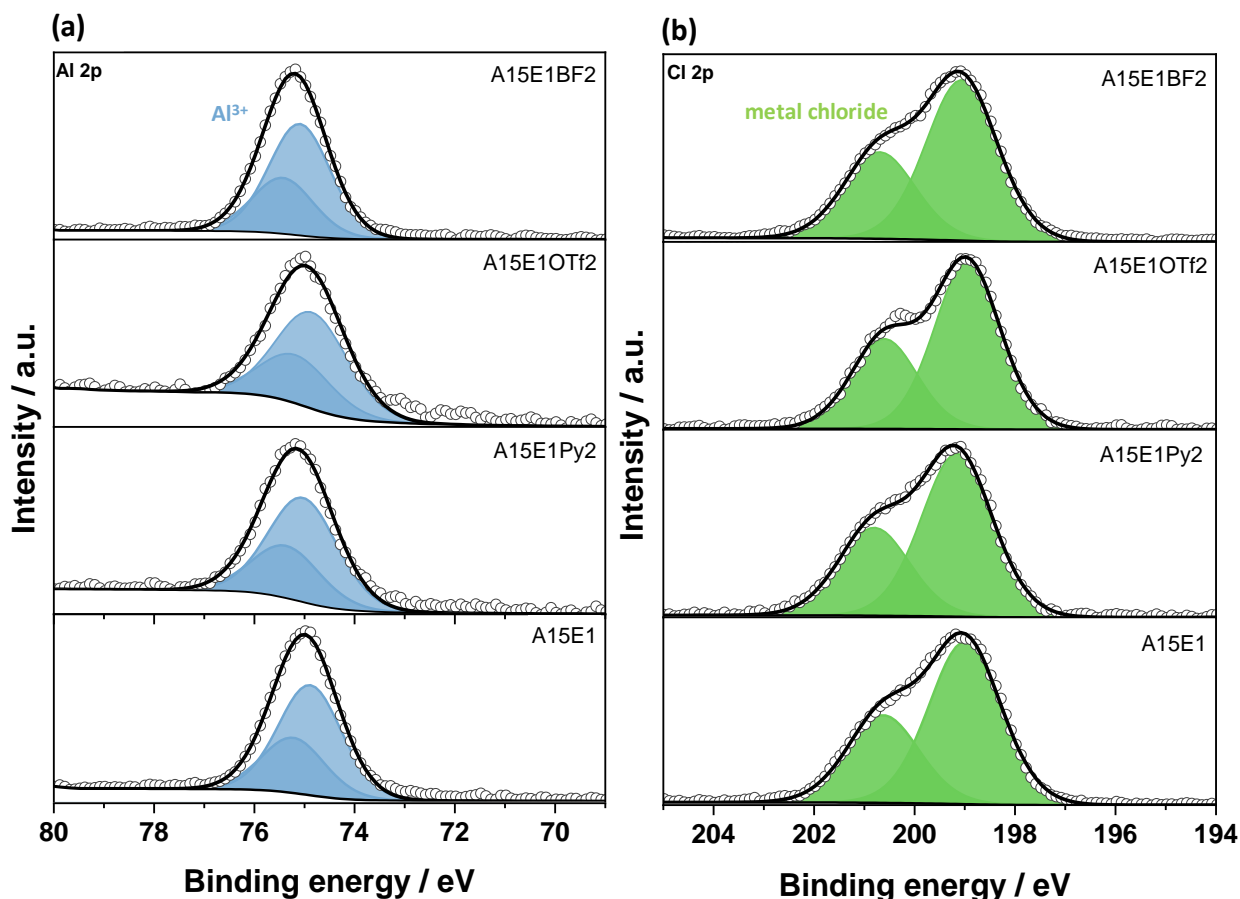
**Figure 21.** F 1s spectra of AISI 316L samples immersion only in A15E1OTf2 and A15E1BF2.

In the case of A15E1OTf2, only a small amount of organic fluoride (C-F bond) is detected on the AISI 316L sample solely immersed in the A15E1OTf2 electrolyte. This can be related to the OTf ( $\text{CF}_3\text{SO}_3^-$ ) anion on the surface which could be adsorbed or remained as the residue of the electrolyte. However, such a small amount of organic fluoride suggests that the F did not bond strongly to the surface of AISI 316L and was mostly removed after washing the sample.

For A15E1BF2, an increase in the signal at around 685.7 eV in the F 1s spectra for the AISI 316L immersed in the electrolyte can be attributed to inorganic F. This indicates that  $\text{BF}_4^-$  anions are most likely adsorbed on the surface and not decomposed.

Figure 22 (a) and (b) illustrate the Al 2p and Cl 2p spectra for AISI 316L samples immersed in different electrolytes, respectively. Across all samples, Al 2p displays a single doublet peak with minimal discernible variation in the binding energy at 74.7 eV for Al  $2p_{3/2}$ . The binding energies of Al 2p for  $\text{Al}_2\text{O}_3$  and  $\text{AlCl}_3$  are quite close<sup>143–146</sup>, making it difficult to distinguish between these compounds, but the presence of the Al ion on the surface can be evident.





**Figure 22.** Al 2p (a) and Cl 2p (b) spectra of AISI 316L samples immersed in different electrolytes

In the Cl 2p spectra, a single doublet could be accurately fitted for all the AISI 316L samples immersed in the electrolytes, both with and without inhibitors. This Cl 2p<sub>3/2</sub> peak is located at around 199 eV, which can be correlated to metal chloride, likely in the form of FeCl<sub>x</sub> or a

In summary, AISI 316L undergoes corrosion when exposed to electrolytes, even during immersion alone, leading to the formation of iron chloride. However, the application of inhibitors can slightly decrease this corrosion. The best reduction in corrosion is observed for the AISI 316L sample immersed in A15E1OTf2, while the worst case is seen in A15E1BF2 among inhibitor-containing electrolytes.

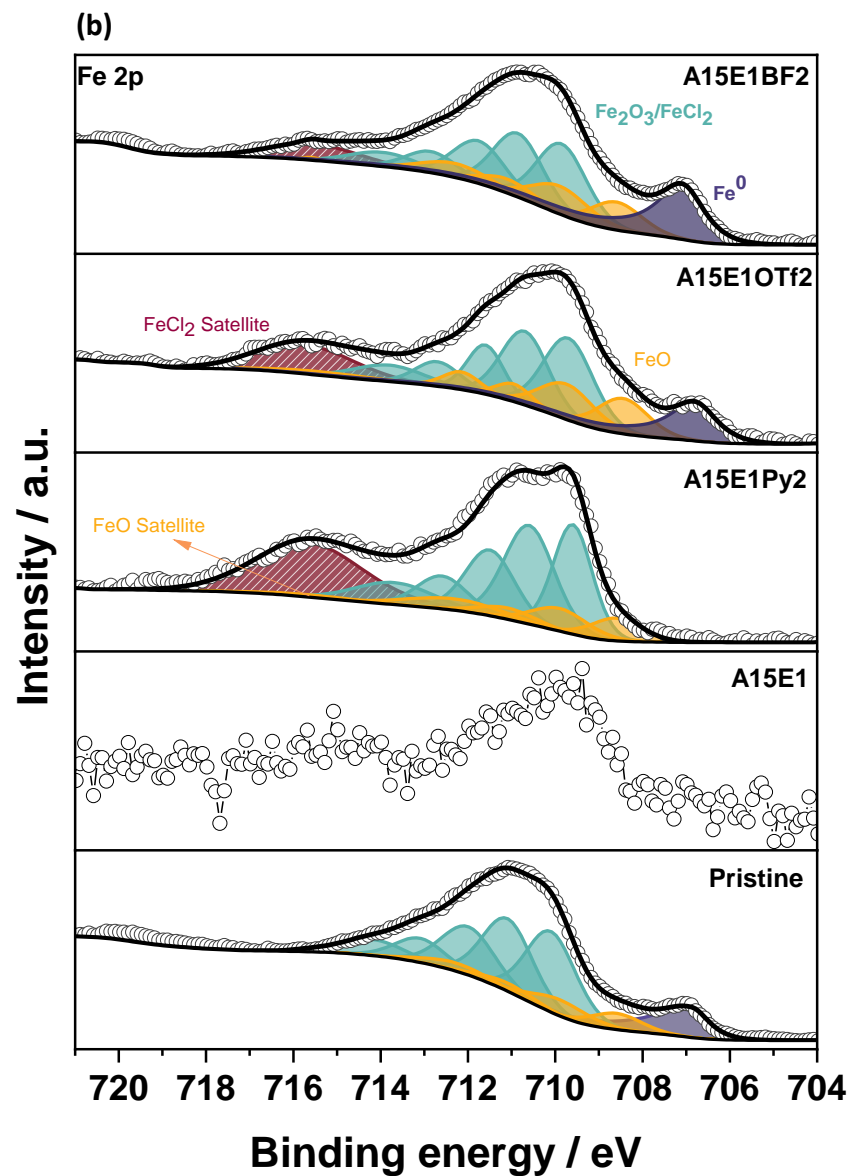
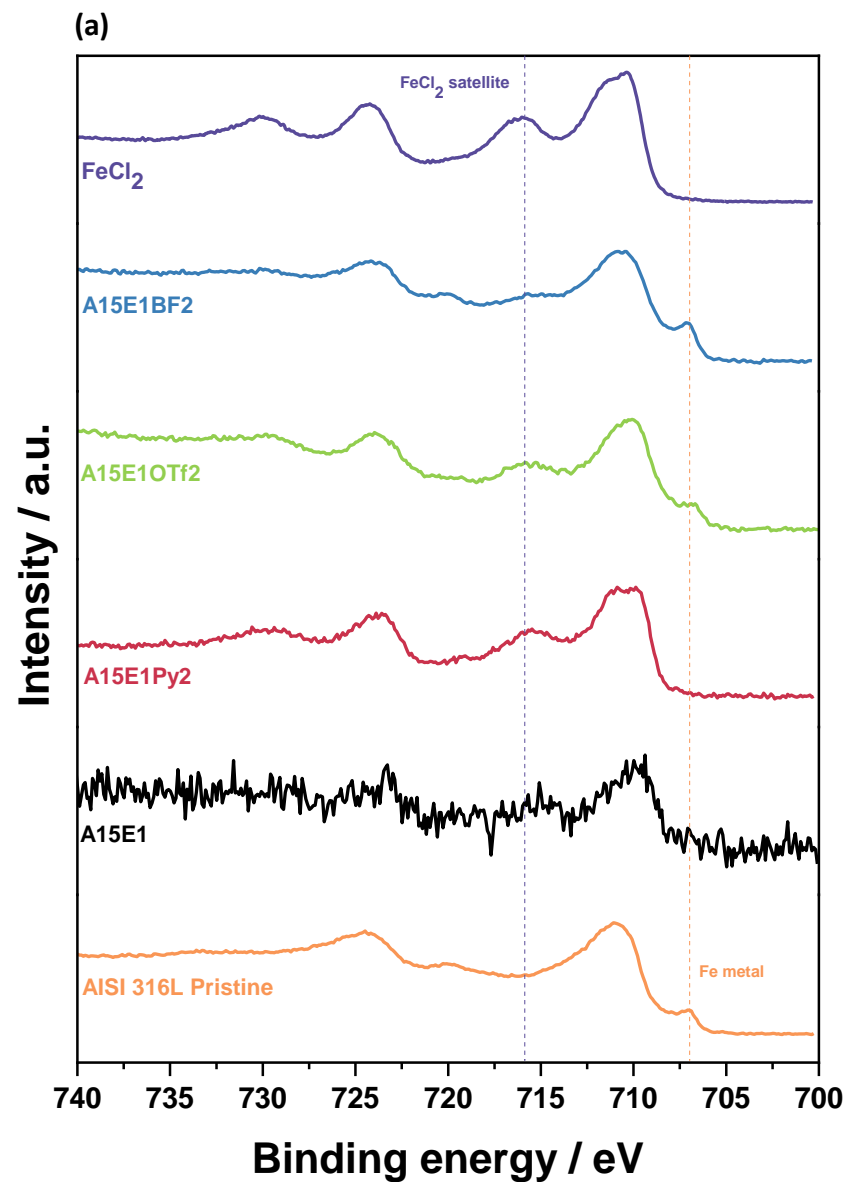
#### 5.1.2.2 XPS results of polarized AISI 316 in the electrolyte-containing inhibitors

To understand the corrosion behavior of AISI 316L under high potential conditions, the XPS results of the AISI 316L samples polarized at 1.5 V vs. Al for 1 minute were evaluated. This evaluation followed the same procedures described in chapter 5.1.2.1 on Fe 2p spectra fitting and the assessment of AISI 316L samples immersed in electrolytes. Specifically, the general

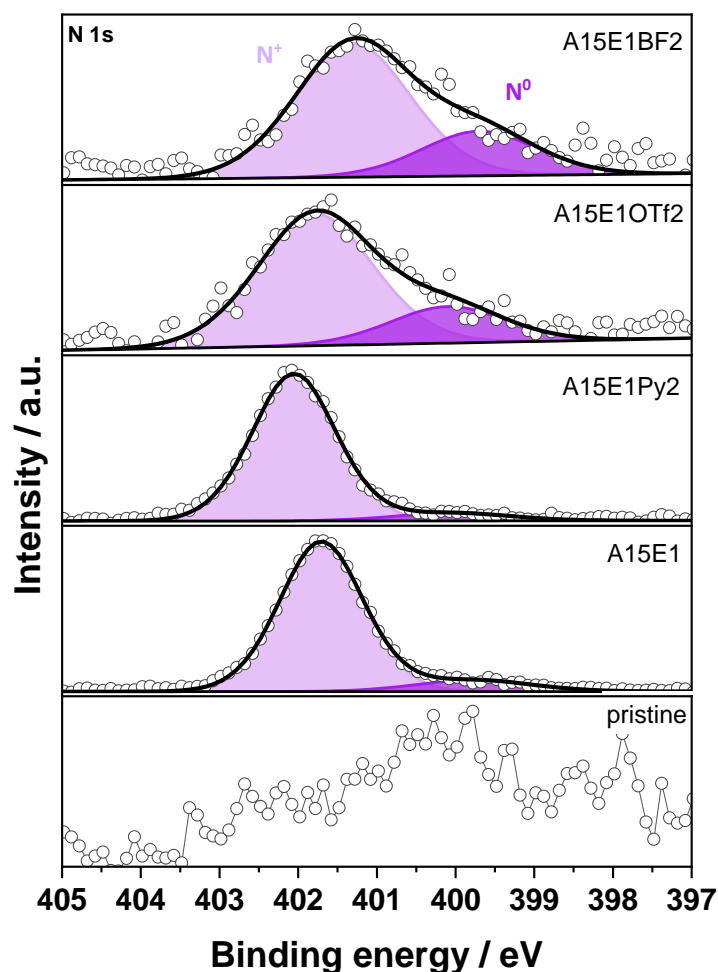
shape of the Fe spectra was compared with that of the pristine AISI 316L foil and FeCl<sub>2</sub> of various samples, as depicted in Figure 23 (a). Additionally, the Fe spectra of the samples were fitted, and peaks associated with metallic iron and the satellite peaks related to FeCl<sub>2</sub>, a primary indicator of corrosion, were compared.

By comparing the Fe 2p spectra of AISI 316L samples polarized in A15E1 electrolytes with and without inhibitors to the AISI 316L pristine and FeCl<sub>2</sub> spectra, as illustrated in Figures 23 (a) and (b), the following observations were made:

1. **Samples polarized in A15E1:** The Fe 2p spectra for these samples have a low signal-to-noise ratio, indicating the surface is likely covered by a mixture of electrolyte, electrolyte decomposition products, and corrosion products. This makes interpreting the surface components or fitting the spectra challenging. This observation correlates with the higher current observed for AISI 316L polarized in A15E1 (Figure 16), which might increase surface roughness and lead to the trapping of electrolyte residues even after washing. However, the shape of the spectra is more similar to FeCl<sub>2</sub> than pristine AISI 316L, as evidenced by an increase in the signal near the FeCl<sub>2</sub> satellite peak.
2. **Sample polarized in A15E1Py2:** The Fe 2p<sub>3/2</sub> peak related to Fe metal is not visible. Instead, the surface of this sample is most likely covered by iron chlorides, as the shape of the graph closely resembles the FeCl<sub>2</sub> spectra, with a prominent FeCl<sub>2</sub> satellite peak that is more pronounced compared to the other samples.
3. **Samples polarized in A15E1OTf2 and A15E1BF2:** These samples show a Fe metal peak at around 706.6 eV and a reduced intensity of the FeCl<sub>2</sub> satellite peak. This suggests a lower presence of iron chlorides on the AISI 316L surface. Although FeCl<sub>2</sub> is still formed, the presence of EMImOTf and EMImBF<sub>4</sub> inhibitors appears to mitigate the corrosion of AISI 316L in these electrolytes



**Figure 23.** Fe 2p spectra for AISI 316L samples polarized at 1.5 V vs. Al for 1 minute (a) Full spectra comparing the shapes with AISI 316L pristine foil and FeCl<sub>2</sub> spectra. (b) Fitted Fe 2p spectra highlighting the Fe metal peak and FeCl<sub>2</sub> satellite peak.



**Figure 24.** N 1s spectra of AISI 316L samples polarized at 1.5 V vs. Al for 1 min in different electrolytes, as well as the AISI 316L pristine foil.

It has been noted that inhibitors adsorb onto the surface through the N atom in the cation. To confirm the presence of these inhibitors on the surface of AISI 316L polarized at 1.5 V vs. Al, N 1s spectra were analyzed, as shown in Figure 24. The N 1s spectra indicate that N content is notably low in the pristine sample. However, in all other samples, a signal at 401.8 eV is evident, attributed to the N<sup>+</sup> in the imidazolium ring (EMIm<sup>+</sup>) originating from the electrolyte. This signal is consistently observed across all samples.

Previous studies have mentioned the potential adsorption of Cl<sup>-</sup> ions onto the surface of AISI 316L in acidic chloride-containing electrolytes, resulting in the formation of (FeCl)<sub>ads</sub><sup>-</sup>.<sup>113</sup> The cationic constituents of the electrolytes, such as EMIm<sup>+</sup> and Py<sup>+</sup> (in the case of A15E1Py2), can subsequently electrostatically adsorb to (FeCl)<sub>ads</sub><sup>-</sup>, leading to the observed peak in the N 1s spectra at 401.8 eV. Additionally, a peak at 400 eV suggests the presence of reduced EMIm and/or Py on the surface, implying the decomposition of EMIm<sup>+</sup> and Py<sup>+</sup> on the surface. These decomposition products, along with the corrosion products, might accumulate on the surface

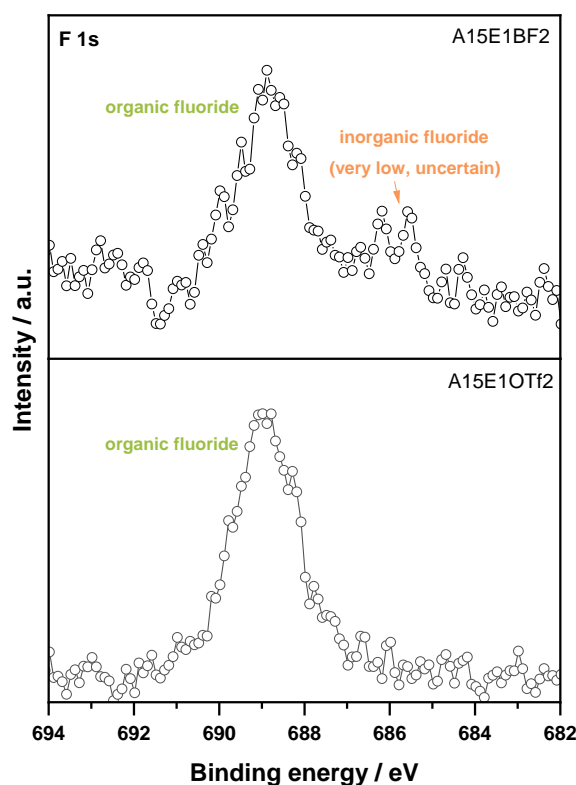
and limit further corrosion by creating a diffusion barrier. This peak is more pronounced in samples exhibiting Fe metal peaks in the Fe spectra, presumed to be less corroded (*e.g.*, A15E1BF2, A15E1OTf2), supporting this assumption.

The presence of OTf<sup>-</sup> and BF<sub>4</sub><sup>-</sup> anions on the AISI 316L surface and whether they have undergone any changes is inspected using the F 1s spectra for AISI 316L in A15E1OTf2 and A15E1BF4, both polarized in these electrolytes, as depicted in Figure 25.

For the AISI 316L sample polarized in A15E1OTf2, an increase in the signal is detectable at 688.8 eV. This can be associated with organic fluoride (C-F bond) which can be correlated to the adsorbed OTf<sup>-</sup> (CF<sub>3</sub>SO<sub>3</sub><sup>-</sup>) anion on the surface.

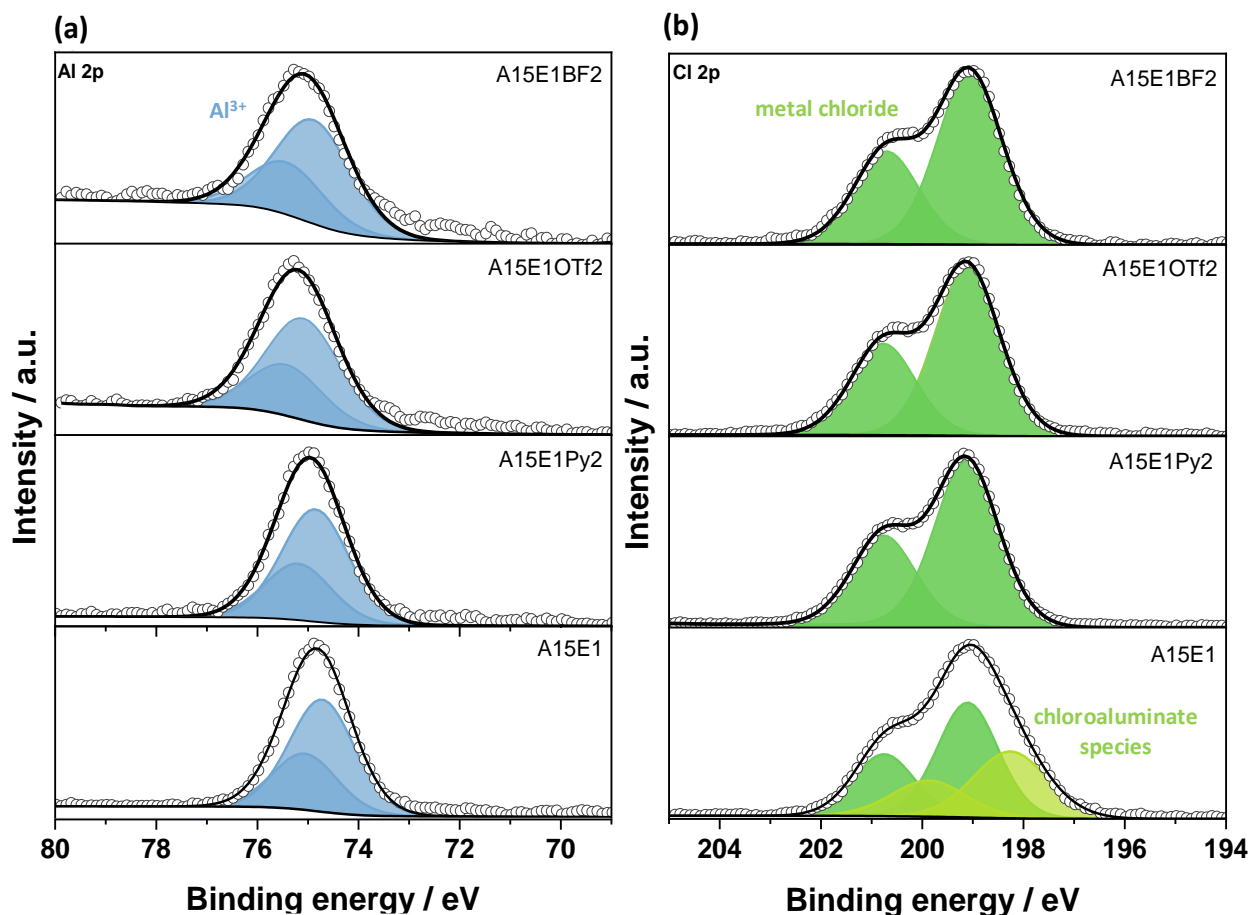
In the case of the AISI 316L sample polarized in A15E1BF4, two peaks are observed. The peak at binding energy at 685.7 eV can be attributed to the inorganic fluoride (presence of BF<sub>4</sub><sup>-</sup> anions), but the poor signal-to-noise ratio introduces uncertainty.<sup>147</sup> The peak at 688.9 eV can be correlated with the formation of organic species (C-F bond), indicating the decomposition of BF<sub>4</sub><sup>-</sup>.<sup>148</sup>

This indicates that both inhibitors are adsorbed onto the surface of AISI 316L when a high potential is applied. This adsorption likely results from the surface of the metal becoming positively charged during polarization, which can attract and adsorb the anions.



**Figure 25.** F 1s spectra of AISI 316L samples polarized at 1.5 V vs. Al for 1 min A15E1OTf2 and A15E1BF2.

Figures 26 (a) and (b) illustrate the Al 2p and Cl 2p spectra for AISI 316L samples polarized in different electrolytes. Across all samples, Al displays a single doublet peak with minimal discernible variation at 74.7 eV for Al 2p<sub>3/2</sub> showing the presence of Al ion on the surface.



**Figure 26.** Al 2p (a) and Cl 2p (b) spectra of AISI 316L samples polarized at 1.5 V vs. Al for 1 min in different electrolytes

The Cl 2p spectra for the samples also show only a doublet in all the samples polarized in the different electrolytes, except for A15E1, which shows two doublets. A metal chloride bond can be observed at around 199 eV for Cl 2p<sub>3/2</sub> which has been assigned to the formation of iron chloride (or a mixture of AlCl<sub>3</sub>/FeCl<sub>y</sub>). It has been also observed that all AISI 316L samples are only immersed in the electrolytes (Figure 22).

Another doublet with Cl 2p<sub>3/2</sub> at 198.5 eV in the Cl 2p spectra can be observed only in the case of AISI 316L polarized in A15E1. Interestingly, the Fe 2p spectra for this sample also exhibit a high noise-to-signal ratio. This may be due to the more heterogeneous surface of AISI 316L as a result of severe corrosion which causes the trapping of the electrolyte on the surface even

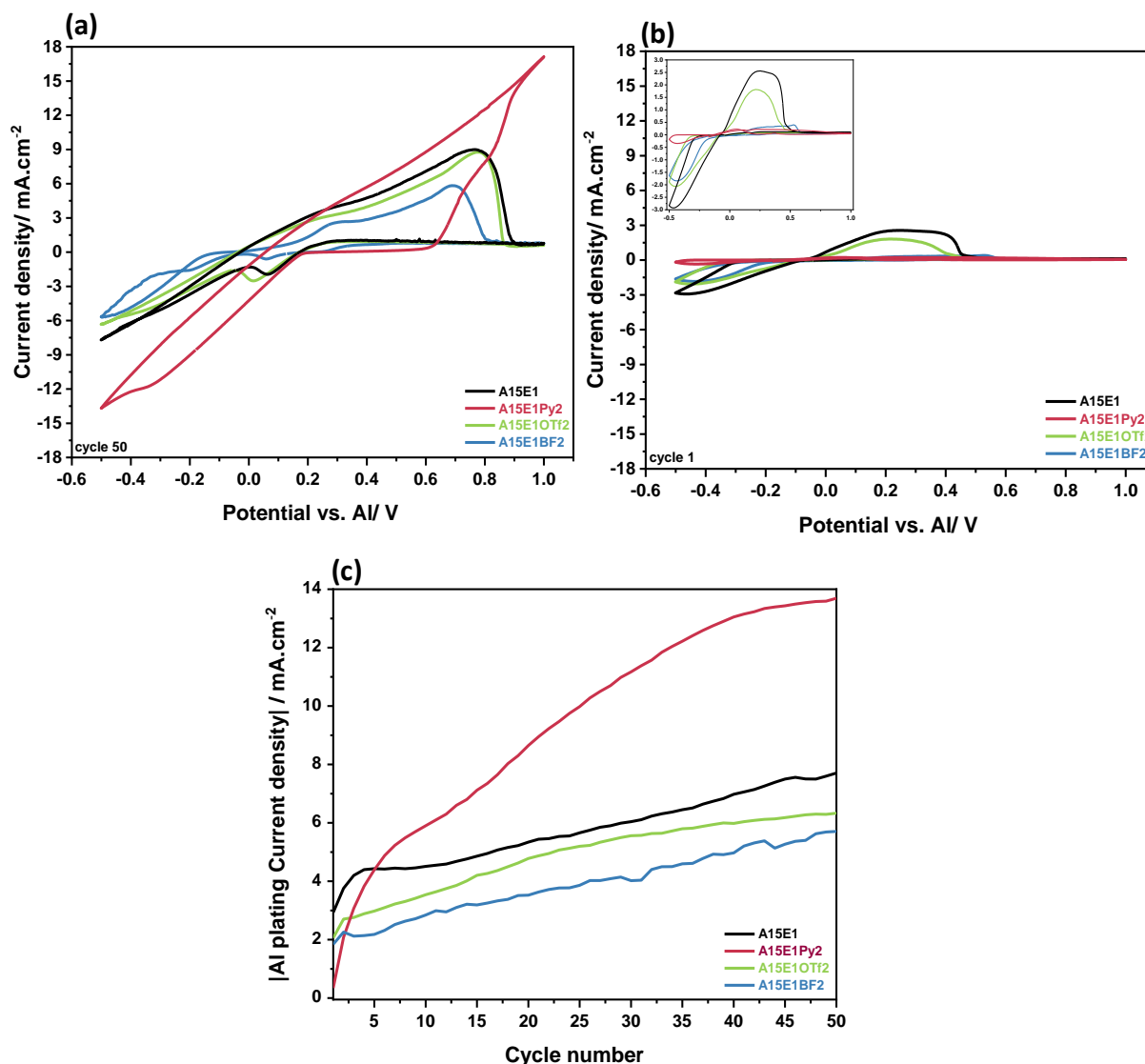
after washing, preventing clear observation of the Fe 2p spectra. Based on this interpretation, it is possible that the doublet observed at 198.5 eV is related to the chloroaluminate species ( $[\text{Al}_2\text{Cl}_7]^-$  and  $[\text{AlCl}_4]^-$ ) from the electrolyte.

In summary, both EMImOTf and EMImBF<sub>4</sub> inhibitors mitigate the corrosion of AISI 316L at high potential to some degree. This mitigation likely occurs due to a combination of factors: adsorption and reduction of the EMIm<sup>+</sup> cation, adsorption of the OTf<sup>-</sup> anion in EMImOTf, and decomposition products of the BF<sub>4</sub><sup>-</sup> anion in EMImBF<sub>4</sub>. However, using these inhibitors raises concerns. While they may address the corrosion of the AISI 316L as a current collector, their adsorption on the metal surfaces could also impact the Al plating and stripping process at the negative electrode. Since Al metal is used as the negative electrode, it is crucial to investigate if these inhibitors adsorb on its surface as well. To address this concern, we conducted further studies on Al plating and stripping behavior in electrolytes containing these inhibitors.

## 5.2 Impact of Inhibitors on Al negative electrode

### 5.2.1 Evaluation of inhibitors impact on Al plating and stripping *via* electrochemical analysis

To investigate the impact of inhibitors on Al plating and stripping behavior, CV measurements, using Al foil as WE, GC as CE, and Al wire as pseudo-reference were conducted. By comparing the Al plating and stripping current densities in electrolytes with and without inhibitors (A15E1, A15E1Py2, A15E1OTf2, A15E1BF2), as displayed in Figure 27 (a) and (b), it becomes evident that the presence of inhibitors affects the Al plating and stripping current density, particularly in the first cycle.



**Figure 27.** CV curves of the Al WE in various electrolytes, with and without inhibitors. The potential window scanned from -0.5 V to 1 V vs. Al at a scan rate of 10 mVs<sup>-1</sup>. A GC CE and an Al wire pseudo-reference electrode were used. The Al WE was cycled 50 times, and the curves for (a) the 1<sup>st</sup> and (b) the 50<sup>th</sup> cycles are shown. (c) the absolute value of the maximum Al plating current density vs. cycle number for various electrolytes.



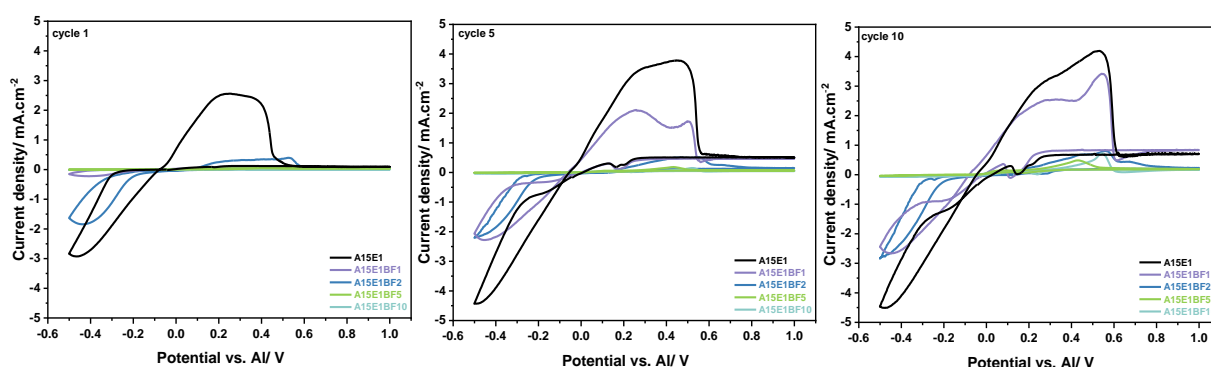
Except for the A15E1OTf2 electrolyte, the addition of inhibitors hinders the Al plating and stripping, with A15EPy2 demonstrating the most significant effect.

Across all samples, regardless of inhibitor presence in the electrolyte, the current density of Al plating and stripping typically increases gradually after several cycles. Figure 27 (c) illustrates an increase in the absolute value of the maximum current density of Al plating in each cycle. Apart from the general increase in the Al plating and stripping current density over the cycling (which can be partly attributed to the removal of the native oxide layer on the Al negative electrode), each inhibitor, affects these processes differently.

As for A15E1OTf2, it appears that the Al plating and stripping are not significantly influenced by the EMImOTf inhibitor compared to the A15E1 electrolyte, neither in the first cycle nor after 50 cycles.

In the A15E1Py2 electrolyte, the Al plating and stripping current density is severely limited in the first cycle. However, by cycle number 50, a higher Al plating and stripping current density can be observed. Although both the stripping and plating potentials shift to positive and negative potentials, respectively. It can be assumed that polarization occurs in this electrolyte.

In the case of A15E1BF2, Al plating and stripping are observed to be limited in the initial cycles, similar to the behavior observed in A15E1Py2. However, the difference in Al plating and stripping current density compared to the A15E1 electrolyte after 50 cycles is not substantial. Nonetheless, lower current densities are still observed for both plating and stripping. The impact of EMImBF<sub>4</sub> inhibitor concentrations on Al plating and stripping behavior was investigated during the initial ten cycles.



**Figure 28.** CV curves of Al WE in various concentrations of the EMImBF<sub>4</sub> inhibitor at cycle numbers 1, 5, and 10. Al was used as the CE and pseudo-reference. The scan rate was 10 mV s<sup>-1</sup>. Concentrations are as follows: A15E1 (no inhibitor), A15E1BF1 (1 wt% inhibitor), A15E1BF2 (2 wt% inhibitor), A15E1BF5 (5 wt% inhibitor), and A15E1BF10 (10 wt% inhibitor). Increasing the inhibitor concentration led to greater limitations in Al plating and stripping.

Notably, increasing the inhibitor concentration generally led to a more pronounced limitation of Al plating and stripping, as observed in Figure 28.

In general, an increase in Al plating and stripping current density after a few cycles is observed in all electrolytes, regardless of the presence of inhibitors. This phenomenon is likely due to less native oxide layer and more active sites on the surface of Al during cycling, along with the adsorption of the EMIm<sup>+</sup> from the electrolyte on the surface in the beginning.

The adsorption of EMIm<sup>+</sup> cations on the Al negative electrode has been previously reported.<sup>128</sup> This phenomenon can exhibit both beneficial and detrimental effects on the Al plating. Due to the negatively charged nature of the Al electrode and the chloroaluminate species in the electrolyte (Al<sub>2</sub>Cl<sub>7</sub><sup>-</sup> and AlCl<sub>4</sub><sup>-</sup>), a two-step adsorption mechanism is possible. Initially, the positively charged EMIm<sup>+</sup> cations could adsorb onto the Al surface due to electrostatic attraction. Subsequently, the negatively charged chloroaluminate species adsorb onto the pre-adsorbed EMIm<sup>+</sup> layer. This two-layered structure would then stack repeatedly, forming the electrical double layers (EDLs), through which electron transfer occurs via tunneling.<sup>128</sup> Nonetheless, the process of Al plating over the adsorbed EMIm<sup>+</sup> layer necessitates extra energy, potentially resulting in a reduced Al plating current density.

### 5.2.2 Surface Characterization of Al Negative Electrode

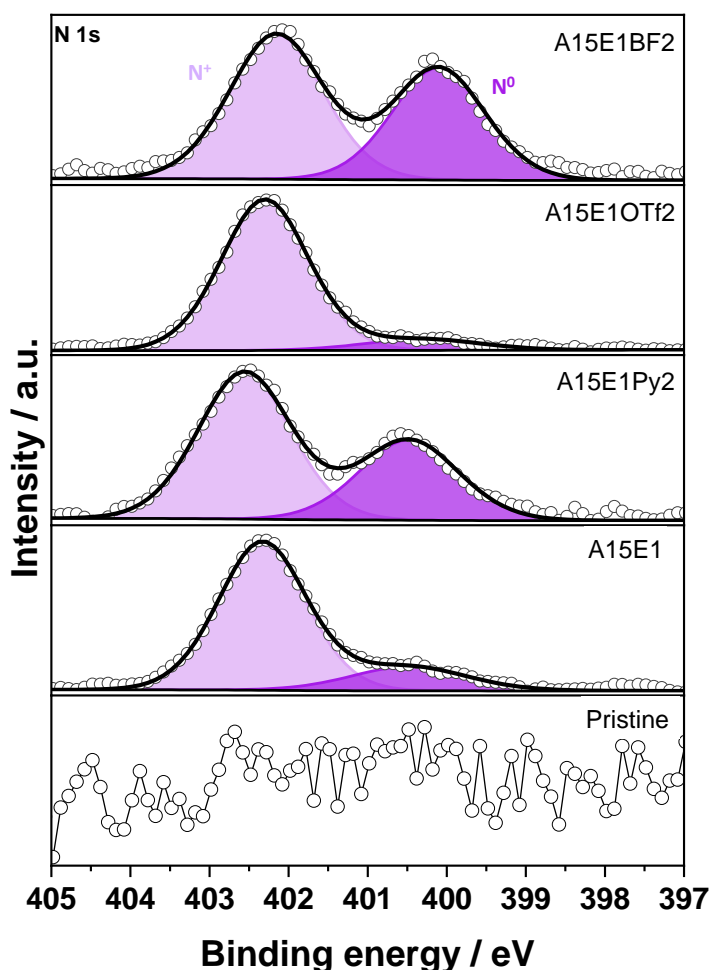
To understand the behavior of these electrolytes, an XPS analysis was conducted. This study aims to compare the surface of Al WE at OCV with Al WE after 50 cycles, to gain insight into the observed increase in Al plating and stripping current density over cycling. Initially, the immersed Al foils were examined to understand the surface of the Al WE at OCV and identify any species that might limit Al plating in the first cycle. Subsequently, the surface of the Al WE was analyzed after 50 CV cycles.

Specifically, the investigation seeks to answer questions such as: Are there any species formed or adsorbed on the surface? If so, are these species stable on the surface after cycling, or do they change or completely dissipate? Additionally, the investigation aims to find a correlation between the species on the surface and the observed polarization effects in A15E1Py2, the minimal changes in A15E1OTf2, and the moderate current density limitation in A15E1BF2.

### 5.2.2.1 Al foil immersed in the electrolytes-containing inhibitors: XPS study

The XPS results for Al foil immersed for 10 minutes in the electrolyte, both with and without inhibitors, are presented in the following section. These results aim to explore why Al plating is limited during the initial cycles in CV measurements using electrolytes containing inhibitors. The immersion time is chosen to approximate the duration of the Al WE in contact with the electrolytes before CV measurements commence.

To explore the presence of the EMIm<sup>+</sup> from electrolyte/inhibitor on the surface, the N 1s spectra were considered. Figure 29 displays the N spectra of Al foil immersed in electrolytes with different inhibitors. A peak around 402 eV corresponds to N<sup>+</sup> in the imidazolium ring, indicating the adsorption of EMIm<sup>+</sup> as a cation. Additionally, a peak at 400 eV suggests neutral N originating from reduced EMIm (and/or Py in A15E1Py2) on the surface.<sup>98</sup>

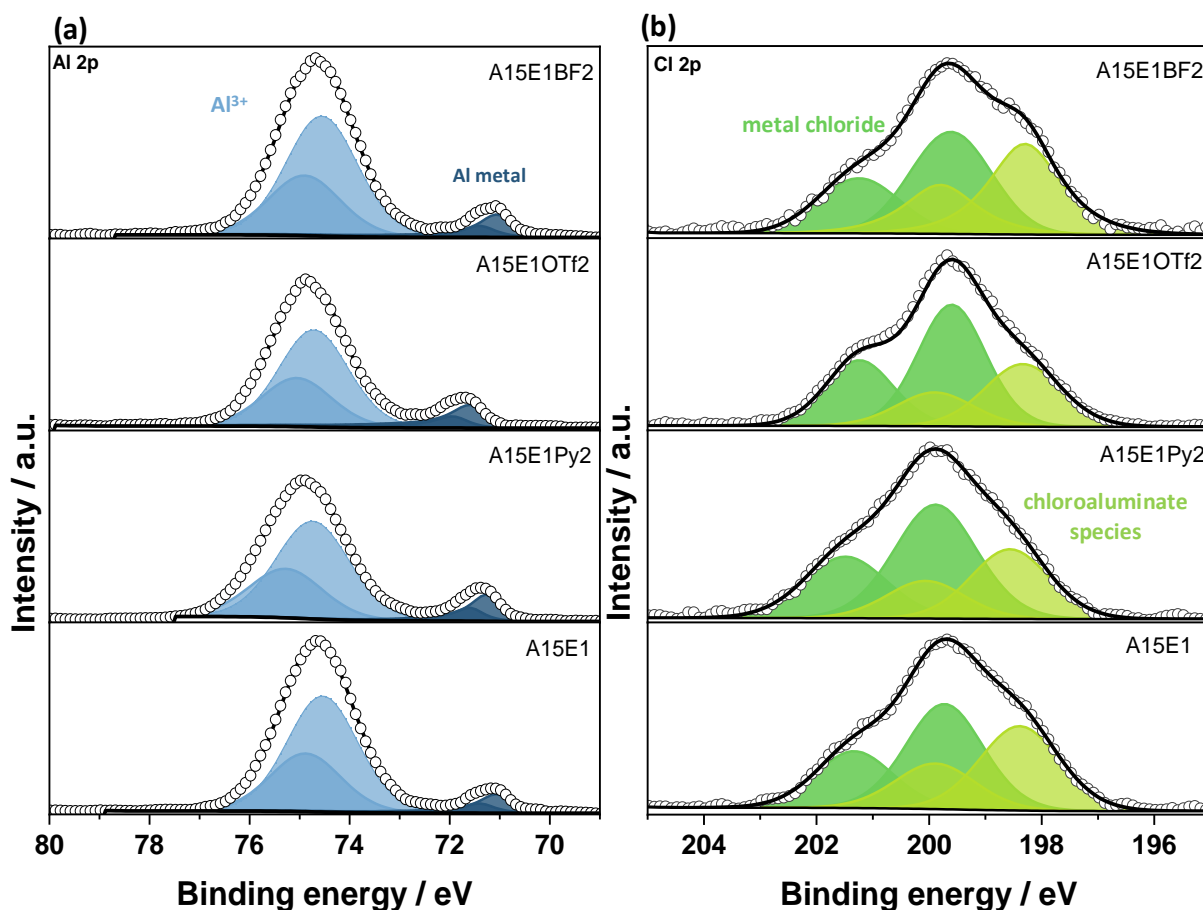


**Figure 29.** N 1s spectra of Al samples immersion in different electrolytes, the N cation can come from EMIm<sup>+</sup> cation and N neutral from the reduced EMIm.

Notably, the N 1s peak at 400 eV is relatively higher, with respect to the peak at 402 eV, for A15E1Py2 and A15E1BF2 compared to A15E1 and A15E1OTf2. This observation, combined with CV measurements, suggests that the presence of reduced EMIm (and/or Py in A15E1Py2) on the surface may be a reason for the greater limitation of Al plating during the first cycle in A15E1Py2 and A15E1BF2 electrolytes.

Particularly, if the reduced cations (EMIm and Py) on the surface are the reason for the limitation of Al plating in the first cycle, similar adsorption could also occur on the surface of the Al wire used as a pseudo-reference electrode. Unlike the working electrode, the reference electrode does not experience potential changes during CV. This could allow for a gradual accumulation of inhibitor molecules on the surface of the Al pseudo-reference over time. This accumulation might explain the observed potential shift in CV measurements after a few cycles. Because in A15E1Py2, both EMIm<sup>+</sup> and Py<sup>+</sup> can adsorb on the Al pseudo-reference, probably with a stronger bond from Py<sup>+</sup>, a more severe potential shift in the CV can be observed with A15E1Py2 (Figure 27). The stronger adsorption of Py<sup>+</sup> might be due to its single ring N and more localized charge which has been stated in earlier research.<sup>122,123</sup> The Al 2p spectra are also investigated to determine the Al species present on the surface and the impact of the inhibitors on them. Figure 30 (a) presents the Al 2p spectra for Al samples immersed in different electrolytes. The Al 2p<sub>3/2</sub> doublet at around the range of 71.5 to 71.8 eV confirmed the presence of metallic Al. Additionally, another doublet appears at around 75 eV, which can be attributed to Al native oxide and/or AlCl<sub>3</sub> on the Al metal. However, distinguishing between Al<sub>2</sub>O<sub>3</sub> and AlCl<sub>3</sub> based on the binding energies of Al 2p<sub>3/2</sub> is challenging, as their values are quite close.<sup>143–146</sup> Therefore, this peak is referred to as Al<sup>3+</sup>, representing both the native oxide on the Al metal and AlCl<sub>3</sub> formed on the surface. In general, there is not much difference in the Al 2p spectra of different Al samples immersed in various electrolytes.

The presence of AlCl<sub>3</sub> is further confirmed by a doublet peak observed in the Cl 2p spectra with a binding energy of Cl 2p<sub>3/2</sub> at around 199.3 eV, which can be associated with metal chloride, as shown in Figure 30 (b). Additionally, another doublet ranging from 198 to 198.3 eV for Cl 2p<sub>3/2</sub> can be observed in the Cl 2p spectra, which can be attributed to the chloroaluminate species ([Al<sub>2</sub>Cl<sub>7</sub>]<sup>-</sup> and [AlCl<sub>4</sub>]<sup>-</sup>) present on the surface. Although some earlier studies have associated this peak with EMImCl,<sup>149,150</sup> it is important to note that due to the strong concentration of the chloroaluminate species, the presence of EMImCl is less probable on the surface.

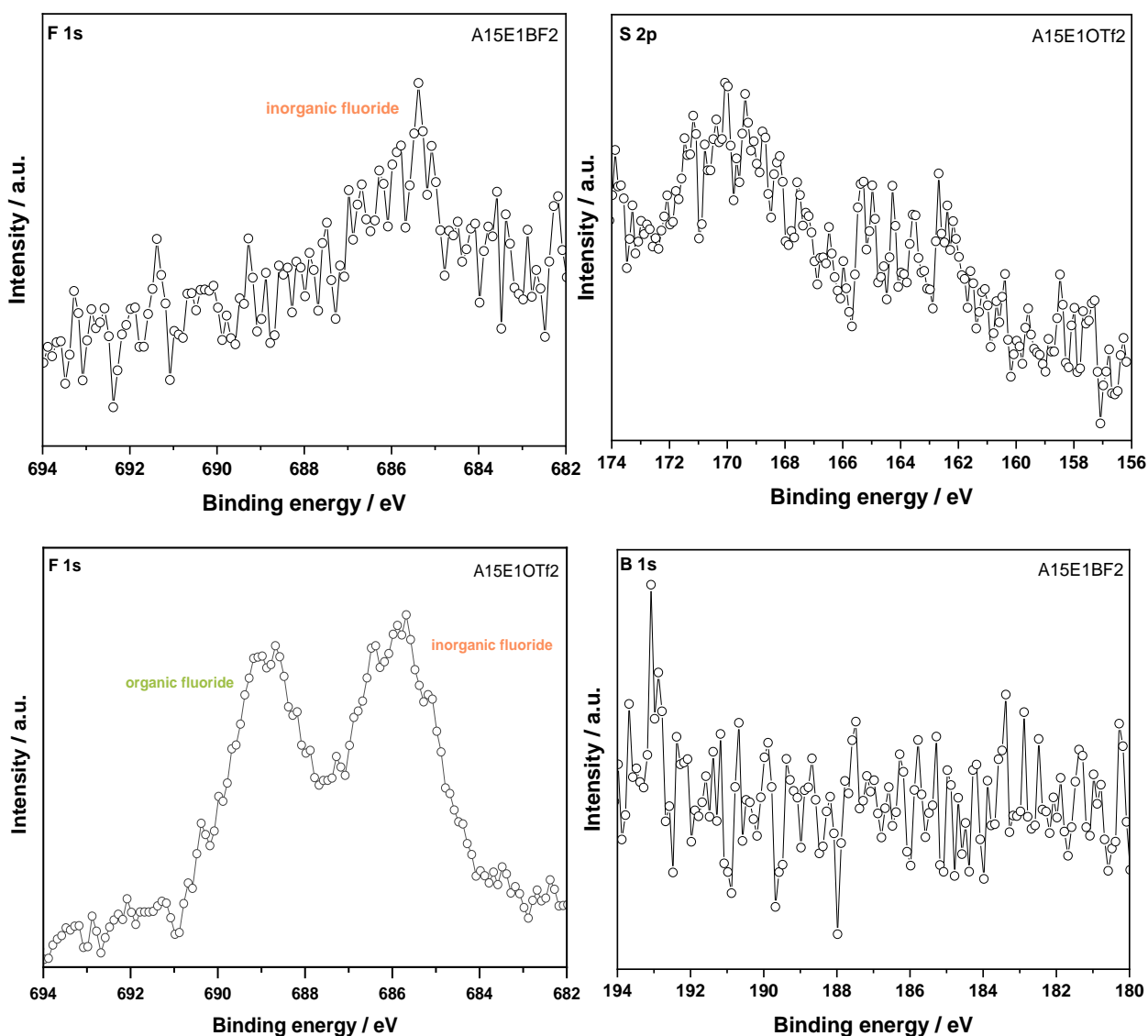


**Figure 30.** Al 2p (a) and Cl 2p (b) spectra of Al samples immersed for 10 minutes in different electrolytes.

The idea behind utilizing different anions,  $\text{BF}_4^-$  and  $\text{OTf}^-$ , in conjunction with the  $\text{EMIm}^+$  cation, instead of  $\text{Cl}^-$ , stemmed from a prior report suggesting that the different electron-donating abilities of the anions not only influence complexes forming on the surface but also enhance the adsorption of the cation and aid in preventing corrosion.<sup>116</sup> However, it is important to investigate the direct impact of the anion itself on Al as well.

The F 1s and S 2p spectra for the  $\text{OTf}^-$  anion and the B 1s and F 1s spectra for  $\text{BF}_4^-$  were examined for both A15E1OTf2 and A15E1BF2 samples and are shown in Figure 31. For the Al sample immersed in A15E1BF2, a scarce amount of F or boron (B)-containing species are found on the Al surface post-washing. Yet, a small increase in the signal at around 685.4 eV is still observed, indicating the presence of  $\text{BF}_4^-$ . Regarding B 1s spectra, no increase in the related signal can be observed. This may be due to the low amount of  $\text{BF}_4^-$  along with the lower atomic sensitivity factor of B compared to F (0.16 for the B/F ratio) and only one B atom as opposed to four F atoms in the  $\text{BF}_4^-$ .<sup>151</sup>

When the Al sample is immersed in A15E1OTf2, the F 1s spectrum reveals two distinct peaks around 685.9 and 688.9 eV, which can be attributed to inorganic fluoride and organic fluoride, respectively. These peaks likely indicate the adsorption and decomposition of OTf. However, the decomposition of OTf does not significantly hinder Al plating in the A15E1OTf2 electrolyte, as previously observed in CV measurements. In the S 2p spectrum, an increase in the signal around 169.5 eV can also be associated with OTf. This low signal-to-noise ratio for sulfur (S) can be anticipated due to its lower atomic sensitivity factor compared to fluorine, which is 0.66 for the S/F ratio,<sup>151</sup> as well as considering the stoichiometric ratio of S to F in OTf, where each OTf<sup>-</sup> anion contains three F atoms and only one S atom. It is worth noting that although inorganic fluorine can include AlF<sub>3</sub>, no AlF<sub>3</sub>-related peak is observed in the Al 2p spectra. This suggests that OTf likely does not form AlF<sub>3</sub>.



**Figure 31.** F 1s and B 1s of Al immersed in A15E1BF2 electrolyte and F1s and S 2p spectra of Al immersed in A15E1OTf2 electrolyte.

While ex-situ XPS measurements coupled with sample washing might overlook unstable surface species formed on the surface, they still suggest limitations in Al plating due to the adsorption of reduced EMIm<sup>+</sup> and Py<sup>+</sup> cations, in the first cycle. These findings suggest that EMImBF<sub>4</sub> and Py<sub>1.4</sub>Cl, adsorb stronger on the Al surface, but restrict initial Al plating compared to the A15E1 electrolyte (as seen in the initial cycle of the CV measurement).

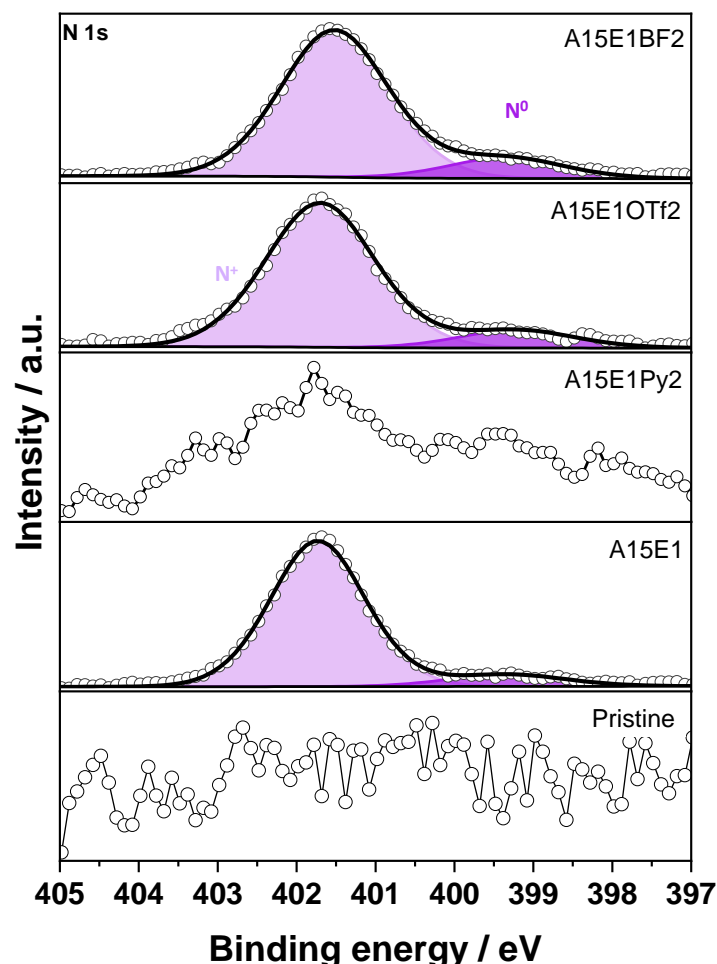
While EMImOTf adsorption on AISI 316L (discussed in chapter 5.1) and the presence of OTf near the surface appear to inhibit Cl<sup>-</sup> adsorption and mitigate corrosion, this effect is not observed in the case of Al surfaces. This suggests a potential advantage for the EMImOTf inhibitor. While it mitigates corrosion of the AISI 316L current collector, it appears to have minimal impact on the Al plating and stripping process at the negative electrode. This could be beneficial for real Al battery cells, where both the current collector and the Al negative electrode are presented.

#### **5.2.2.2 Al foil cycled in the electrolytes-containing inhibitors: XPS study**

By examining the samples immersed in electrolytes with and without inhibitors, we aimed to determine if the surface of the Al foil changes upon contact with the electrolyte. Understanding these changes could help explain why the plating and stripping current density is limited when inhibitors are introduced into the electrolyte. However, as observed in the CV measurements, this limitation on Al plating and stripping diminishes by cycle 50. In this section, with the help of XPS, we aim to identify what changes occur on the Al surface after cycling, especially in the electrolytes with Py<sub>1.4</sub>Cl and EMImBF<sub>4</sub>, where Al plating and stripping current densities are changing significantly during 50 cycles, as shown in the CV measurements.

N 1s spectra of the Al foil cycled 50 times in the electrolytes were first evaluated to observe if peaks related to EMIm<sup>+</sup> (and Py<sup>+</sup> in the case of A15E1Py2) and their reduced forms are present on the surface after 50 cycles. Figure 32 shows the N 1s spectra of Al cycled in the electrolyte. It is noticeable that both peaks at 400 eV and 402 eV, correlated to neutral N from the reduced EMIm and the positively charged N from EMIm<sup>+</sup>, respectively, can be observed for Al samples cycled in the electrolyte, except for the sample cycled in A15E1Py2.

Although the Al sample immersed in this electrolyte exhibits the highest ratio of reduced EMIm/Py observed among the inhibitors (with the lowest Al plating and stripping current density in the initial cycle), after cycling, a very small amount of N is presented on the surface.



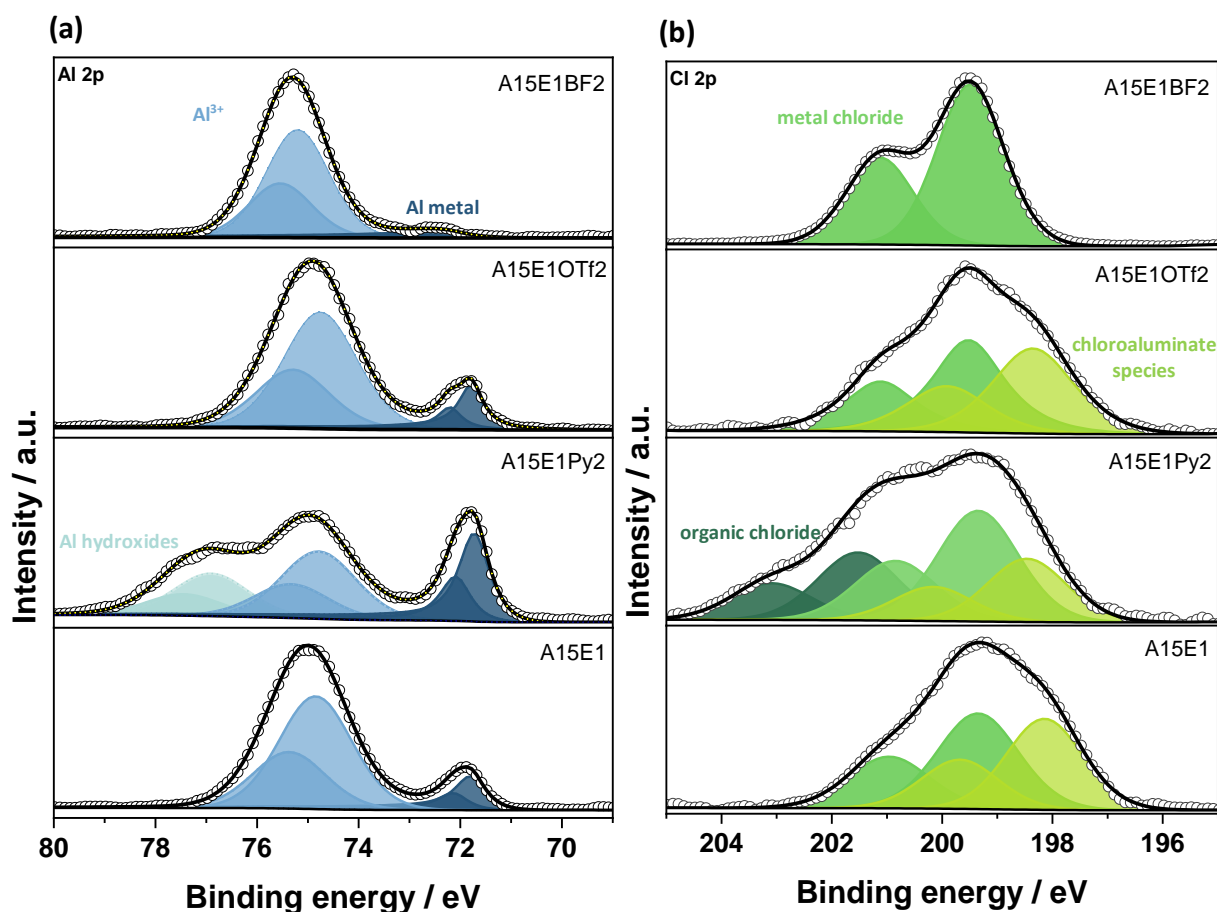
**Figure 32.** N 1s spectra of Al samples after 50 cycles in different electrolytes, the N cation can come from EMIm<sup>+</sup> cation and N neutral from the reduced EMIm. Al foil, GC disc, and Al wire were used as WE, CE, and pseudo-reference electrodes, respectively. The potential window scanned from -0.5 V vs. Al reference electrode to 1 V vs. Al pseudo-reference electrode at a scan rate of 10 mV s<sup>-1</sup>.

Apart from the Al sample cycled in A15E1Py2, for all other cycled samples, the peak at 400 eV decreases in respect to the peak at 402 eV. This suggests that in the cycled samples, the reduced EMIm is not retained on the surface. In other words, if the reduced EMIm (and Py in the case of A15E1Py2 electrolyte) were one of the reasons for Al plating and stripping limitation, the observed improvement in Al plating and stripping after 50 cycles is likely due to the less availability of the reduced species on the surface. A higher amount of reduced EMIm can be seen in the case of the A15E1BF2 electrolyte, which also shows lower plating and stripping current in cycle 50 compared to the A15E1, although the differences are minimal at this stage.

The Al 2p spectra of the cycled Al surface reveal the species present and the impact of inhibitors after 50 cycles, as shown in Figure 33 (a). The metallic Al appears as an Al 2p<sub>3/2</sub>



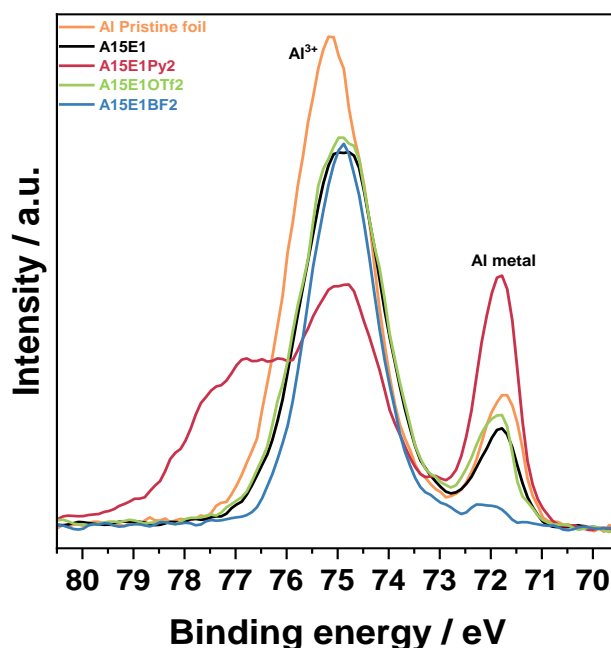
doublet in the range of 71.5 to 71.8 eV. A second doublet at around 75 eV, designated as  $\text{Al}^{3+}$ , reflects a combination of native Al oxide ( $\text{Al}_2\text{O}_3$ ) and  $\text{AlCl}_3$  formed during cycling and electrolyte interaction. The peaks related to  $\text{Al}^{3+}$  remain almost unchanged across all samples, while the intensity of the metallic Al varies with different electrolytes.



**Figure 33.** Al 2p (a) and Cl 2p (b) spectra of Al samples after 50 cycles in different electrolytes. Al foil, GC disc, and Al wire were used as WE, CE, and pseudo-Reference electrodes, respectively. The potential window scanned from -0.5 V to 1 V vs. Al at a scan rate of  $10 \text{ mV s}^{-1}$ .

The Al metal peak in A15E1OTf2 experienced the least changes compared to A15E1, but in A15E1BF2, a less intense metallic peak is observed, suggesting that the surface is likely covered with  $\text{Al}_2\text{O}_3$  and/or  $\text{AlCl}_3$  species. The presence of less metallic Al on the surface could explain the limited current observed in cycle 50 for Al cycled in A15E1BF2 compared to A15E1. Moreover, it appears that adding inhibitors to the electrolyte does not alter the Al-related species, and the presence of  $\text{BF}_4^-$  and  $\text{OTf}^-$  anions in the electrolyte does not lead to the formation of  $\text{AlF}_3$  on the surface.

In the A15E1Py2 electrolyte, the peak related to the metallic Al is more intense as compared with A15E1. The higher Al plating and stripping current observed in cycle 50 of the CV measurement, can be related to the more Al metal available on the surface, which could be influenced by the polarization effect. Figure 34 compares the intensity of Al 2p spectra for all cycled samples in the different electrolytes. It highlights the changes in the metallic Al ratio across the electrolytes without normalization, focusing more on the relative intensities.



**Figure 34.** A comparison of intensities of Al 2p spectra of Al cycled in the electrolyte containing inhibitors and the Al pristine foil.

Moreover, the XPS of Al cycled in A15E1Py2 reveals an additional doublet at 76.9 eV, suggesting the presence of Al hydroxides. These hydroxides could have formed from residual water adsorbed by the  $\text{Py}_{1.4}\text{Cl}$  inhibitor during Al plating. Furthermore, the presence of an additional peak at 201.5 eV for Cl 2p<sub>3/2</sub> suggests organic chloride species, possibly arising from the inhibitor decomposition during cycling. These findings question the stability of  $\text{Py}_{1.4}\text{Cl}$  within the applied potential window. The observed potential shift in CV measurements (Figure 27) might have additionally contributed to this instability.

The presence of  $\text{AlCl}_3$  on the analyzed surface is further corroborated by the Cl 2p spectra in Figure 33 (b). A characteristic metal chloride doublet peak is observed at a binding energy of approximately 199.3 eV, corresponding to Cl 2p<sub>3/2</sub> for metal chloride ( $\text{AlCl}_3$ ). An additional doublet appears in the Cl 2p spectra, ranging from 198.1 to 198.4 eV for Cl 2p<sub>3/2</sub>. This peak

can be attributed to the presence of the chloroaluminate species ( $[\text{Al}_2\text{Cl}_7]^-$  and  $[\text{AlCl}_4]^-$ ), as a sign of electrolyte remained on the surface.

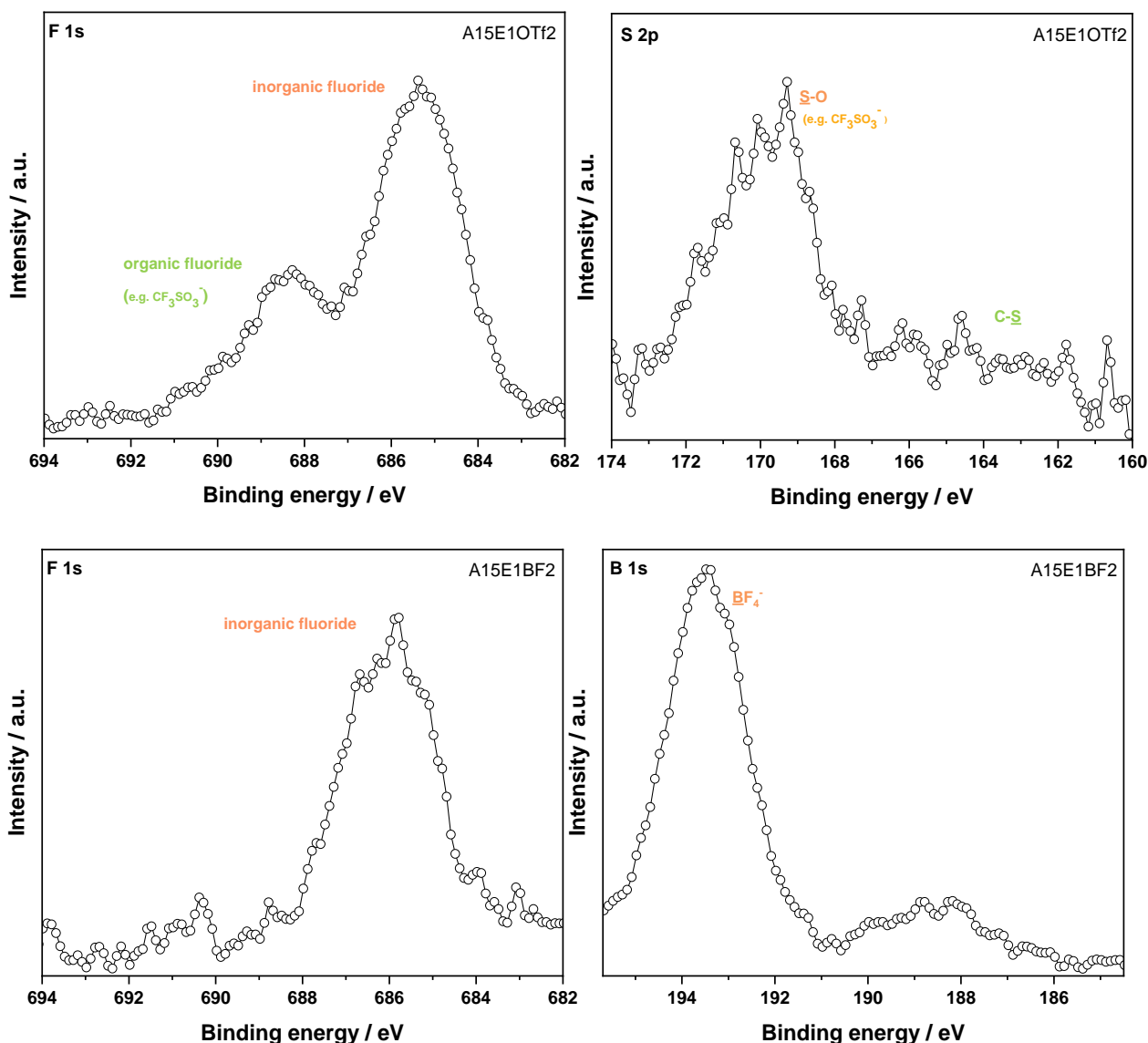
The Cl 2p doublet associated with electrolyte species ( $[\text{Al}_2\text{Cl}_7]^-$  and  $[\text{AlCl}_4]^-$ ) is absent in the case of Al cycled with A15E1BF2 (as evident from Figure 33 (b)). It is noteworthy that similarly only one Cl doublet is also found in the AISI 316L samples. A potential explanation for this discrepancy could be a lower amount of electrolyte remaining on the surface after cycling and washing these samples. This suggests that the absence of the electrolyte species peak might not be solely dependent on the electrolyte composition but on the initial state of the surface as well.

The effect of the  $\text{BF}_4^-$  and  $\text{OTf}^-$  were also evaluated after 50 cycles. The B 1s and F 1s spectra for  $\text{BF}_4^-$  and the F 1s and S 2p spectra for the  $\text{OTf}^-$  anion are shown for Al cycled in A15E1OTf2 and A15E1BF2, respectively.

The F 1s and B 1s spectra shown in Figure 35 for the Al sample cycled in A15E1BF2 exhibit increased signals at approximately 686 eV and 193.4 eV, respectively. These increases are correlated with the presence of  $\text{BF}_4^-$ ,<sup>147,152</sup> indicating that the inhibitor is adsorbed on the surface during cycling. This adsorption may also be associated with the lower current density observed for Al plating and stripping in this electrolyte compared to A15E1, although the effect is not significant.

The F 1s and S 2p spectra exhibit an increase in the signal at 688.7 eV and 168.7 eV, respectively. These can be attributed to the presence of  $\text{OTf}^-$  ( $\text{CF}_3\text{SO}_3^-$ ), indicating that traces of the anion remain on the surface.<sup>153,154</sup> Additionally, the smaller increase in the signal around 686 eV and 163.7 eV suggests the presence of inorganic fluoride and the C-S bond, respectively. This can be linked to the decomposition of  $\text{OTf}^-$ .<sup>153</sup> After cycling, a higher proportion of inorganic fluoride compared to organic fluoride can be observed. This is evident when comparing the F 1s spectra for Al immersed in A15E1OTf2 electrolyte (as shown in Figure 35). It appears that the decomposition of  $\text{OTf}^-$  continues to occur on the surface of Al during cycling. However, as noted in the sample that was only immersed in the electrolyte, this decomposition product does not seem to limit Al plating and stripping.

Despite the XPS analysis suggesting the presence of inorganic fluoride on the cycled Al surface in both A15E1OTf2 and A15E1BF2 electrolytes (Figure 35),  $\text{AlF}_3$  is unlikely to be the primary source. While the observed fluoride could potentially be  $\text{AlF}_3$ , the expected binding energy of  $\text{AlF}_3$  is around 76 eV, which is higher than the peaks observed in Al 2p spectra.<sup>153</sup>



**Figure 35.** F 1s and B 1s of Al cycled for 50 times in A15E1BF2 electrolyte and F 1s and S 2p spectra of Al cycled for 50 times in the A15E1OTf2 electrolyte. Al foil, GC disc, and Al wire were used as WE, CE, and pseudo-reference electrodes, respectively. The potential window scanned from -0.5 V vs. Al to 1 V vs. Al at a scan rate of  $10 \text{ mV s}^{-1}$ .

### 5.3 The key findings of this chapter

Although AISI 316L is renowned for its excellent corrosion resistance, it experiences corrosion when exposed to the A15E1 electrolyte, forming iron chloride even during immersion. This corrosion becomes more severe at high potentials, which raises concerns about the suitability of AISI 316L as a current collector.<sup>42</sup>

The application of the inhibitors—Py<sub>1.4</sub>Cl, EMImOTf, and EMImBF<sub>4</sub>— reduces corrosion under OCV conditions. The EMImOTf additive seems the most effective one while A15E1BF<sub>2</sub> is the most unreliable, based on potentiodynamic polarization.

XPS results supported these findings showing the higher Fe metal peaks and lower FeCl<sub>2</sub> satellite peaks in the Fe 2p spectra of AISI 316L immersed in A15E1OTf<sub>2</sub>. This reduction is likely due to the adsorption and reduction of the EMIm<sup>+</sup> cation on the AISI 316L surface. The OTf<sup>-</sup> anion might hinder Cl<sup>-</sup> adsorption by repelling Cl<sup>-</sup> ions with its bulky structure and negative charge. Although the BF<sub>4</sub><sup>-</sup> anion also adsorbs during immersion, as indicated by F spectra, it seems less effective in repelling Cl<sup>-</sup>, and it cannot form a stable protective layer.

At high potential, both EMImOTf and EMImBF<sub>4</sub> inhibitors mitigate electrolyte aggressiveness to some degree. Identifying the exact complexes formed on AISI 316L with these inhibitors is challenging; however, organic fluoride species observed on the surface indicate the adsorption of OTf<sup>-</sup> and decomposition products of BF<sub>4</sub><sup>-</sup>. The decomposition of the EMImBF<sub>4</sub> inhibitor may explain the higher current density observed for AISI 316L polarized in A15E1BF<sub>2</sub> compared to A15E1 despite less corrosion shown in surface analysis.

Unfortunately, despite the initial adsorption of Py<sup>+</sup> and EMIm<sup>+</sup> mitigating corrosion under immersion conditions in the A15E1Py<sub>2</sub>, this adsorption is not stable enough to prevent AISI 316L corrosion at higher potentials and also because positively charged electrodes tend to attract and interact more strongly with anions, not cations. Even if [FeCl][Py<sub>1.4</sub>]<sub>ads</sub> form, as hypothesized in the literature,<sup>139</sup> it would not be stable.

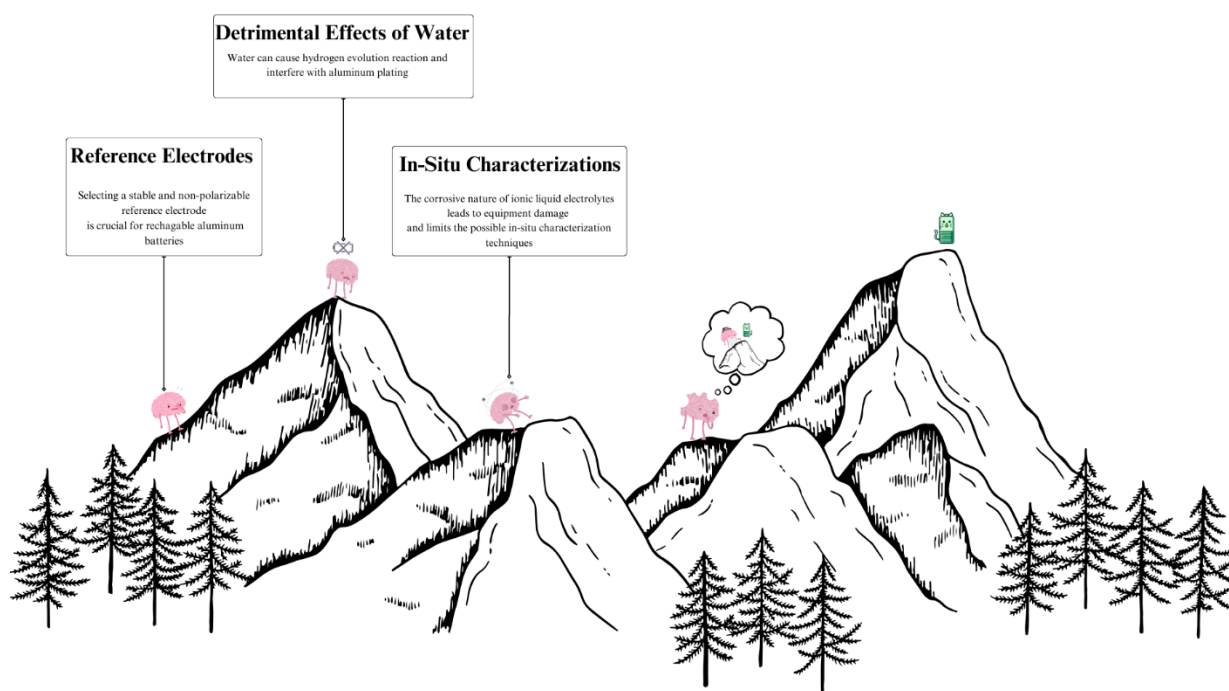
Under the investigated conditions, AISI 316L suffers severe corrosion even with inhibitors applied at a concentration of 2 wt%, rendering it unsuitable as a cost-efficient current collector material for RABs using the chloroaluminate ionic liquid electrolyte (AlCl<sub>3</sub>:EMImCl with molar ratio of 1.5:1).

Moreover, the evaluation of these inhibitors on Al plating and stripping *via* CV reveals a crucial limitation. While an increase in Al plating and stripping current density is observed over

cycling, the initial cycles suffer due to the adsorption of reduced inhibitor cations on the Al surface. This adsorption hinders Al plating, suggesting a trade-off between corrosion protection and plating efficiency. The increase in Al plating and stripping current density after a few cycles is observed in all electrolytes, regardless of the presence of inhibitors. This phenomenon is likely due to the presence of more active sites on the surface of Al during cycling, commonly referred to as activation cycles for Al as well as the presence of less reduced EMIm (and Py in the case of A15E1Py2) on the surface.

## 6 Technical challenges in evaluating RABs

The pursuit of scientific progress is rarely without its hurdles. Research on rechargeable aluminum batteries (RABs) is no exception. A graphical illustration in Figure 36 presents some of the challenges encountered during the present investigation and more detail will be discussed in this chapter. By sharing these obstacles, the author aims to equip the scientific community with valuable foreknowledge, potentially leading to more efficient and streamlined research endeavors on RABs.



**Figure 36.** A graphical illustration highlighting the challenges faced in the research and development of rechargeable aluminum batteries.

### 6.1 Reference electrode challenges in RABs evaluation

Selecting the appropriate reference electrode for non-aqueous systems is a critical decision. The chosen reference should exhibit stability throughout electrochemical measurements, maintaining consistent composition and ideally remaining non-polarizable to ensure a stable potential. Thus, the selection of the reference electrode relies on the experimental conditions, particularly the electrolyte composition.

Conventional reference electrodes like the saturated calomel electrode (SCE) or the Ag/AgCl electrode are designed for stability in aqueous solutions, making them unsuitable for non-aqueous environments. Their performance may suffer from unpredictable behavior or potential

drift, rendering them incompatible with non-aqueous electrolytes commonly used in rechargeable batteries. Consequently, pseudo-reference electrodes have been utilized in research, although they fall short of ideal references due to their irreproducible potentials under specific conditions.

Such challenges arise in Li-ion and Na-ion batteries, where conventional pseudo-reference electrodes like Li and Na metal yield unstable and poorly reproducible potential measurements. Research in the field of Li-ion and Na-ion batteries has focused on addressing these issues by investigating various reference materials including silver (Ag) wire, activated carbon, metal alloy electrodes, and insertion electrode materials to identify the most suitable reference for these systems.<sup>155–157</sup>

In Al-metal batteries utilizing chloroaluminate ionic liquid electrolytes, the use of conventional pseudo-reference electrode materials like Ag or Pt wire is discouraged. These materials are prone to instability in the corrosive electrolytes, leading to corrosion and potential drift. Even when Al wire is used as a pseudo-reference electrode, challenges may arise due to potential issues with the passivation layer on its surface being affected by different electrolytes. This can result in potential calibration difficulties, making it challenging to accurately evaluate and study the electrochemical reaction mechanisms occurring in various electrolytes.

For instance, in our investigation into the effects of inhibitors, we discovered that these inhibitors have the potential to adsorb onto the surface of the Al metal. Consequently, there is a possibility that they could also adsorb onto the surface of the Al pseudo-reference electrode, thereby increasing polarization on its surface and potentially leading to misleading measurements.

In non-aqueous organic electrolytes containing  $\text{Al}(\text{OTf})_3$  and  $\text{Al}(\text{TFSI})$  salts in Al-metal batteries, the water content can significantly impact the reliability of using Al wire as a pseudo-reference electrode. Therefore, more careful investigation and consideration are necessary to identify better alternatives for reference electrodes. The lack of sufficient research in Al-metal batteries exacerbates these challenges and underscores the need for further exploration.

## **6.2 Detrimental effects of water in RABs**

Water can play a detrimental role in RABs due to its influence on the HER and Al plating. The standard reduction potential ( $E^\circ$ ) for HER ( $\approx 0 \text{ V vs. SHE}$ ) is more favorable compared to Al



reduction ( $\approx -1.66$  V vs. SHE) under standard conditions.<sup>133</sup> But, this thermodynamic driving force can promote HER over Al plating even in non-standard conditions as well.

Although the HER might be considered a side reaction, it poses problems, including gas generation inside the cell package, and causes safety issues. Additionally, it can interfere with Al plating on the surface of the negative electrode, as observed in our study with ANU-20000 electrolyte. Even if Al can be plated, the presence of water residue can lead to the formation of Al oxide/hydroxides, which act as non-conductive barriers, hindering further stripping processes and/or decreasing plating and stripping efficiency. Moreover, the electrolyte might decompose near the negative electrode, potentially by altering the local pH due to the HER reaction. This effect was suspected to be related to the decomposition products observed on the cycled Al electrode in the A15E1Py2 electrolyte (refer to chapter 5.2.2.2).

Unfortunately, accurately determining and removing water content in RAB electrolytes is a big challenge. For instance, it is difficult to track water in highly corrosive ionic liquid electrolytes like Lewis acid  $\text{AlCl}_3\text{-EMImCl}$  mixtures due to their corrosive nature, which would damage the Pt electrode used in KF titration. Although high-purity precursors like  $\text{AlCl}_3$  and EMImCl are employed to minimize impurities, ensuring complete dryness after electrolyte preparation remains a challenge.

Commercially available  $\text{Al(OTf)}_3$  salts, often used in non-corrosive electrolytes, inherently contain water as demonstrated by ATR-FTIR, DSC, and TGA-MS analysis. This bound water exhibits remarkable stability, resisting removal by thermal desorption or chemical dehydration. Heating  $\text{Al(OTf)}_3$  beyond 200 °C likely leads to irreversible decomposition, forming an amorphous glass.<sup>158</sup> Therefore, electrolytes using  $\text{Al(OTf)}_3$  require further drying processes, as seen with the ANU-20000 electrolyte in Chapter 4.3, which underwent an intensive four-month drying process using  $\text{CaCl}_2$  and  $\text{P}_4\text{O}_{10}$ .

When tracking the water using KF titration, it is also important to note that any redox-active component such as DMSO can react with iodine in the reagent, generating false results. Therefore, many electrolyte formulations containing components like cyclic and non-cyclic carbonates, keto-esters, and additives like Fluoroethylene carbonate (FEC) and vinylene carbonate (VC) require special KF reagents designed for challenging electrolyte formulations.<sup>159,160</sup>

### **6.3 Challenges of in-situ characterization in RABs research**

While in-situ characterization techniques like Raman spectroscopy, XAS, and XRD offer invaluable insights into the dynamic behavior of electrodes and electrolytes during operation, their application in RABs research remains limited. Conventional cell designs used for in-situ characterization techniques are unsuitable due to the corrosive nature of ionic liquid electrolytes.<sup>5</sup> The inherent risk of leakage of the cells and damage to expensive equipment, significantly hinders the adoption of these techniques for studying RABs.

For instance, in this work, ex-situ XPS was employed to analyze the surface composition of Al negative electrodes and AISI 316L as a potential current collector. However, to prevent damage to the XPS instrument, samples require washing, potentially removing surface species crucial for understanding the electrode-electrolyte interface. This highlights a critical challenge for the RABs research community – the lack of readily available and reliable in-situ characterization techniques.

## 7 Conclusion

The feasibility of aluminum (Al) plating on platinum (Pt) electrodes using the  $\text{Al}(\text{OTf})_3/\text{NMA}/\text{urea}$  (ANU-20000) electrolyte was investigated as an alternative to the corrosive chloroaluminate ionic liquid electrolytes. While CV measurements indicate redox activity on the Pt electrode, further analysis revealed a critical limitation. No significant Al plating can be observed through scanning electron microscope/ energy-dispersive X-ray spectroscopy (SEM/EDX) techniques. Instead, the observed current is dominated by the hydrogen evolution reaction (HER), confirmed by *operando* microscopy and Gas Chromatography (GC) measurements. Residual water in the electrolyte, after drying procedures mentioned in literature<sup>26</sup>, is identified as the primary cause of HER.

Further investigation using Electrochemical Quartz Crystal Microbalance (EQCM) suggests the concurrent adsorption/desorption of  $\text{Al}(\text{OH})^{2+}$  and  $\text{Al}^{3+}$  ions on the Pt surface during cyclic voltammetry (CV) measurements. However, these adsorbed Al species do not translate to successful Al plating, likely due to the competing HER side reaction. Notably, the urea-containing electrolyte (ANU-20000) facilitates the dissociation of  $\text{Al}(\text{OTf})_3$ , promoting the adsorption of  $\text{Al}(\text{OH})^{2+}$  and  $\text{Al}^{3+}$  ions. This means that without urea, this reversible adsorption of cations does not occur, as indicated by EQCM.

Drying the ANU-20000 electrolyte to a residual water content of approximately 300 ppm significantly reduces the redox activity observed in CV, suggesting a decrease in HER activity. Furthermore, GC measurements confirm that the gas formation in the dried electrolyte approaches the instrument's detection limit. However, despite the reduced HER, metallic Al on the Pt electrode surface after polarization in the dried (ANU-300) electrolyte cannot be detected using X-ray photoelectron spectroscopy (XPS). The chosen electrolyte might inherently have limitations in promoting Al plating or residual water-related impurities in the dried electrolyte and could still hinder Al plating on the Pt surface.

These findings suggest that while the  $\text{Al}(\text{OTf})_3/\text{NMA}/\text{urea}$  mixture offers some advantages over  $\text{AlCl}_3$ -based electrolytes, its limited observed reversible Al plating and stripping, even after intensive drying, hinders its immediate suitability for rechargeable aluminum batteries (RABs).

Another approach was taken to address the corrosion issues of chloroaluminate ionic liquid electrolytes by using inhibitors to mitigate the corrosion of AISI 316L, a candidate for current collectors. While AISI 316L exhibits excellent corrosion resistance in various environments, it experiences vulnerability to significant corrosion in this electrolyte, leading to the formation of iron chloride.

The application of inhibitors— EMImOTf, EMImBF<sub>4</sub>, and Py1.4Cl<sup>-</sup> —, offer a degree of corrosion protection at OCV, with EMImOTf demonstrating the best performance, inhibition efficiency of 64±9 %, based on potentiodynamic polarization and surface analysis using XPS. This improvement likely stems from the adsorption/reduction of the inhibitor's cations on the AISI 316L surface.

Despite mitigating corrosion to some extent, both EMImOTf and EMImBF<sub>4</sub> inhibitors cannot fully address the issue at high potentials of 1.5V vs. Al. XPS analysis confirms the presence of less iron chlorides formation probably due to the adsorption of reduced inhibitor cations (EMIm<sup>0</sup>), as well as the adsorption/decomposition of the corresponding anions (OTf<sup>-</sup> and BF<sub>4</sub><sup>-</sup>). However, concerns arise about the suitability of AISI 316L as a current collector in these electrolytes. The observed corrosion rates with inhibitors are still too high for AISI 316L to be a viable option for practical applications.

Furthermore, CV measurements reveal a critical restriction: the presence of inhibitors hinders Al plating and stripping, particularly in the initial cycles, although Al plating/stripping current density increases over cycling in all electrolytes. This highlights the delicate balance required between corrosion protection and achieving efficient Al plating and stripping, the core electrochemical process in RABs. Interestingly, the A15E1OTf2 electrolyte containing EMImOTf exhibits the least impact on Al plating and stripping compared to other inhibitor-containing electrolytes, possibly due to lower inhibitor cation adsorption/decomposition. In contrast, A15E1BF2 and A15E1Py2 exhibit limited Al plating and stripping in initial cycles but improve over time. This can be linked to the initial adsorption/decomposition of inhibitor cations on the Al surface and subsequent instability during cycling as confirmed by XPS. Overall, while inhibitors may offer some corrosion mitigation, their impact on Al plating and stripping poses a challenge for their practical application in RABs.

Several technical challenges in evaluating RABs has delved into the complexities of selecting an appropriate reference electrode for non-aqueous systems, the detrimental effects of water in RABs, and the limitations of in-situ characterization techniques for studying RABs research.

## 8 Outlook

The journey towards Rechargeable Aluminum Batteries (RABs) reveals a promising pathway for advancement filled with complicated challenges.

A fundamental obstacle lies in the inadequacy of conventional reference electrodes (SCE and Ag/AgCl) within non-aqueous environments. To address the limitations of conventional reference electrodes, it is beneficial to investigate the behavior of pseudo-reference electrodes, specifically focusing on Al metal. The research on truly stable and consistent reference electrode that function effectively across diverse electrolytes is an essential step towards achieving accurate potential measurements in RABs.

Future efforts should prioritize the development of advanced electrolytes specifically formulated to suppress HER. This multifaceted approach may involve incorporating water scavengers to meticulously eliminate water content, alongside implementing stricter drying procedures. Establishing accurate water content determination, particularly for highly corrosive ionic liquid electrolytes is an essential step for optimizing RABs electrolyte performance.

Using alternative Al salts (instead of  $\text{AlCl}_3$ ) in combination with weakly coordinating solvents or deep eutectic systems could potentially address the challenges faced by RABs. Research has identified electrolytes in which Al salts dissolve successfully; however, these electrolytes have not confirmed Al plating and stripping (refer to Table. 1 in chapter 2.3). One approach could be to use an anode material that facilitates the interaction of  $\text{Al}^{3+}$  ions, rather than relying on Al plating. While this would negatively affect the volumetric capacity of RABs compared to using Al metal, it could circumvent the issue of the native oxide layer on Al metal. This strategy would allow for the use of non-corrosive electrolytes, thereby solving the problem of corrosion of the current collectors and cell components.

While the corrosion inhibitors might offer promise in protecting current collectors within chloroaluminate ionic liquid electrolytes, a potential drawback exists. These inhibitors might also adsorb onto the Al metal itself during battery operation. This adsorption could hinder the essential process of Al plating and stripping on the negative electrode, even if the inhibitor successfully protects the current collector. Therefore, if Al metal remains the negative electrode material, alternative approaches to reduce electrolyte corrosivity may be necessary. One

promising avenue could be the adoption of gel electrolytes as it is suggested that gel electrolytes can reduce electrolyte corrosivity.<sup>31,79</sup> Exploring such alternatives could be a valuable strategy for optimizing RABs performance.

A significant technical limitation of this study was the inability to directly observe the real-time interactions between inhibitors and the electrode surface due to ex-situ characterization techniques and sample washing procedures. This highlights the need for advanced in-situ characterization techniques, such as near-ambient pressure XPS. This approach could provide invaluable insights into surface chemistry, particularly the role of anion adsorption, aiding researchers in understanding the puzzle of corrosion inhibition within RABs.

However, to integrate in-situ characterization techniques, specialized cell designs that can withstand the harsh and corrosive nature of corrosive ionic liquid electrolytes are crucial. These advanced designs would not only minimize leakage and protect expensive equipment. This would be a significant boom for the RAB research community, allowing for real-time observation and analysis of RAB behavior within operational conditions.

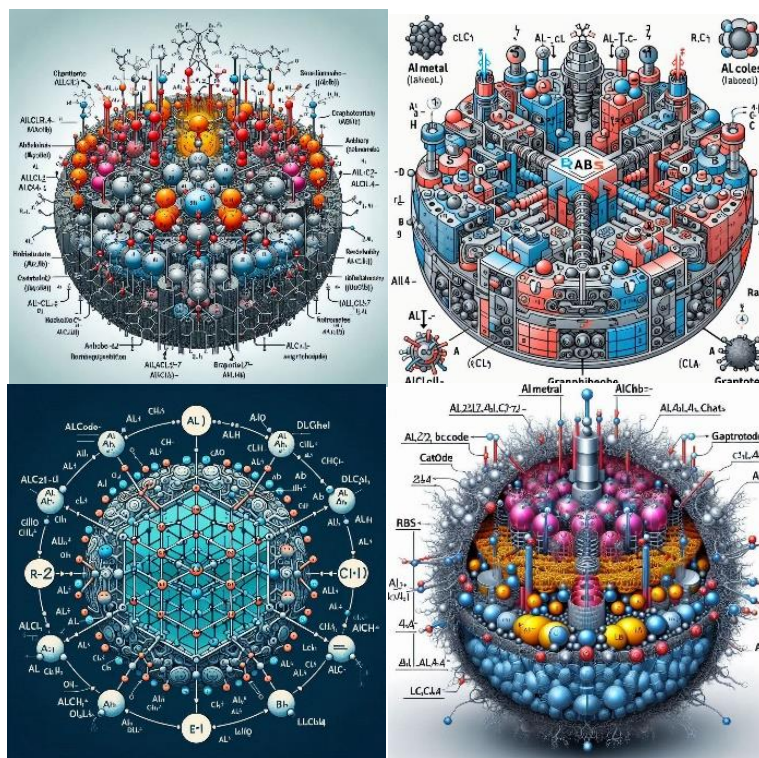
By addressing these challenges and pursuing these exciting avenues of exploration, researchers can unlock the immense potential of RABs, paving the way for a more sustainable and efficient energy future.

## A pinch of amusement

**Me:** Can you generate for me a schematic figure of the RABs, with Al metal as Anode and graphite as cathode and  $[\text{Al}_2\text{Cl}_7]^-$  and  $[\text{AlCl}_4]^-$  species inside the electrolyte?



I'll try to create that.

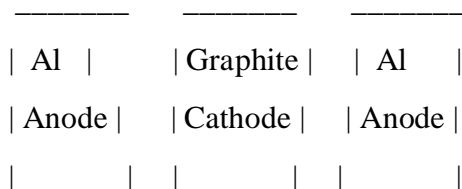


**Me:** oh, I meant simply a simple electrochemistry Cell!



I apologize for the misunderstanding! Let's create a schematic diagram of a simple electrochemical cell with aluminum (Al) as the anode and graphite as the cathode.

Here's a basic representation:




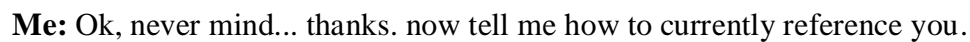
**Me:** Thanks, but, please generate a simple Al battery Cell with Al metal and graphite as Anode and cathode

Certainly! Let's create a schematic diagram of a simple aluminum (Al) battery cell with Al metal as the anode and graphite as the cathode: Feel free to ask if you need further clarification or additional details! 😊





 I apologize for the oversight! Let's create a more accurate schematic diagram of an aluminum (Al) battery cell with Al metal as the anode and graphite as the cathode. This time, I'll represent the layers as flat surfaces:



**Me:** No, I mean how to mention that you have made the picture, scientifically referencing you

**“Figure created by an AI assistant using Copilot.”**

90

## 9 References

1. Yang Z, Zhang J, Kintner-Meyer MCW, et al. Electrochemical energy storage for green grid. *Chem Rev.* 2011;111(5):3577-3613.
2. Tarascon JM, Armand M. Issues and challenges facing rechargeable lithium batteries. *Nature.* 2001;414(6861):359-367. doi:10.1038/35104644
3. Tarascon JM. Is lithium the new gold? *Nat Chem.* 2010;2(6):510.
4. Craig B, Schoetz T, Cruden A, de Leon CP. Review of current progress in non-aqueous aluminium batteries. *Renew Sustain Energy Rev.* 2020;133:110100.
5. Zhang Y, Liu S, Ji Y, Ma J, Yu H. Emerging nonaqueous aluminum-ion batteries: challenges, status, and perspectives. *Adv Mater.* 2018;30(38):1706310.
6. Wu X, Qin N, Wang F, et al. Reversible aluminum ion storage mechanism in Ti-deficient rutile titanium dioxide anode for aqueous aluminum-ion batteries. *Energy Storage Mater.* 2021;37:619-627.
7. Schoetz T, Craig B, de Leon CP, Bund A, Ueda M, Low CTJ. Aluminium-poly (3, 4-ethylenedioxythiophene) rechargeable battery with ionic liquid electrolyte. *J Energy Storage.* 2020;28:101176.
8. Cheng Y, Luo L, Zhong L, et al. Highly reversible zinc-ion intercalation into chevre phase  $\text{Mo}_6\text{S}_8$  nanocubes and applications for advanced zinc-ion batteries. *ACS Appl Mater Interfaces.* 2016;8(22):13673-13677.
9. Kummer JT, Weber N. A sodium-sulfur secondary battery. *Sae Trans.* Published online 1968:1003-1028.
10. Chandrasekaran R, Ruth Mangani I, Vasanthi R, Selladurai S. Ionic conductivity and battery characteristic studies on  $\text{PEO}^+ \text{NaClO}_3$  polymer electrolyte. *Ionics (Kiel).* 2001;7:88-93.
11. Singer J, Fielder WL, Kautz HE, Fordyce JS. New solid conductors of  $\text{Na}^+$  and  $\text{K}^+$  ions. *J Electrochem Soc.* 1976;123(5):614.
12. Zhao Q, Hu Y, Zhang K, Chen J. Potassium-sulfur batteries: A new member of room-temperature rechargeable metal-sulfur batteries. *Inorg Chem.* 2014;53(17):9000-9005.
13. Di Noto V, Lavina S, Longo D, Vidali M. A novel electrolytic complex based on  $\delta$ - $\text{MgCl}_2$  and poly (ethylene glycol) 400. *Electrochim Acta.* 1998;43(10-11):1225-1237.
14. Di Noto V, Münchow V, Vittadello M, Collet JC, Lavina S. Synthesis, characterization and conductivity studies of Li and Mg polymer electrolytes based on esters of ethylenediaminetetraacetic acid and PEG400. *Solid State Ionics.* 2002;147(3-4):397-402.
15. Biscazzo S, Vittadello M, Lavina S, Di Noto V. Synthesis and structure of electrolytic complexes based on  $\alpha$ -hydro- $\omega$ -oligo (oxyethylene) hydroxy-poly [oligo (oxyethylene) oxydimethylsililene] and  $\delta$ - $\text{MgCl}_2$ . *Solid state ionics.* 2002;147(3-4):377-382.

16. Dominko R, Bitenc J, Berthelot R, Gauthier M, Pagot G, Di Noto V. Magnesium batteries: Current picture and missing pieces of the puzzle. *J Power Sources*. 2020;478:229027.
17. Lipson AL, Pan B, Lapidus SH, Liao C, Vaughey JT, Ingram BJ. Rechargeable Ca-ion batteries: a new energy storage system. *Chem Mater*. 2015;27(24):8442-8447.
18. Ponrouch A, Frontera C, Bardé F, Palacín MR. Towards a calcium-based rechargeable battery. *Nat Mater*. 2016;15(2):169-172.
19. Martinez-Cisneros CS, Fernandez A, Antonelli C, et al. Opening the door to liquid-free polymer electrolytes for calcium batteries. *Electrochim Acta*. 2020;353:136525.
20. Muñoz-Torrero D, Palma J, Marcilla R, Ventosa E. A critical perspective on rechargeable Al-ion battery technology. *Dalt Trans*. 2019;48(27):9906-9911.
21. Ng KL, Lu Z, Wang Y, Singh CV, Azimi G. Fundamental insights into electrical and transport properties of chloroaluminate ionic liquids for aluminum-ion batteries. *J Phys Chem C*. 2021;125(28):15145-15154.
22. Yuan D, Zhao J, Manalastas Jr W, Kumar S, Srinivasan M. Emerging rechargeable aqueous aluminum ion battery: Status, challenges, and outlooks. *Nano Mater Sci*. 2020;2(3):248-263.
23. Pagot G, Vezzù K, Greenbaum SG, Di Noto V. Hybrid twin-metal aluminum–magnesium electrolytes for rechargeable batteries. *J Power Sources*. 2021;493:229681.
24. Ponrouch A, Bitenc J, Dominko R, Lindahl N, Johansson P, Palacín MR. Multivalent rechargeable batteries. *Energy Storage Mater*. 2019;20:253-262.
25. Das SK, Mahapatra S, Lahan H. Aluminium-ion batteries: developments and challenges. *J Mater Chem A*. 2017;5(14):6347-6367.
26. Mandai T, Johansson P. Al conductive haloaluminate-free non-aqueous room-temperature electrolytes. *J Mater Chem A*. 2015;3(23):12230-12239.
27. Han X, Bai Y, Zhao R, Li Y, Wu F, Wu C. Electrolytes for Rechargeable Aluminum Batteries. *Prog Mater Sci*. Published online 2022:100960.
28. Schötz T, de Leon CP, Ueda M, Bund A. Perspective—state of the art of rechargeable aluminum batteries in non-aqueous systems. *J Electrochem Soc*. 2017;164(14):A3499.
29. Tu J, Song WL, Lei H, et al. Nonaqueous rechargeable aluminum batteries: progresses, challenges, and perspectives. *Chem Rev*. 2021;121(8):4903-4961.
30. Leung OM, Schoetz T, Prodromakis T, Ponce de Leon C. Review—Progress in Electrolytes for Rechargeable Aluminium Batteries. *J Electrochem Soc*. 2021;168(5):056509. doi:10.1149/1945-7111/abfb36
31. Elia GA, Acevedo CI, Kazemi R, Fantini S, Lin R, Hahn R. A Gel Polymer Electrolyte for Aluminum Batteries. *Energy Technol*. 2021;9(8). doi:10.1002/ente.202100208
32. Faraday M. VI. Experimental researches in electricity.-Seventh Series. *Philos Trans R Soc London*. 1834;(124):77-122.

33. Lee J, Srimuk P, Fleischmann S, Su X, Hatton TA, Presser V. Redox-electrolytes for non-flow electrochemical energy storage: A critical review and best practice. *Prog Mater Sci.* 2019;101:46-89.
34. Paranthaman P, Brown GM, Sun X, Nanda J, Manthiram A, Manivannan A. *A Transformational, High Energy Density Secondary Aluminum Ion Battery.*; 2010. [http://www.sc.doe.gov/bes/reports/files/EES\\_rpt.pdf](http://www.sc.doe.gov/bes/reports/files/EES_rpt.pdf)
35. Wang H, Bai Y, Chen S, et al. Binder-free V<sub>2</sub>O<sub>5</sub> cathode for greener rechargeable aluminum battery. *ACS Appl Mater Interfaces.* 2015;7(1):80-84. doi:10.1021/am508001h
36. Hudak NS. Chloroaluminate-Doped Conducting Polymers as Positive Electrodes in Rechargeable Aluminum Batteries. *J Phys Chem C.* 2014;118(10):5203-5215. doi:10.1021/jp500593d
37. Lin MC, Gong M, Lu B, et al. An ultrafast rechargeable aluminium-ion battery. *Nature.* 2015;520(7547):325-328. doi:10.1038/nature14340
38. Dong X, Xu H, Chen H, et al. Commercial expanded graphite as high-performance cathode for low-cost aluminum-ion battery. *Carbon N Y.* 2019;148:134-140.
39. Bhauriyal P, Mahata A, Pathak B. The staging mechanism of AlCl<sub>4</sub> intercalation in a graphite electrode for an aluminium-ion battery. *Phys Chem Chem Phys.* 2017;19(11):7980-7989.
40. Faegh E, Ng B, Hayman D, Mustain WE. Practical assessment of the performance of aluminium battery technologies. *Nat Energy.* 2021;6(1):21-29.
41. Huang MC, Yang CH, Chiang CC, et al. Influence of High Loading on the Performance of Natural Graphite-Based Al Secondary Batteries. *Energies.* 2018;11(10):12-16. doi:10.3390/en11102760
42. Shi J, Zhang J, Guo J. Avoiding Pitfalls in Rechargeable Aluminum Batteries Research. *ACS Energy Lett.* 2019;4(9):2124-2129. doi:10.1021/acsenergylett.9b01285
43. Kowsari E, Payami M, Amini R, Ramezanzadeh B, Javanbakht M. Task-specific ionic liquid as a new green inhibitor of mild steel corrosion. *Appl Surf Sci.* 2014;289:478-486. doi:https://doi.org/10.1016/j.apsusc.2013.11.017
44. Corrales-Luna M, Le Manh T, Romero-Romo M, Palomar-Pardavé M, Arce-Estrada EM. 1-Ethyl 3-methylimidazolium thiocyanate ionic liquid as corrosion inhibitor of API 5L X52 steel in H<sub>2</sub>SO<sub>4</sub> and HCl media. *Corros Sci.* 2019;153:85-99. doi:https://doi.org/10.1016/j.corsci.2019.03.041
45. Zunita M, Kevin YJ. Ionic liquids as corrosion inhibitor: From research and development to commercialization. *Results Eng.* 2022;15:100562. doi:https://doi.org/10.1016/j.rineng.2022.100562
46. Ardakani EK, Kowsari E, Ehsani A, Ramakrishna S. Performance of all ionic liquids as the eco-friendly and sustainable compounds in inhibiting corrosion in various media: A comprehensive review. *Microchem J.* 2021;165:106049.

doi:<https://doi.org/10.1016/j.microc.2021.106049>

47. Naseri E, Hajisafari M, Kosari A, Talari M, Hosseinpour S, Davoodi A. Inhibitive effect of Clopidogrel as a green corrosion inhibitor for mild steel; statistical modeling and quantum Monte Carlo simulation studies. *J Mol Liq.* 2018;269:193-202.
48. Talari M, Nezhad SM, Alavi SJ, Mohtashamipour M, Davoodi A, Hosseinpour S. Experimental and computational chemistry studies of two imidazole-based compounds as corrosion inhibitors for mild steel in HCl solution. *J Mol Liq.* 2019;286:110915.
49. Miyake M, Fujii H, Hirato T. Electroplating of Al on Mg alloy in a dimethyl sulfone–aluminum chloride bath. *Surf Coatings Technol.* 2015;277:160-164. doi:<https://doi.org/10.1016/j.surfcoat.2015.07.047>
50. Legrand L, Tranchant A, Messina R. Electrodeposition Studies of Aluminum on Tungsten Electrode from DMSO<sub>2</sub> Electrolytes: Determination of Al<sup>III</sup> Species Diffusion Coefficients. *J Electrochem Soc.* 1994;141(2):378. doi:10.1149/1.2054735
51. Nakayama Y, Senda Y, Kawasaki H, et al. Sulfone-based electrolytes for aluminium rechargeable batteries. *Phys Chem Chem Phys.* 2015;17(8):5758-5766.
52. Legrand L, Heintz M, Tranchant A, Messina R. Sulfone-based electrolytes for aluminum electrodeposition. *Electrochim Acta.* 1995;40(11):1711-1716. doi:[https://doi.org/10.1016/0013-4686\(95\)00019-B](https://doi.org/10.1016/0013-4686(95)00019-B)
53. Zhang Z, Kitada A, Gao S, et al. A Concentrated AlCl<sub>3</sub>–Diglyme Electrolyte for Hard and Corrosion-Resistant Aluminum Electrodeposits. *ACS Appl Mater Interfaces.* 2020;12(38):43289-43298.
54. Li M, Gao B, Liu C, et al. Electrodeposition of aluminum from AlCl<sub>3</sub>/acetamide eutectic solvent. *Electrochim Acta.* 2015;180:811-814.
55. Wen X, Liu Y, Xu D, Zhao Y, Lake RK, Guo J. Room-temperature electrodeposition of aluminum via manipulating coordination structure in AlCl<sub>3</sub> solutions. *J Phys Chem Lett.* 2020;11(4):1589-1593.
56. Couch DE, Brenner A. A hydride bath for the electrodeposition of aluminum. *J Electrochem Soc.* 1952;99(6):234.
57. Ishibashi N, Yoshio M. Electrodeposition of aluminium from the NBS type bath using tetrahydrofuran—benzene mixed solvent. *Electrochim Acta.* 1972;17(8):1343-1352. doi:[https://doi.org/10.1016/0013-4686\(72\)80080-X](https://doi.org/10.1016/0013-4686(72)80080-X)
58. Badawy WA, Sabrah BA, Hilal NHY. A new bath for the electrodeposition of aluminium. II. Kinetics and mechanism of the deposition and dissolution processes. *J Appl Electrochem.* 1987;17(2):357-369. doi:10.1007/BF01023302
59. Graef MWM. The mechanism of aluminum electrodeposition from solutions of AlCl<sub>3</sub> and LiAlH<sub>4</sub> in THF. *J Electrochem Soc.* 1985;132(5):1038.
60. Lefebvre MC, Conway BE. Nucleation and morphologies in the process of electrocrystallization of aluminium on smooth gold and glassy-carbon substrates. *J*

- Electroanal Chem.* 2000;480(1):46-58. doi:[https://doi.org/10.1016/S0022-0728\(99\)00444-1](https://doi.org/10.1016/S0022-0728(99)00444-1)
61. Lefebvre MC, Conway BE. Elementary steps and mechanism of electrodeposition of Al from complex hydride ions in tetrahydrofuran baths. *J Electroanal Chem.* 2000;480(1):34-45. doi:[https://doi.org/10.1016/S0022-0728\(99\)00443-X](https://doi.org/10.1016/S0022-0728(99)00443-X)
  62. Yoshio M, Ishibashi N. High-rate plating of aluminium from the bath containing aluminium chloride and lithium aluminium hydride in tetrahydrofuran. *J Appl Electrochem.* 1973;3(4):321-325. doi:10.1007/BF00613040
  63. Mandai T, Johansson P. Haloaluminate-free cationic aluminum complexes: structural characterization and physicochemical properties. *J Phys Chem C.* 2016;120(38):21285-21292.
  64. Chiku M, Matsumura S, Takeda H, Higuchi E, Inoue H. Aluminum bis (trifluoromethanesulfonyl) imide as a chloride-free electrolyte for rechargeable aluminum batteries. *J Electrochem Soc.* 2017;164(9):A1841.
  65. Wen X, Zhang J, Luo H, et al. Synthesis and electrochemical properties of aluminum hexafluorophosphate. *J Phys Chem Lett.* 2021;12(25):5903-5908.
  66. Slim Z, Menke EJ. Comparing Computational Predictions and Experimental Results for Aluminum Triflate in Tetrahydrofuran. *J Phys Chem B.* 2020;124(24):5002-5008. doi:10.1021/acs.jpcb.0c02570
  67. Slim Z, Menke EJ. Aluminum Electrodeposition from Chloride-Rich and Chloride-Free Organic Electrolytes. *J Phys Chem C.* 2022;126(5):2365-2373.
  68. Jayaprakash N, Das SK, Archer LA. The rechargeable aluminum-ion battery. *Chem Commun.* 2011;47(47):12610-12612.
  69. Reed LD, Arteaga A, Menke EJ. A combined experimental and computational study of an aluminum triflate/diglyme electrolyte. *J Phys Chem B.* 2015;119(39):12677-12681.
  70. Reed LD, Ortiz SN, Xiong M, Menke EJ. A rechargeable aluminum-ion battery utilizing a copper hexacyanoferrate cathode in an organic electrolyte. *Chem Commun.* 2015;51(76):14397-14400.
  71. Peters W, Duong HT, Lee S, Drillet JF. Investigation of Al (TfO)<sub>3</sub>-based deep eutectic solvent electrolytes for aluminium-ion batteries. Part I: understanding the positively charged Al complex formation. *Phys Chem Chem Phys.* 2021;23(38):21923-21933.
  72. Slim Z, Menke E. Hydride-Enhanced Plating and Stripping of Aluminum from Tri-flate-Based Organic Electrolytes. Published online 2022.
  73. Holleck GL, Giner J, Burrows B. Rechargeable Al/Cl<sub>2</sub> battery with molten AlCl<sub>4</sub><sup>-</sup>/electrolyte. In: *From Electrocatalysis to Fuel Cells; Seminar.* ; 1972.
  74. Wang J, Zhang X, Chu W, Liu S, Yu H. A sub-100° C aluminum ion battery based on a ternary inorganic molten salt. *Chem Commun.* 2019;55(15):2138-2141.
  75. Galiński M, Lewandowski A, Stępiak I. Ionic liquids as electrolytes. *Electrochim Acta.*

- 2006;51(26):5567-5580. doi:<https://doi.org/10.1016/j.electacta.2006.03.016>
76. Ma D, Yuan D, Ponce de León C, Jiang Z, Xia X, Pan J. Current Progress and Future Perspectives of Electrolytes for Rechargeable Aluminum-Ion Batteries. *Energy Environ Mater*. 2023;6(1):1-18. doi:10.1002/eem2.12301
  77. Giffin GA. Ionic liquid-based electrolytes for “beyond lithium” battery technologies. *J Mater Chem A*. 2016;4(35):13378-13389. doi:10.1039/c6ta05260f
  78. Hu Z, Zhang H, Wang H, Zhang F, Li Q, Li H. Nonaqueous Aluminum Ion Batteries: Recent Progress and Prospects. *ACS Mater Lett*. 2020;2(8):887-904. doi:10.1021/acsmaterialslett.0c00208
  79. Sun XG, Fang Y, Jiang X, Yoshii K, Tsuda T, Dai S. Polymer gel electrolytes for application in aluminum deposition and rechargeable aluminum ion batteries. *Chem Commun*. 2016;52(2):292-295.
  80. Miguel Á, García N, Gregorio V, López-Cudero A, Tiemblo P. Tough Polymer Gel Electrolytes for Aluminum Secondary Batteries Based on Urea:  $\text{AlCl}_3$ , Prepared by a New Solvent-Free and Scalable Procedure. *Polymers (Basel)*. 2020;12(6). doi:10.3390/polym12061336
  81. Schoetz T, Leung O, de Leon CP, Zaleski C, Efimov I. Aluminium deposition in EMImCl- $\text{AlCl}_3$  ionic liquid and ionogel for improved aluminium batteries. *J Electrochem Soc*. 2020;167(4):40516.
  82. Kotobuki M, Lu L, Savilov S V, Aldoshin SM. Poly (vinylidene fluoride)-based Al ion conductive solid polymer electrolyte for Al battery. *J Electrochem Soc*. 2017;164(14):A3868.
  83. Wilkes JS. A short history of ionic liquids - From molten salts to neoteric solvents. *Green Chem*. 2002;4(2):73-80. doi:10.1039/b110838g
  84. Carlin RT, Crawford W, Bersch M. Nucleation and morphology studies of aluminum deposited from an ambient-temperature chloroaluminate molten salt. *J Electrochem Soc*. 1992;139(10):2720.
  85. Carlin RT, Trulove PC, Hugh C. Electrodeposition of Cobalt-Aluminum Alloys from Room Temperature Chloroaluminate Molten Salt. *J Electrochem Soc*. 1996;143(9):2747.
  86. Ueda M, Susukida D, Konda S, Ohtsuka T. Improvement of resistance of TiAl alloy against high temperature oxidation by electroplating in  $\text{AlCl}_3$ - $\text{NaCl}$ - $\text{KCl}$ - $\text{CrCl}_2$  molten salt. *Surf Coatings Technol*. 2004;176(2):202-208.
  87. Agiorgousis ML, Sun YY, Zhang S. The role of ionic liquid electrolyte in an aluminum-graphite electrochemical cell. *ACS Energy Lett*. 2017;2(3):689-693.
  88. Angell M, Pan CJ, Rong Y, et al. High Coulombic efficiency aluminum-ion battery using an  $\text{AlCl}_3$ -urea ionic liquid analog electrolyte. *Proc Natl Acad Sci*. 2017;114(5):834-839.

89. Huynh TC, Dao QPD, Truong TN, Doan NG, Ho SL. Electrodeposition of aluminum on cathodes in ionic liquid based choline chloride/urea/ $\text{AlCl}_3$ . *Environ Pollut.* 2014;3(4):59-69.
90. Zhao Y, VanderNoot TJ. Electrodeposition of aluminium from nonaqueous organic electrolytic systems and room temperature molten salts. *Electrochim Acta.* 1997;42(1):3-13. doi:[https://doi.org/10.1016/0013-4686\(96\)00080-1](https://doi.org/10.1016/0013-4686(96)00080-1)
91. Wasserscheid P, Welton T. *Ionic Liquids in Synthesis*. Vol 1. Wiley Online Library; 2008.
92. Wang H, Gu S, Bai Y, et al. Anion-effects on electrochemical properties of ionic liquid electrolytes for rechargeable aluminum batteries. *J Mater Chem A.* 2015;3(45):22677-22686.
93. Reynolds GF, Dymek Jr CJ. Primary and secondary room temperature molten salt electrochemical cells. *J Power Sources.* 1985;15(2-3):109-118.
94. Zein El Abedin S, Giridhar P, Schwab P, Endres F. Electrodeposition of nanocrystalline aluminium from a chloroaluminate ionic liquid. *Electrochem commun.* 2010;12(8):1084-1086. doi:10.1016/j.elecom.2010.05.034
95. Yang H, Wu F, Bai Y, Wu C. Toward better electrode/electrolyte interfaces in the ionic-liquid-based rechargeable aluminum batteries. *J Energy Chem.* 2020;45:98-102. doi:10.1016/j.jechem.2019.10.003
96. Nappini S, Matruglio A, Naumenko D, et al. Graphene nanobubbles on  $\text{TiO}_2$  for *in-operando* electron spectroscopy of liquid-phase chemistry. *Nanoscale.* 2017;9(13):4456-4466. doi:10.1039/c6nr09061c
97. Qin QX, Skylas-Kazacos M. Electrodeposition and dissolution of aluminium in ambient temperature molten salt system aluminium chloride n-butylpyridinium chloride. *J Electroanal Chem Interfacial Electrochem.* 1984;168(1):193-206. doi:[https://doi.org/10.1016/0368-1874\(84\)87098-7](https://doi.org/10.1016/0368-1874(84)87098-7)
98. Ge X, Li J, Zhang C, Wang Z, Luo J. Superlubricity of 1-ethyl-3-methylimidazolium trifluoromethanesulfonate ionic liquid induced by tribochemical reactions. *Langmuir.* 2018;34(18):5245-5252.
99. Pitner WR, Hussey CL, Stafford GR. Electrodeposition of Nickel-Aluminum Alloys from the Aluminum Chloride-1-methyl-3-ethylimidazolium Chloride Room Temperature Molten Salt. *J Electrochem Soc.* 1996;143(1):130-138. doi:10.1149/1.1836397
100. Liao Q, Pitner WR, Stewart G, Hussey CL, Stafford GR. Electrodeposition of Aluminum from the Aluminum Chloride-1-Methyl-3-ethylimidazolium Chloride Room Temperature Molten Salt + Benzene. *J Electrochem Soc.* 1997;144(3):936-943. doi:10.1149/1.1837510
101. Pradhan D, Reddy RG. Mechanistic study of Al electrodeposition from EMIC– $\text{AlCl}_3$  and BMIC– $\text{AlCl}_3$  electrolytes at low temperature. *Mater Chem Phys.* 2014;143(2):564-



569. doi:10.1016/J.MATCHEMPHYS.2013.09.033
102. KAN H min, WANG Z wen, WANG X yang, ZHANG N. Electrochemical deposition of aluminum on W electrode from  $\text{AlCl}_3$ -NaCl melts. *Trans Nonferrous Met Soc China*. 2010;20(1):158-164. doi:[https://doi.org/10.1016/S1003-6326\(09\)60114-X](https://doi.org/10.1016/S1003-6326(09)60114-X)
  103. Elterman VA, Shevelin PY, Yolshina LA, Vovkotrub EG, Borozdin A V. Effects of  $\text{AlCl}_3$ -1-ethyl-3-methylimidazolium chloride ionic liquid composition on transport properties. *J Mol Liq*. 2020;320:114482.
  104. Melton TJ, Joyce J, Maloy JT, Boon JA, Wilkes JS. Electrochemical studies of sodium chloride as a Lewis buffer for room temperature chloroaluminate molten salts. *J Electrochem Soc*. 1990;137(12):3865.
  105. Carlin RT, Osteryoung RA. Aluminum anodization in a basic ambient temperature molten salt. *J Electrochem Soc*. 1989;136(5):1409.
  106. Chrysoulakis Y, Poignet JC, Manoli G. Electrochemical study of aluminium ion reduction in acidic  $\text{AlCl}_3$ -n-butyl-pyridinium chloride melts. *J Appl Electrochem*. 1987;17(4):857-867. doi:10.1007/BF01007824
  107. Oh Y, Lee G, Tak Y. Stability of Metallic Current Collectors in Acidic Ionic Liquid for Rechargeable Aluminum-Ion Batteries. *ChemElectroChem*. 2018;5(22):3348-3352. doi:10.1002/celec.201800892
  108. Fang Y, Yoshii K, Jiang X, et al. An  $\text{AlCl}_3$  based ionic liquid with a neutral substituted pyridine ligand for electrochemical deposition of aluminum. *Electrochim Acta*. 2015;160:82-88. doi:<https://doi.org/10.1016/j.electacta.2015.02.020>
  109. Yoshida K, Nakamura M, Kazue Y, et al. Oxidative-Stability Enhancement and Charge Transport Mechanism in Glyme–Lithium Salt Equimolar Complexes. *J Am Chem Soc*. 2011;133(33):13121-13129. doi:10.1021/ja203983r
  110. Terada S, Mandai T, Nozawa R, et al. Physicochemical properties of pentaglyme–sodium bis (trifluoromethanesulfonyl) amide solvate ionic liquid. *Phys Chem Chem Phys*. 2014;16(23):11737-11746.
  111. Yang H, Li H, Li J, et al. The Rechargeable Aluminum Battery: Opportunities and Challenges. *Angew Chemie Int Ed*. 2019;58(35):11978-11996. doi:<https://doi.org/10.1002/anie.201814031>
  112. Zhang X, Devine TM. Factors that influence formation of  $\text{AlF}_3$  passive film on aluminum in Li-ion battery electrolytes with  $\text{LiPF}_6$ . *J Electrochem Soc*. 2006;153(9):B375.
  113. Gerengi H, Solomon MM, Umoren SA, Ugras HI, Yildiz M, Slepiski P. Improved Performance of 1-Ethyl-3-Methylimidazolium Tetrafluoroborate at Steel/HCl Interface by Iodide Ions. *J Bio- Tribo-Corrosion*. 2018;4(1):12. doi:10.1007/s40735-018-0126-3
  114. Ma Y, Han F, Li Z, Xia C. Acidic-functionalized ionic liquid as corrosion inhibitor for 304 stainless steel in aqueous sulfuric acid. *ACS Sustain Chem Eng*. 2016;4(9):5046-5052.

115. Tüken T, Demir F, Kıcıır N, Sığircık G, Erbil M. Inhibition effect of 1-ethyl-3-methylimidazolium dicyanamide against steel corrosion. *Corros Sci.* 2012;59:110-118. doi:<https://doi.org/10.1016/j.corsci.2012.02.021>
116. Mashuga ME, Olasunkanmi LO, Adekunle AS, Yesudass S, Kabanda MM, Ebenso EE. Adsorption, Thermodynamic and Quantum Chemical Studies of 1-hexyl-3-methylimidazolium Based Ionic Liquids as Corrosion Inhibitors for Mild Steel in HCl. *Materials (Basel)*. 2015;8(6):3607-3632. doi:10.3390/ma8063607
117. Ashassi-Sorkhabi H, Es'haghi M. Corrosion inhibition of mild steel in acidic media by [BMIm]Br Ionic liquid. *Mater Chem Phys.* 2009;114(1):267-271. doi:<https://doi.org/10.1016/j.matchemphys.2008.09.019>
118. Zhang QB, Hua YX. Corrosion inhibition of mild steel by alkylimidazolium ionic liquids in hydrochloric acid. *Electrochim Acta.* 2009;54(6):1881-1887. doi:<https://doi.org/10.1016/j.electacta.2008.10.025>
119. Nkuna AA, Akpan ED, Obot IB, Verma C, Ebenso EE, Murulana LC. Impact of selected ionic liquids on corrosion protection of mild steel in acidic medium: Experimental and computational studies. *J Mol Liq.* 2020;314:113609. doi:<https://doi.org/10.1016/j.molliq.2020.113609>
120. El-Shamy AM, Zakaria K, Abbas MA, Zein El Abedin S. Anti-bacterial and anti-corrosion effects of the ionic liquid 1-butyl-1-methylpyrrolidinium trifluoromethylsulfonate. *J Mol Liq.* 2015;211:363-369. doi:<https://doi.org/10.1016/j.molliq.2015.07.028>
121. Zhou X, Yang H, Wang F. [BMIM]BF<sub>4</sub> ionic liquids as effective inhibitor for carbon steel in alkaline chloride solution. *Electrochim Acta.* 2011;56(11):4268-4275. doi:<https://doi.org/10.1016/j.electacta.2011.01.081>
122. Sherif ESM, Abdo HS, Abedin SZ El. Corrosion Inhibition of Cast Iron in Arabian Gulf Seawater by Two Different Ionic Liquids. *Materials (Basel)*. 2015;8(7):3883-3895. doi:10.3390/ma8073883
123. Zamindar S, Mandal S, Murmu M, Banerjee P. Unveiling the future of steel corrosion inhibition: a revolutionary sustainable odyssey with a special emphasis on N+-containing ionic liquids through cutting-edge innovations. *Mater Adv.* Published online 2024.
124. Lozano I, Mazario E, Olivares-Xometl CO, Likhanova N V, Herrasti P. Corrosion behaviour of API 5LX52 steel in HCl and H<sub>2</sub>SO<sub>4</sub> media in the presence of 1,3-dibencilimidazolium acetate and 1,3-dibencilimidazolium dodecanoate ionic liquids as inhibitors. *Mater Chem Phys.* 2014;147(1):191-197. doi:<https://doi.org/10.1016/j.matchemphys.2014.04.029>
125. TSC Surface - rhd instruments. Accessed May 14, 2024. <https://rhd-instruments.de/en/products/cells/tsc-surface>
126. EQCM. <https://www.gamry.com/support-2/legacy-devices/eqcm-quartz-crystal->

microbalance-2/

127. Rahide F. Open Challenges on Aluminum Triflate-Based Electrolytes for Aluminum Batteries. Published online 2023. doi:10.1149/1945-7111/acc762
128. McCafferty E. *Introduction to Corrosion Science*. Springer Science & Business Media; 2010.
129. Sauerbrey G. Verwendung von Schwingquarzen zur Wägung dünner Schichten und zur Mikrowägung. *Zeitschrift für Phys.* 1959;155:206-222.
130. Ispas A, Wolff E, Bund A. An Electrochemical Quartz Crystal Microbalance Study on Electrodeposition of Aluminum and Aluminum-Manganese Alloys. *J Electrochem Soc.* 2017;164(8):H5263-H5270. doi:10.1149/2.0381708jes
131. Böttcher R, Ispas A, Bund A. Determination of transport parameters in [EMIm] Cl–based Ionic Liquids–Diffusion and electrical conductivity. *Electrochim Acta.* 2021;366:137370.
132. Tang J, Azumi K. Optimization of pulsed electrodeposition of aluminum from AlCl<sub>3</sub>-1-ethyl-3-methylimidazolium chloride ionic liquid. *Electrochim Acta.* 2011;56(3):1130-1137. doi:10.1016/J.ELECTACTA.2010.10.056
133. Lide DR. *CRC Handbook of Chemistry and Physics*. Vol 85. CRC press; 2004.
134. Di Liberto G, Giordano L. Role of solvation model on the stability of oxygenates on Pt (111): A comparison between microsolvation, extended bilayer, and extended metal/water interface. *Electrochem Sci Adv.* Published online 2023:e2100204.
135. Skúlason E, Tripkovic V, Björketun ME, et al. Modeling the Electrochemical Hydrogen Oxidation and Evolution Reactions on the Basis of Density Functional Theory Calculations. *J Phys Chem C.* 2010;114(42):18182-18197. doi:10.1021/jp1048887
136. Liu L, Liu Y, Liu C. Enhancing the Understanding of Hydrogen Evolution and Oxidation Reactions on Pt(111) through Ab Initio Simulation of Electrode/Electrolyte Kinetics. *J Am Chem Soc.* 2020;142(11):4985-4989. doi:10.1021/jacs.9b13694
137. Lee SS, Schmidt M, Sturchio NC, Nagy KL, Fenter P. Effect of pH on the formation of gibbsite-layer films at the muscovite (001)–water interface. *J Phys Chem C.* 2019;123(11):6560-6571.
138. Likhanova N V, Domínguez-Aguilar MA, Olivares-Xometl O, Nava-Entzana N, Arce E, Dorantes H. The effect of ionic liquids with imidazolium and pyridinium cations on the corrosion inhibition of mild steel in acidic environment. *Corros Sci.* 2010;52(6):2088-2097. doi:https://doi.org/10.1016/j.corsci.2010.02.030
139. Ha JH, Cho JH, Kim JH, Cho BW, Oh SH. 1-Butyl-1-methylpyrrolidinium chloride as an effective corrosion inhibitor for stainless steel current collectors in magnesium chloride complex electrolytes. *J Power Sources.* 2017;355:90-97. doi:https://doi.org/10.1016/j.jpowsour.2017.04.041
140. Wang YC, Lee TC, Lin JY, Chang JK, Tseng CM. Corrosion properties of metals in

- dicyanamide-based ionic liquids. *Corros Sci.* 2014;78:81-88. doi:<https://doi.org/10.1016/j.corsci.2013.09.002>
141. Grosvenor AP, Kobe BA, Biesinger MC, McIntyre NS. Investigation of multiplet splitting of Fe 2p XPS spectra and bonding in iron compounds. *Surf Interface Anal An Int J devoted to Dev Appl Tech Anal surfaces, interfaces thin Film.* 2004;36(12):1564-1574.
  142. Biesinger MC, Payne BP, Grosvenor AP, Lau LWM, Gerson AR, Smart RSC. Resolving surface chemical states in XPS analysis of first row transition metals, oxides and hydroxides: Cr, Mn, Fe, Co and Ni. *Appl Surf Sci.* 2011;257(7):2717-2730.
  143. Bakkar A, Neubert V. A new method for practical electrodeposition of aluminium from ionic liquids. *Electrochem commun.* 2015;51:113-116. doi:10.1016/J.ELECOM.2014.12.012
  144. Kumar S, Verma V, Arora H, Manalastas WJ, Srinivasan M. Rechargeable Al-Metal Aqueous Battery Using NaMnHCF as a Cathode: Investigating the Role of Coated-Al Anode Treatments for Superior Battery Cycling Performance. *ACS Appl Energy Mater.* 2020;3(9):8627-8635. doi:10.1021/acsaem.0c01240
  145. McGuire GE, Schweitzer GK, Carlson TA. Core electron binding energies in some Group IIIA, VB, and VIB compounds. *Inorg Chem.* 1973;12(10):2450-2453. doi:10.1021/ic50128a045
  146. Dong T, Ng KL, Wang Y, Voznyy O, Azimi G. Evaluating Solid Electrolyte Interphase Engineering for Rechargeable Aqueous Aluminum Metal Batteries. In: *Electrochemical Society Meeting Abstracts 239*. The Electrochemical Society, Inc.; 2021:425.
  147. Foelske-Schmitz A, Weingarth D, Kötzt R. Quasi in situ XPS study of electrochemical oxidation and reduction of highly oriented pyrolytic graphite in [1-ethyl-3-methylimidazolium][BF<sub>4</sub>] electrolytes. *Electrochim Acta.* 2011;56(28):10321-10331. doi:<https://doi.org/10.1016/j.electacta.2011.03.064>
  148. Foelske-Schmitz A, Weingarth D, Kaiser H, Kötzt R. Quasi in situ XPS study of anion intercalation into HOPG from the ionic liquid [EMIM][BF<sub>4</sub>]. *Electrochem commun.* 2010;12(10):1453-1456. doi:<https://doi.org/10.1016/j.elecom.2010.08.007>
  149. Rahide F, Flowers JK, Hao J, Stein HS, Ehrenberg H, Dsoke S. Hindered Aluminum Plating and Stripping in Urea/NMA/Al (OTF)<sub>3</sub> as a Cl-Free Electrolyte for Aluminum Batteries. *J Electrochem Soc.* 2023;170(12):120534.
  150. Rahide F, Palanisamy K, Flowers JK, et al. Modification of Al surface via acidic treatment and its impact on plating and stripping. *ChemSusChem.* 2024;17(5):e202301142.
  151. J. C. *Handbook of X-Ray Photoelectron Spectroscopy.*; 1992.
  152. Yan Y, Zhu Y, Zhang L, et al. Study on the anodic behavior of AISI E52100 steel in two fluorine-containing ionic liquids. *Res Chem Intermed.* 2021;47(5):2107-2123. doi:10.1007/s11164-020-04386-3

153. Kumar S, Rama P, Yang G, Lieu WY, Chinnadurai D, Seh ZW. Additive-Driven Interfacial Engineering of Aluminum Metal Anode for Ultralong Cycling Life. *Nano-Micro Lett.* 2022;15(1):21. doi:10.1007/s40820-022-01000-6
154. Liu X, Mariani A, Zarrabeitia M, et al. Effect of organic cations in locally concentrated ionic liquid electrolytes on the electrochemical performance of lithium metal batteries. *Energy Storage Mater.* 2022;44:370-378. doi:https://doi.org/10.1016/j.ensm.2021.10.034
155. La Mantia F, Wessells CD, Deshazer HD, Cui Y. Reliable reference electrodes for lithium-ion batteries. *Electrochem commun.* 2013;31:141-144. doi:https://doi.org/10.1016/j.elecom.2013.03.015
156. Ruch PW, Cericola D, Hahn M, Kötz R, Wokaun A. On the use of activated carbon as a quasi-reference electrode in non-aqueous electrolyte solutions. *J Electroanal Chem.* 2009;636(1):128-131. doi:https://doi.org/10.1016/j.jelechem.2009.09.007
157. Lee SE, Tang MH. Reliable reference electrodes for nonaqueous sodium-ion batteries. *J Electrochem Soc.* 2019;166(14):A3260.
158. Pastel GR, Chen Y, Pollard TP, et al. A sobering examination of the feasibility of aqueous aluminum batteries. *Energy Environ Sci.* Published online 2022.
159. honeywellcom. US patent US8795905B2 4. *Phys Chem Chem Phys.* 2018;21(3):832. www.honeywell.com
160. Fischer K. Accurate Water Determination Aquastar ® Karl Fischer.
161. Sarapulova A, Zemlyanushin E, Sabi N, Hofmann A, Trouillet V. Accepted Manuscript. Published online 2024. doi:10.1002/batt.202400317
162. Equipment, EL-CELL electrochemical test. <https://www.el-cell.com/products/test-cells/optical-test-cells/ecc-opto-10/#1489590351680-30ae9365-4211>

## 10 Contributions of Authorship

Chapter 4 originates from the scientific publication, titled “Exploring the Possibility of Aluminum Plating/Stripping from a Non-Corrosive  $\text{Al}(\text{OTf})_3$ -Based Electrolyte” in the Journal of Batteries & Supercaps.<sup>161</sup>

- **Mahla Talari:** Lead author, conducted all electrochemical experiments, data analysis, cell assembly, and electrolyte preparation. Authored the manuscript with supervision and conceptualization from Sonia Dsoke.
- **Eugen Zemlyanushin:** Executed and analyzed SEM/EDX characterization.
- **Angelina Sarapulova:** Co-conducted EQCM measurements and analysis, and provided supervision.
- **Andreas Hofmann:** Performed GC measurements and data interpretation.
- **Vanessa Trouillet:** supervision on XPS data
- **Noha Sabi:** supervision and conceptualization of the manuscript

Chapter 5, the work was carried out by Mahla Talari under the guidance and conceptualization of Sonia Dsoke and Julia Maibach, with EMImBF<sub>4</sub> and EMImOTf inhibitors supplied by IoLiTec-Ionic Liquids Technologies GmbH.

Chapter 6 reflects Mahla Talari’s insights from her experiences with Rechargeable Aluminum Batteries (RABs).

During the preparation of this work, the author used AI assistants, including Copilot, Gemini, and ChatGPT, to aid in the writing process. After using this tool/service, the author reviewed and edited the content as needed and took full responsibility for the content.

## 11 Scientific contributions

### 11.1 Publication

1. M. Talari, A. Sarapulova, E. Zemlyanushin, N. Sabi, A. Hofmann, V. Trouillet, S. Dsoke, Exploring the possibility of aluminum plating/stripping from a non-corrosive  $\text{Al}(\text{OTf})_3$ -based electrolyte, *Batteries & Supercaps*, **2024**.

### 11.2 Conference contributions

1. M. Talari, J. Du, F. Jeschull, J. Maibach, Sonia Dsoke, mitigating corrosivity of the Chloroaluminate electrolyte for aluminum batteries using additives, *International Conference, Hong Kong (China) – International Meeting on Lithium batteries (IMLB) 2024*, Poster presentation.

2. M. Talari, A. Sarapulova, E. Zemlyanushin, N. Sabi, A. Hofmann, V. Trouillet, S. Dsoke, Exploring the possibility of aluminum plating/stripping from a non-corrosive  $\text{Al}(\text{OTf})_3$ -based electrolyte, *International conference, Gothenburg (Sweden) - The Electrochemical Society (ECS)*, **2023**, Oral presentation.

3. M. Talari, S. Dsoke, Chloroaluminate Ionic Liquids in Aluminum Batteries corrosivity issue, *POLiS Conclave meeting, Ulm (Germany)*, **2023**. The presentation included a poster and a winning science slam talk.